Master Thesis

Iondynamics in helium nanoclusters after Interatomic Coulombic Decay

Submitted by
Amnueporn Florian Carl Lebrecht Wiegandt
September 2015

Supervisor: Prof. Dr. Reinhard Dörner
PD Dr. Till Jahnke

Goethe-Universität Frankfurt am Main
Institut für Kernphysik

Contents

Chapter 1

Introduction

In attempting to understand the properties of matter and answer the question “where everything took its origin”, modern physics has explored regions of extraordinary high energy densities. Nuclear physics has created exotic particles, has formed new and heavy elements and has broken the strongest nuclear bonds. On the other side atomic and solid state physics have reached regions of ultra-low energy density and have achieved the ability to study nature’s most weakly bound systems such as rare gas molecules and clusters. In the family of rare gas molecules helium dimers and helium clusters are the most weakly bound systems and as such the most weakly bound structures in nature. At the same time the helium dimer is the largest diatomic molecule that can form with internuclear distances reaching the regime of macroscopic structures as a DNA-helix and small viruses (Figure 1.1). Despite its nearly macroscopic size, this molecule is one of the simplest quantum systems and is subject to many quantum effects that have been observed in the past. Quantum behavior can also be seen even if the number of helium atoms that form a bound system increases. Such compounds of cold helium atoms, so-called helium clusters, reach sizes up to 10^7 and more atoms. Thus, these clusters represent a link between simple quantum systems and macroscopic structures. In the context of nanotechnology it is highly relevant how a change in size affects the properties of an assembly.

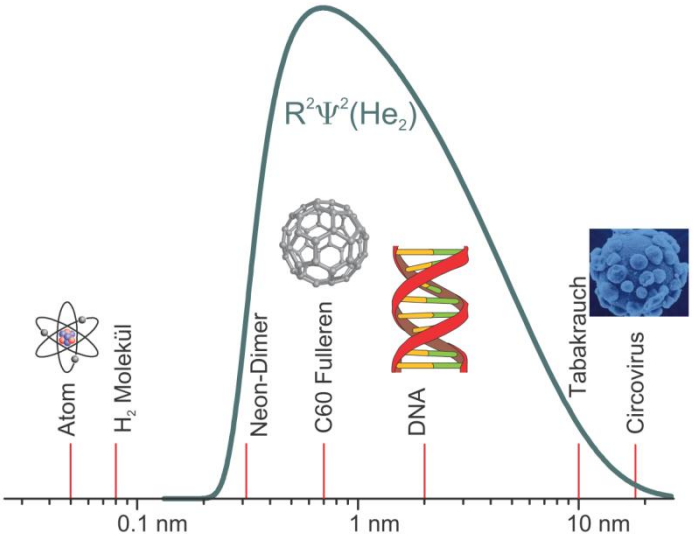

Figure 1.1: Distribution of internuclear distances for the helium dimer on a logarithmic scale. The size is comparable with the size of macroscopic molecules and viruses. Illustration is taken from **[1]**.

Due to their superfluid and inert characteristics, helium nanoclusters are often used in spectroscopy as a cooling matrix for dopant atoms and exotic molecules in order to study their properties at extraordinarily low temperatures down to 0.4 Kelvin. Therefore, a better understanding of the interaction of charged particles such as ions and electrons with the helium clusters is obviously of great interest.

1.1 Motivation

In order to better understand the properties of these clusters, their ionization and fragmentation dynamics have been studied by using electron impact ionization [2] and photoionization [3]. **I**nteratomic **C**oulombic **D**ecay (ICD) has been introduced as a very efficient way to deposit two neighboring charges into helium clusters which create a well-defined initial state to study the subsequent fragmentation of the compound caused by Coulomb explosion[1] of the ion pair.

It is of great interest to verify the feasibility of inducing ICD in such clusters by using synchrotron radiation and to investigate the interaction of the ionic fragments that have taken part in the decay as well as the interaction of the emitted electrons with the helium

[1] Strong repulsion driven by the Coulomb forces between two ions

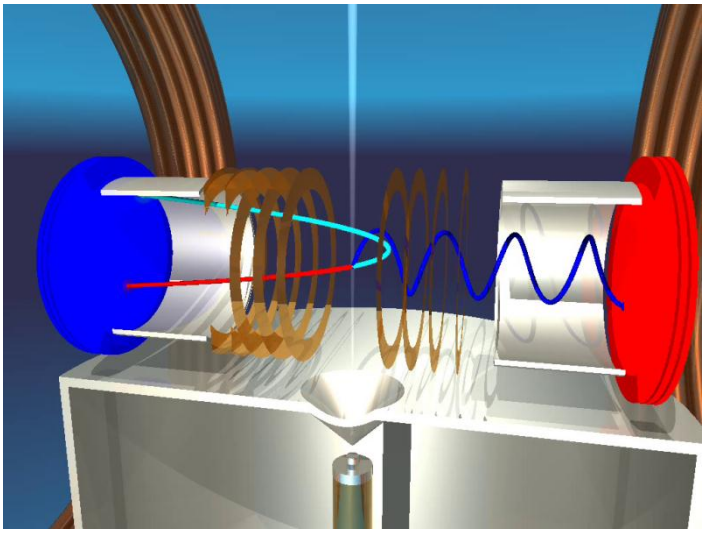

Figure 1.2: The COLTRIMS-reaction microscope consists of three main components. A thin jet of cold gas is crossed with the projectile pathway defining a target zone in the middle of the setup. All emerged ions are then guided onto two opposite detectors (shown in red and blue) by an electric and magnetic field. Illustration is taken from **[4]**.

droplet. The **COL**d **T**arget **R**ecoil **I**on **M**omentum **S**pectroscopy (COLTRIMS) reaction microscope (Figure 1.2) provides an excellent tool to get an entire view on the kinematics of those particles. Nevertheless previous experiments could not unambiguously reveal these dynamics and prove the existence of ICD in large helium clusters [5].

1.2 Background

Predicted in 1997 by Cederbaum *et al.* [6] and experimentally verified in 2004 by Jahnke *et al.* [7], ICD represents a mechanism to transfer excitation energy by exchange of a virtual photon from one atom to a neighboring atom causing ionization. It has been used to investigate the ionization dynamics of rare gas dimers and clusters. The fragmentation of helium dimers after an interatomic Coulombic decay has first been characterized by T. Havermeier in 2010 [8]. By using synchrotron radiation and COLTRIMS he was able to identify ICD as a significantly contributing decay-channel of the singly ionized and excited helium dimer. In 2013 the ionization dynamics of large helium clusters have been studied by C. Müller by using the same method [5]. He was able to detect electrons in coincidence with small ionic fragments with characteristic

energy relation which he interpreted to be the fragments of small helium clusters that have undergone ICD. This typical energy relation could not be found for larger ionic fragments which themselves had a significantly lower energy than expected. The secession of neutral helium atoms from initially larger ionic fragments has been suspected to dissipate energy and lead to this deviation. Nevertheless it could not be elucidated at which point neutral atoms emerge from the ionic fragments. The size of the target-clusters also remained uncertain due to a lack of accurate temperature and pressure data of the target source as well as the correlation between the different fragment sizes and the size of the clusters they originated from.

Therefore, a new experiment on ICD induced helium cluster fragmentations under well controlled source conditions is presented in the present work. We have characterized the fragmentation of pure ^{4}He nanoclusters of mean sizes between N~5000 and N~200000.

ICD was induced in the clusters by using a VUV photon beam of $h\nu = 67$ eV from the BESSY II synchrotron light source causing photoionization and excitation.

Cluster breakups into singly charged $\mathbf{He}_N^+$ fragments containing one to twenty helium atoms have been observed. Energy spectra are presented for the kinetic energy release (KER) and the energy of the emitted electrons in different fragmentation channels. Elastic scattering of the charged fragments from neutral cluster atoms as well as evaporative cooling are discussed in the present work as two energy dissipative mechanisms that can explain the results from [5].

Chapter 2

Fundamentals

This chapter gives a brief resume of the physical principles underlying the formation of helium dimers and helium clusters. In addition, the laboratory conditions that are necessary for the formation of those clusters as well as the properties of helium clusters will be described. In the following several interaction mechanisms of synchrotron radiation with such helium clusters and correlated processes that are relevant for this work will be discussed and finally the process of Interatomic Coulombic Decay in helium dimers and clusters will be introduced.

2.1 Interatomic bonds

At room temperatures and atmospheric pressures the potential energy of most atoms can be reduced by the formation of interatomic bonds and the creation of diatomic molecules and larger compounds. Bond types are often categorized in metallic, ionic, covalent, dipole, hydrogen, and Van der Waals-bonds according to the predominant mechanisms that lead to their formation.

Metal bonds are found in the solid phase of metals. The valence electrons in metal atoms show a very low binding energy which gives them the capability to jump from atom to atom inside a crystal lattice. The high electron mobility leads to the creation of an electron gas and conduction bands that give them a very good electrical and thermal conductivity. The characteristic bond strength of such metal atoms inside a crystal lattice is usually smaller than 1 eV.

In **ionic bonds** atoms try to reach the rare gas configuration by tearing one or more electrons away from their less electronegative binding partners aiming to fill up their orbitals. In this way pairs of cations and anions are formed which bind together by the attractive Coulomb force. This type of bond can typically be found between metal atoms and nonmetal atoms. An example for an ionic bound molecule is the $Na^{+}Cl^{-}$ molecule (salt). The bond strengths of such ionic bonds are high compared to metallic bonds and reach values of several eV. Ionic bonds can also be partly covalent.[1]

In contrast to ionically bound molecules the electrons in **covalent** or **atomic bonds** are shared between both binding partners. The differences between metal-bonds and covalent bonds are small and mainly based on the degree of delocalization of the involved electrons. In the bound state atoms that undergo covalent bonds are in an equilibrium state between repulsive Coulomb interaction of the two positively charged nuclei and the attractive exchange interaction of the electrons. This can be illustrated by using the example of the covalent bound diatomic H_2^+ molecular ion. The atomic 1s-orbitals create an overlap and form molecular σ-orbitals as solutions of the Schrödinger-equation. In this sense, two orbitals can be obtained of which only one leads to a bound state (Figure 2.1). In case of a symmetric overlap the resulting electron density distributions add up in such a way that the probability to find the electrons between the two atoms is increased causing a shielding effect of the electrostatic repulsion between the two nuclei. If the overlap is asymmetric, the atomic wave functions[2] interfere destructively resulting in an extenuation of the electron density between the two atoms.

[1] The ionic character of a bond depends on the difference in electronegativity of the binding partners.
[2] A solution of the Schrödinger equation in position space is called “wave function”

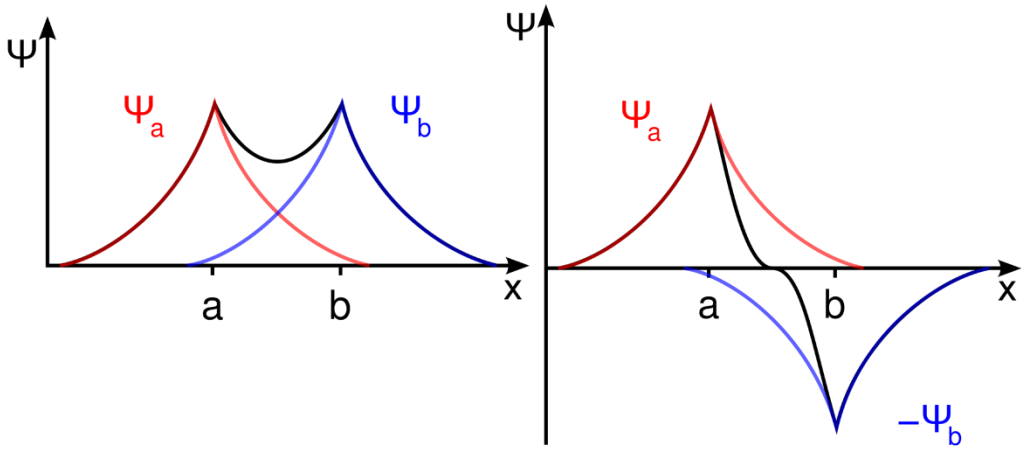

Figure 2.1: The two solutions of the Schrödinger equation for the hydrogen molecular ion with single atoms centered in **a** and **b** lead to a so-called bound and an anti-bound state. In the bound state the atomic wave functions create a symmetric overlap (left), which lead to a higher electron density between the atoms. Illustration is taken from **[9]**

Covalent bonds are predominant between atoms of nonmetallic elements except the rare gases. These atoms have orbitals which are saturated with electrons. In this case the Pauli-principle has to be taken into account which constrains the binding electrons to occupy both binding and anti-binding states. This results in a domination of the repulsive effects of the anti-binding state. For helium this can be illustrated in a term diagram (Figure 2.2).

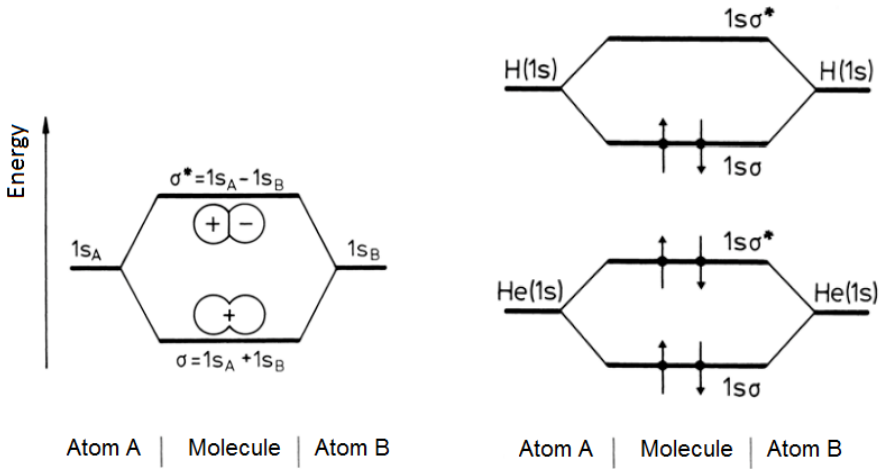

Figure 2.2: Term diagram of the combination of two 1s orbitals to a molecular σ-orbital (left). The symmetric or asymmetric overlap lead to two energetic states. Due to the Pauli principle the four electrons of a helium molecule would have to occupy both states. Thus a covalent bond between two helium atoms does not exist (right). Illustration is adapted from **[5]**.

In contrast to all other bonds, **Van der Waals bonds** are found between all types of atoms or molecules even atoms of the rare gases. Similar to the dipole bond, this bond type relies on electrostatic forces between two electric dipoles. If molecules contain atoms of different electronegativity, they can induce a static electric dipole momentum in the particles. Two molecules then align to each other and form larger structures. Moreover, electric dipole moments can emerge even from molecules and atoms with totally isotropic charge distribution and electronegativity. Due to fluctuations in the electron cloud around the particles, temporary electric dipoles are created which then polarize neighboring atoms. The polarizations of both atoms stabilize each other and create a static attractive potential $V(R)$ between the two atoms. At large internuclear distances the attractive Van der Waals forces are predominant.

$$V(R) \lim_{R\to\infty} = -\frac{C_w}{R^6} \tag{2.1}$$

The positive Van der Waals coefficient C_w can be determined by using second order perturbation theory. At short distances though, the repulsive potential of the nuclei comes into play. The resulting potential can be approximated with a Lennard-Jones potential ("6-12 potential") by applying the empirical parameters $m = 6$ and $n = 12$:

$$V(R) = \frac{m}{n-m}\epsilon\left[\left(\frac{R_0}{R}\right)^n - \frac{n}{m}\left(\frac{R_0}{R}\right)^m\right] \tag{2.2}$$

where ϵ, R_0determine the position and the depth of the potential minimum (Table 2.1).

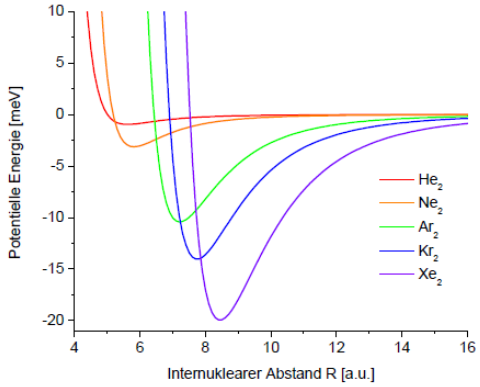

Figure 2.3: Lennard-Jones potentials for some rare gas dimers. (Taken from **[8]**).

	ϵ [eV]	R_0[a.u.]
He_2	9.467E-4	5.6165
He_2^+	2.476	2.042
Ne_2	3.121E-3	5.8128
Ar_2	1.041E-2	7.2129
Kr_2	1.404E-2	7.7433
Xe_2	1.997E-2	8.4434

Table 2.1: Parameters for some rare gases **[8]**.

The Van der Waals bond is extremely weak compared to all other bond types. Typical binding energies are of the order of 0.1 eV. Thus, the strength and the stability of the interaction changes dramatically if one of the binding partners is ionic. The potential $V(R)$ then drops by R^4 and is proportional to the polarizability c_D of a static dipole:

$$V(R) \lim_{R\to\infty} = -\frac{c_D}{R^4} \tag{2.3}$$

For short distances the approximation made in (2.2) can be modified with $m = 4$. However, this approximation reaches its limits for extremely flat potential wells such as the Lennard-Jones potential for the helium dimer (Figure 2.3). To calculate the exotic properties of the helium molecule, complex diffusion quantum Monte Carlo methods are required [8] which use the Green's function to solve the Schrödinger equation.

2.2 The helium dimer

Because of the very shallow binding potential of the helium dimer its existence has long been doubted. Calculations made by K. Tang in 1995 estimated a potential depth of only -0.94668 meV [10]. Taking into account the zero point energy of the ground state which has a value of -0.94658 meV, the energetic states of this system lay only 95 neV below the continuum. This extremely low binding energy has a strong impact on the size of this molecule. The momentum and the localization of particles are connected by the Heisenberg uncertainty principle.

$$\Delta p \cdot \Delta x \geq \frac{\hbar}{2} \tag{2.4}$$

This determines that the location and the momentum of a particle cannot be observed at the same time with infinite accuracy. In a one-dimensional potential this relation can be written as:

$$\Delta E \cdot \Delta x \geq \frac{\hbar}{2m} |\langle p_x \rangle| \tag{2.5}$$

By applying relation (2.5) on the binding energy and momentum of the helium dimer, Δx has to be in the order of 50 Å. This value matches very well to the average internuclear distance that has been measured for instance in [11]. The distribution of internuclear distances is very broad (Figure 1.1). While the maximum has been found at distances of about 7 Å, also sizes of more than 200 Å can be found [1]. The extremely low binding energy of this potential leads to the fact that neither bound vibrational nor rotational exited energy states exist in this molecule. Furthermore, helium dimers can only be created from the ^{4}He isotope because the zero point energy in hypothetical ^{3}He-^{3}He or ^{3}He-^{4}He systems already exceeds the potential depth [12].

At room temperature the average energy of atoms is about $E = k_B T = 26\, meV$. This value is almost five orders of magnitude higher than the binding energy of the ground state of the ^{4}He dimer. To create helium dimers or even larger helium clusters, extreme temperature conditions are thus indispensable.

2.2.1 Helium clusters

Already in the 1960s helium clusters have been formed in cold molecular beams. Since the 1980s, a series of interesting properties have been revealed which can be ascribed to the low binding energy and small mass of the helium atoms. Due to their low temperatures, helium clusters always exist in a liquid state, which is why they are often known as helium droplets. Above a critical number[1] of atoms such droplets become superfluid when a macroscopic number of helium atoms occupy the same quantum

[1] Characteristic dimensions should be greater than the temperature dependent coherence

state. The binding energy of each He atom in a droplet is about 0.6 meV [13]. The shape of such droplets is spherical or ellipsoid with a center density of $\rho = 21.8\ nm^{-3}$ dropping towards zero at the surface within a distance of 6 Å [14] [15] [16]. The exact structure of helium droplets is still subject to ongoing research. X-ray diffraction experiments have recently indicated the existence of quantum vortices in superfluid droplets [17]. As a superfluid these clusters provide an infinite thermal conductivity. When heated, thermal energy can be dissipated by evaporation of neutral helium atoms from the cluster surface until the equilibrium temperature of 0.38 K is reached again [18]. In addition, movement inside the superfluid clusters can happen frictionless underneath a certain velocity, called the Landau velocity (60 m/s). Helium droplets are transparent for light in a very broad band reaching from far infrared to vacuum ultraviolet (VUV).

The ultra-cold temperatures essential for the formation of helium clusters can be attained by an adiabatic gas expansion. Typically precooled helium at temperatures of $T_0 < 20\ K$ and pressures of $P_0 \approx 10$ bar is expanded through a nozzle of $d \approx 5\ \mu m$ into a vacuum chamber. When streaming through the nozzle, the helium gas expands adiabatically creating a supersonic shock wave. The random motion of the gas atoms is then guided into a directed stream of helium atoms while internal collisions contract the thermal velocity distribution causing the gas to cool down towards temperatures below 1 mK. Starting from a certain point $T_0,\ P_0$ in the gas phase, the expansion follows an isentrope in the phase diagram of helium. Above a starting temperature of about $T_0 = 10\ K$ the isentrope passes the critical point $T_C = 5.2\ K$ from the gas side.

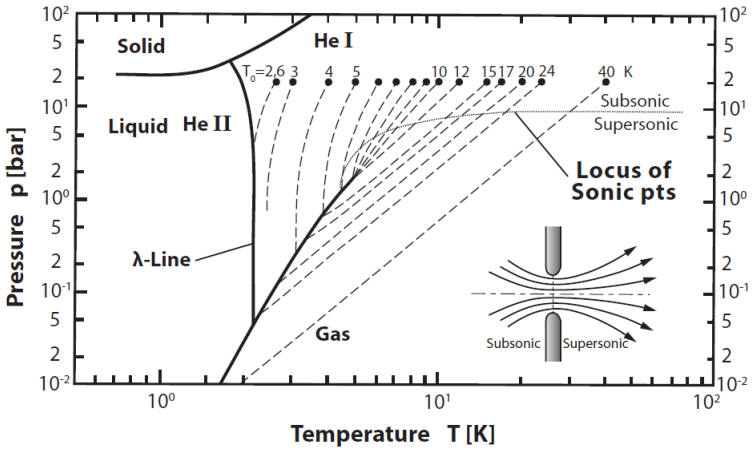

Figure 2.4: Phase diagram of ^{4}He. Starting from a certain point in the diagram the expansion follows an isentrope (dotted lines). (From **[19]**).

While crossing the phase separation line to the He-I liquid phase, supercooled helium vapor starts to condensate into clusters (Figure 2.4).

If the starting temperature is lower ($T_0 < 10\,K$), the helium is already liquid before passing the nozzle. The expansion in this case follows its isentrope until it reaches the phase separation line from the He-I side. At temperatures lower than 5 K a narrow stream of liquid helium leaves the nozzle and fragments into very large droplets due to Rayleigh instabilities [20].

In both cases subsequent evaporation leads to a further cooling of the droplets until their temperature falls below the lambda point $T_\lambda \approx 2.18\,K$ and the droplets become superfluid when entering the He-II phase. The temperature drops further down until the equilibrium temperature of $T_E = 0.38\,K$ is reached.

The size distribution of clusters generated in free jet expansions is extremely broad and depends strongly on temperature and pressure of the precooled helium. Small changes in the starting temperature T_0 of only a few Kelvin can alter the mean cluster size in several orders of magnitude. Lower starting temperatures and higher pressures P_0 lead to larger clusters. However, the exact cluster size distribution is difficult to determine. Numerous experiments including deflection [21] and electron impact ionization experiments [22] [23] have found a logarithmic-normal distribution for the expansion of subcritical and supercritical helium [24] [25]:

$$P_N^{sub} = \frac{1}{N\delta\sqrt{2\pi}} e^{\frac{-(\ln(N)-\ln(\widehat{N}))^2}{2\delta^2}} \quad and \quad P_N^{sup} = \frac{1}{\langle N\rangle} e^{-\frac{N}{\langle N\rangle}} \tag{2.6}$$

where P_N is the probability to find clusters of a size N if $\widehat{N}$ is the most probable cluster size. The parameter $\delta = 0.626$ reflects the width of the distribution [23]. Despite the broadness of the log-normal distribution, the mean cluster size $\langle N\rangle$ (or simply "N" as used in the subsequent chapters) is from a practical standpoint a reasonable parameter to characterize the gas targets used in this experiment.

$$\langle N\rangle = e^{\ln(\widehat{N})+\frac{\delta^2}{2}} \quad and \quad \widehat{N} = \langle N\rangle\, e^{-\frac{\delta^2}{2}} \tag{2.7}$$

The mean cluster sizes found in free helium jet expansions in dependence of the starting conditions T_0, P_0 have been experimentally determined in 2004 by Toennies *et al.* [19] (Figure 2.5) and recently in 2011 by Gomez *et al.* [20] (Figure 2.6).

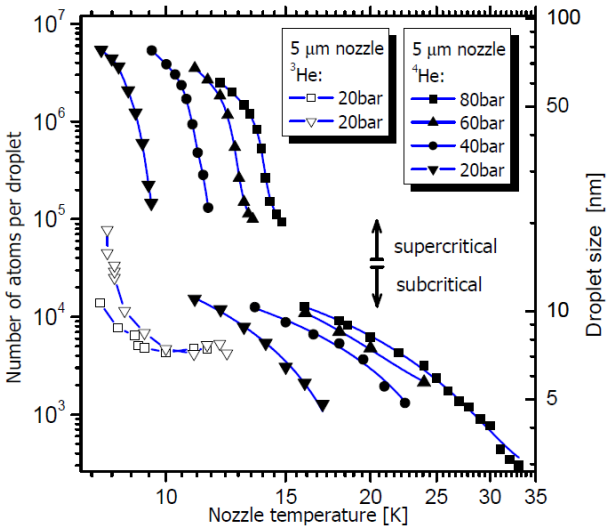

Figure 2.5: Mean droplet sizes ⟨**N**⟩ as a function of $\mathbf{T_0}$, $\mathbf{P_0}$ as observed in **[19]**.

However, the experiment reported in [20] provides the most accurate correlation of mean cluster sizes and temperatures T_0 by holding the stagnation pressure P_0 constant.

Attempts were made in [26] to empirically estimate the maximum size reached in free jet expansions through a nozzle with a diameter d [µm] starting from T_0 $[K]$, P_0 [bar]:

$$\widehat{N} \approx 6264 \cdot \frac{P_0 d^{1.5}}{T_0^{2.4}} \tag{2.8}$$

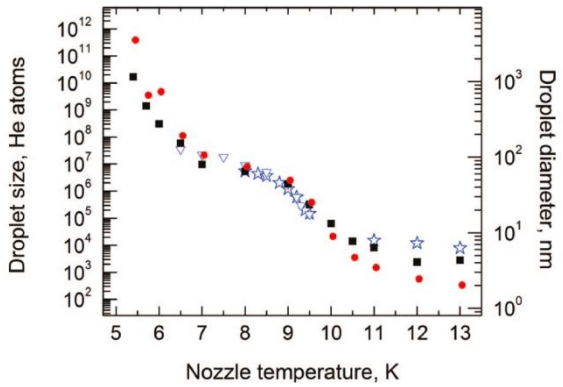

Figure 2.6: The mean droplet sizes ⟨**N**⟩ in dependence of $\mathbf{T_0}$ as measured in **[20]**. A nozzle of 5 µm diameter was used and the stagnation pressure was set to $\mathbf{P_0 = 20\ bar}$.

2.3 Photoexcitation and -ionization

Atoms and molecules can absorb energy from their environment and can be excited. There are three forms of excitation, namely rotational excitation, vibrational excitation and electronic excitation. By taking quantization into account, atoms and molecules can occupy only discrete states of excitation which are well determined by their associated wave functions and energy eigenvalues. During a photoexcitation or ionization an atom or molecule absorbs energy from a photon and changes its energetic state. The electronic excitation is the most relevant excitation process for this work. Atoms can be excited if bound electrons absorb energy and populate a state of higher energy. The energy required to reach the various energy levels is gained from the photon energy. If this energy is sufficiently high, an electron can be lifted up from its orbital into the continuum and the free electron leaves the ionized atom. In this case the photon energy must exceed the ionization threshold energy of the electron orbital. The electron carries away as much energy as remains after subtracting its binding energy from the photon energy.

$$E_{kin} = E_{\gamma} - E_B \tag{2.9}$$

The quantum mechanical description of photoionization and excitation is based on the time-dependent Schrödinger equation for the interaction between electromagnetic radiation and atoms.

$$i\hbar \frac{\partial}{\partial t}\psi(r,t) = H(t)\psi(r,t) \tag{2.10}$$

In a single-electron-system the time dependent Hamiltonian $H(t)$ can be separated in:

$$H(t) = -\frac{\hbar^2}{2m}\nabla^2 - \frac{Ze^2}{4\pi r\varepsilon_0} - \frac{i\hbar e}{m}\mathbf{A} + \frac{e^2}{2m}\mathbf{A^2} \tag{2.11}$$

a time independent part H_0:

$$H_0 = -\frac{\hbar^2}{2m}\nabla^2 - \frac{Ze^2}{4\pi r\varepsilon_0} \tag{2.12}$$

and a time dependent interaction part $H_{int}(t)$ containing the vector potential[1] $\mathbf{A}$:

$$H_{int}(t) = -\frac{i\hbar e}{m}\mathbf{A} + \frac{e^2}{2m}\mathbf{A^2} \tag{2.13}$$

Assuming a single-photon-process, the $\mathbf{A^2}$-term in equation (2.13) can be neglected because no further interaction with the light field has to be taken into account [5].
Furthermore, the transition cross section $\sigma_{A\to B}$ between two states can be written as:

$$\sigma_{A\to B} = \frac{4\pi^2\alpha\hbar^2}{m^2(E_B - E_A)}\,|M_{AB}|^2 \tag{2.14}$$

where M_{AB} is the transition dipole moment for the transition from state A to B.

2.3.1 Photoionization

For the transition between an initial state and the continuum state in case of a photoionization the transition moment can be expressed as:

$$M_{AB} = \langle\psi_A|\epsilon e^{i\mathbf{k}\cdot\mathbf{r}}\nabla|\psi_B\rangle = \int \psi_A(\mathbf{r})\,\epsilon e^{i\mathbf{k}\cdot\mathbf{r}}\nabla\psi_B(\mathbf{r})d\mathbf{r} \tag{2.15}$$

Usually the photon wavelength is several orders of magnitude larger than the size of one atom. In this case the term $\mathbf{k}\cdot\mathbf{r}$ which goes along with the wavenumber $\mathbf{k} = \frac{2\pi}{\lambda}$ in equation (2.15) is very small and the exponential part can be set to one.

[1] The radiation field is represented by the vector potential in the Coulomb gauge

Thus, the transition moment M_{AB} for the photoionization can be derived by using the so-called dipole approximation[1].

$$M_{AB} = \langle \psi_A | \epsilon \nabla | \psi_B \rangle \tag{2.16}$$

By using Fermi's golden rule, this leads to the differential cross section for the photoionization process.

$$\frac{d\sigma}{d\Omega}(\Theta) = 4\pi^2 \alpha \omega k |\epsilon D_{AB}|^2 = \frac{\sigma_{tot}}{4\pi}[1 + \beta P_2 \cos(\Theta)] \tag{2.17}$$

In which P_2 designates the second Legendre-polynomial and β is the asymmetry-parameter which can take values between -1 and 2. With the asymmetry-parameter tribute is paid to the fact that the system has a certain angular momentum.

The photoionization cross-section depends on the photon energy and reaches its maximum at the ionization threshold while it drops for higher energies (Figure 2.8).

The energy eigenvalues of different energy levels in the helium atom are well-known [27] and can be approximated by:

$$E_{nl,\pm} \approx -\frac{Z^2}{2}\left(1 + \frac{1}{n^2}\right) + J_{nl} \pm K_{nl} \tag{2.18}$$

where J_{nl} is the Coulomb integral and K_{nl} is the exchange-integral. The resulting energy levels are listed in Table 2.2.

[1] Neglecting higher terms in the series expansion of the exponential function.

2.3.2 Two-step-one process

In addition to photo single ionization, two processes can lead to photo double ionization, namely the electron shake-off and the two-step-one process.

The latter process can take place in a helium atom if the atom is ionized (for example by photoionization) and the emitted photoelectron collides with a second electron from the same atom while having enough energy to set it free.

$$\mathbf{He} + h\nu \rightarrow \mathbf{He}^{2+} + 2e^{-} \tag{2.19}$$

As mentioned before, the energy of the photoelectron must be high enough for the second ionization. Though, the Møller scattering cross section for an electron-electron scattering drops with higher electron energies [28]. This fact narrows the energy window for this process. At higher energies the shake-off process outweighs the two-step-one process.

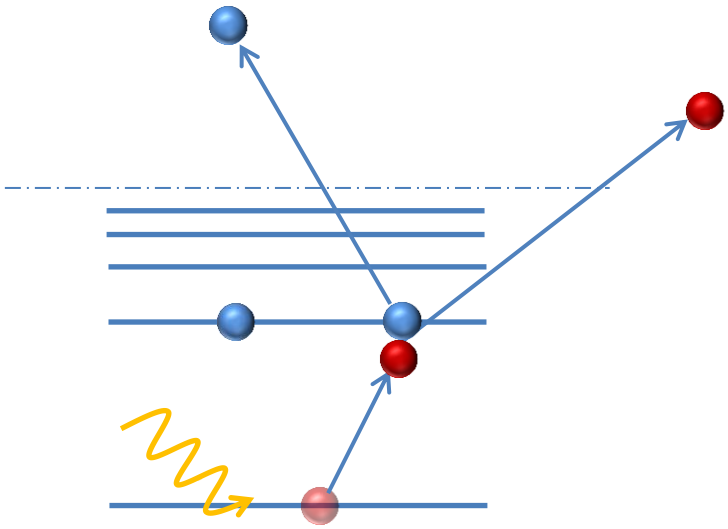

Figure 2.7: Single photon double ionization: Diagram of the photo-induced two-step-one process. The primary photoelectron hits the secondary electron on its way out of the atom. As a result two free electrons leave the atom.

2.3.3 Shake-off Process

At higher energies the probability to create doubly charged helium ions by electron shake-off is higher than by the two-step-one process [5]. Once the photoelectron has left the system after a very fast photoionization, the remaining electron is exposed to an abrupt change in the potential. Although the change of the system's Hamiltonian is sudden, the wave function must remain continuous. The wave function of the initial state can be expanded into the eigenstates of the modified, final-state potential. The probability to find electrons which originated from an initial state in a final state is given by:

$$P_{i\to f} = \int \left|\psi_f^* \psi_i d\tau\right|^2 \tag{2.20}$$

ψ_i and ψ_f are the wave functions defining the initial and final states [29].

The change of the Hamiltonian in the course of the fast photoionization must take place on a short timescale. The time t in which the wave functions and energetic states ϵ_i, ϵ_f merge into each other has to fulfill the so-called "sudden approximation" [29]:

$$\frac{1}{\hbar}(\epsilon_i - \epsilon_f)t \ll 1 \tag{2.21}$$

If the change is sufficiently fast, the wave function of the remaining electron after photoionization can have a finite overlap with the continuum wave function [5].

As a result, the energetic states change in a way that the electron finds itself in the continuum and can leaves the atom.

2.3.4 Photoexcitation

If the supplied energy is not high enough for the ionization, the energy can still be sufficient to lift electrons to levels of higher energy. This process is called photoexcitation. Excited states decay within a certain decay time releasing the stored energy through different decay mechanisms[1].

State	ϵ (singlet)	ϵ (triplet)
$1s^2$	0 eV	-
1s2s	20.616 eV	19.820 eV
1s2p	21.218 eV	20.964 eV
1s3s	22.920 eV	22.718 eV
1s3p	23.087 eV	23.007 eV
1s3d	23.074 eV	23.074 eV
⋮	⋮	⋮

Table 2.2: Energy levels of helium **[8]**.

Besides this single excitation (2.22) also a double excitation (2.23)[2] or even an excitation with additional ionization (2.24) of helium as a two-electron-system is conceivable.

$$\mathbf{He} + h\nu \rightarrow \mathbf{He}^{*} \tag{2.22}$$

$$\mathbf{He} + h\nu \rightarrow \mathbf{He}^{**} \tag{2.23}$$

$$\mathbf{He} + h\nu \rightarrow \mathbf{He}^{+*} + e^{-} \tag{2.24}$$

In case of ionization, the energy levels in the helium ion change as listed in Table 2.3. The energy eigenvalues of this single-electron, hydrogen-like system are much easier to calculate and can be written as [30]:

$$E(n) = E_0 Z^2 \left(1 - \frac{1}{n^2}\right) \approx 13.6\ eV \cdot 2^2 \cdot \left(1 - \frac{1}{n^2}\right)\ [eV] \tag{2.25}$$

[1] Typical decay channels can be radiative decay, Auger decay or interatomic Coulombic decay.
[2] Doubly excited states decay mostly by autoionization: $\mathbf{He} + h\nu \rightarrow \mathbf{He}^{**} \rightarrow \mathbf{He}^{+} + e^{-}$

The photoionization in combination with an additional excitation described in (2.24) is the most relevant process for this work. The energetic threshold for this process is at 65.4 eV. Above this energy a single photon can lift one 1s-electron of the helium atom into the continuum while shifting the remaining into an excited state of the He^+ ion.

$$E = E_{ion}(\mathbf{He}) + E_{\mathbf{He^+}}(n = 2) = 24.59\ eV + 40.81\ eV = \mathbf{65.4\ eV} \quad (2.26)$$

State	J	Level [eV]
1s	1/2	0
2p	1/2	40.813029
	3/2	40.8137552
2s	1/2	40.8130871
3p	1/2	48.3712952
	3/2	48.3715104
3s	1/2	48.3713125
3d	3/2	48.37151
	5/2	48.3715817
⋮	⋮	⋮

Table 2.3: Energy levels of He^+ **[8]**.

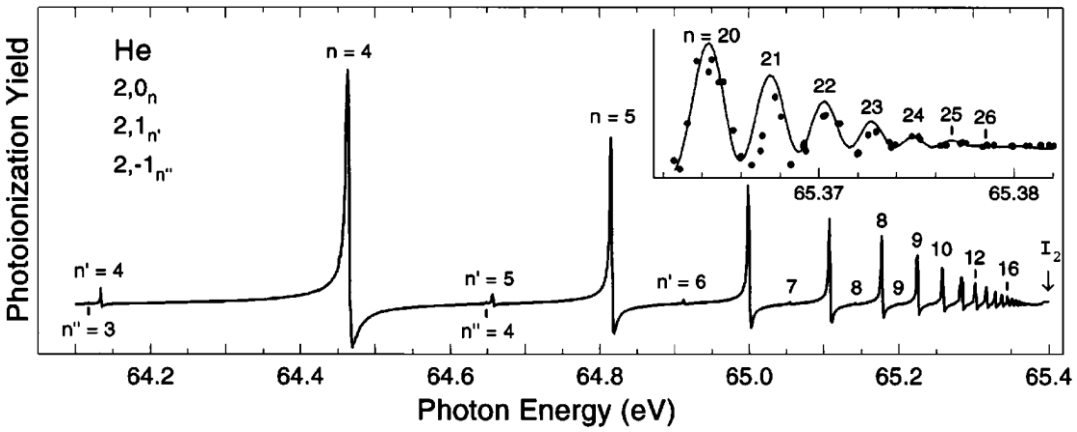

Figure 2.8: Photoionization cross section for the neutral helium atom in dependence of the photon energy as illustrated in **[31]**.

2.4.1 Radiative decay

The lifetimes of such excited states differ strongly and are in the order of a few femtoseconds to several nanoseconds. In many cases this excited state can decay to a lower energetic state or the ground state after lifetimes of picoseconds to nanoseconds by emission of one photon. This deexcitation process is called radiative decay. The emitted photon carries an angular momentum of 1ħ which has to be provided by the system. In this sense only such transitions are allowed that change the parity ($\Delta l = \pm 1$ e.g. $2p \rightarrow 2s$).

Nevertheless, also "forbidden" transitions such as multipole-transitions can possibly take place which don't change the parity. However, multipole-transitions have a much longer lifetime (Table 2.4) than "allowed transitions" and therefore have a negligible contribution to the deexcitation in cases when other transition mechanisms are possible for the system.

State	**Lifetime [ns]**
2p	0.1
2s	1922
3s	1.00
3p	0.34
3d	0.98
⋮	⋮

Table 2.4: Lifetimes of He^{+*} **[8]**.

2.4.2 Interatomic Coulombic Decay

Interatomic Coulombic Decay (**ICD**) is a relaxation mechanism that has been predicted in weakly bound molecules by Cederbaum *et al.* [6] and has recently been verified in helium dimers [8] and small rare gas clusters [5], [7], [32], [33]. ICD can take place in excited compounds of loosely bound atoms as one of them transfers the excess energy to a neighboring atom by a virtual photon causing ionization of its partner. This presupposes that the released excitation energy from the first atom is high enough to ionize its bound partner. In helium dimers or clusters (as well as in other homonuclear rare gas compounds) this can be the case if one helium atom exists in a singly ionized and excited state (equation (2.24)). This helium ion has a vacancy in its 1s-shell while the remaining electron populates a state of higher energy. When returning to the ground state, the stored energy can be transferred to a neighboring atom by a virtual photon. The neighboring helium atom though is ionized and emits one electron which is conventionally called the ICD electron.

$$h\nu + \mathbf{He}_2 \rightarrow \mathbf{He}_2^{+*} + e_{photo}^- \tag{2.27}$$

$$\mathbf{He}_2^{+*} \rightarrow \mathbf{He}^+(1s) + \mathbf{He}^+(1s) + e_{ICD}^- \tag{2.28}$$

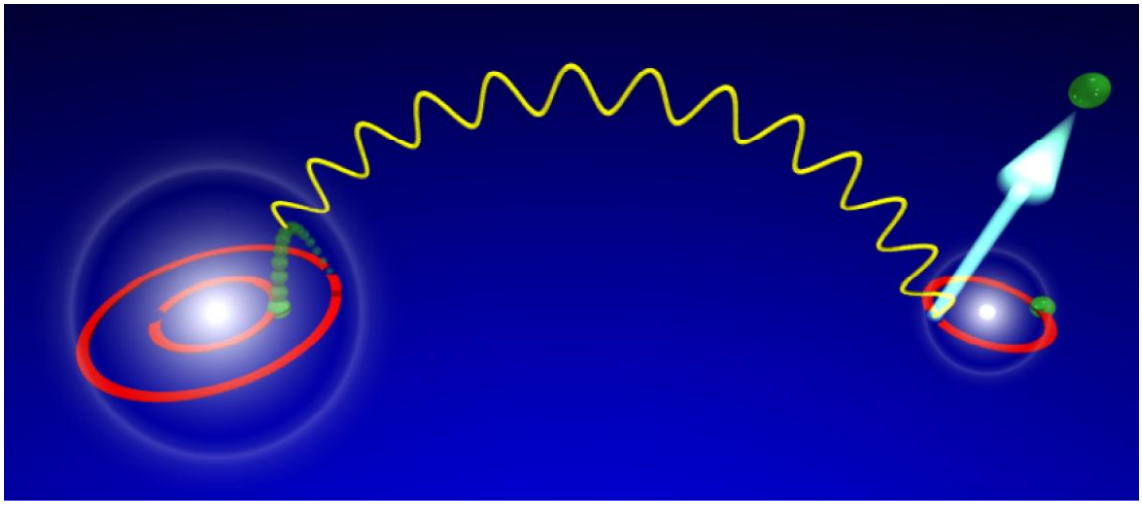

Figure 2.9: ICD in a helium dimer: After ionization and excitation of the left atom the relaxation energy of the decay is transferred by a virtual photon causing the ionization of the partner atom. The emitted electron is called the ICD electron. (From **[8]**).

2.5.1 Ionization dynamics and kinetic energy release

An ionized and excited helium dimer $\mathbf{He_2^{+*}}(n = 2)$ occurring after photoionization and excitation of one helium atom (equation (2.24) and (2.26)) is significantly stronger bound than the neutral $\mathbf{He_2}$. The potential curves for an $n = 2$ excited ion illustrated in Figure 2.9 show a minimum of about 200 meV at a distance of 3.5 atomic units. This leads to a sudden contraction of the dimer and the excitation of vibrational states in the $\mathbf{He_2^+}$ before a deexcitation can take place. In this context two decay channels are conceivable which have lifetime dependent probabilities. The lifetime for a radiative decay is in the order of several nanoseconds whereas the lifetime of the ICD process depends on the internuclear distance and stays, in case of He_2, in the order of picoseconds [34]. This gives radiative decay a higher probability at distances larger than 20 Å whereas the ICD process is predominant at internuclear distances below 10 Å [35]. The ICD channel leads to the ionization of the neighboring atom and the ion pair dissociates along the repulsive Coulomb potential of the dimer. The repulsion due to the strong electrostatic force causes an immense acceleration of the two particles and the transformation of potential into kinetic energy in the so-called "Coulomb explosion". The total amount of potential energy which is converted into kinetic energy of the two particles is called "kinetic energy release" (**KER**) and depends on the internuclear distance at the moment when ICD takes place (Figure 2.10).

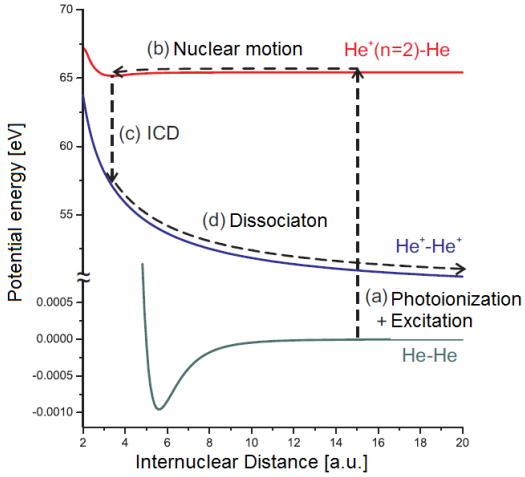

Figure 2.10: Dissociation of a helium dimer after ICD induced by photoionization and excitation into the n=2 excited $\mathbf{He_2^{+*}}$ state. Illustration is adapted from **[8]**.

The relation between KER and the internuclear distance is given by:

$$KER = \frac{e^2}{4\pi\epsilon\varepsilon_0 R} \tag{2.29}$$

while the momenta of the two ions are always antiparallel and of equal magnitude:

$$\vec{p}_1 = -\vec{p}_2 \tag{2.30}$$

Figure 2.11 shows the KER from the dissociation of helium dimers as found in [8]. The distribution shows a maximum at about 8.25 eV which corresponds to an internuclear distance of $R = \frac{1}{KER} \approx 3.25\ a.u.$ The KER distribution shows an intensity pattern for lower KER which is caused by vibrational excited modes in the singly charged dimer.
The outgoing ICD electron also shows a certain energy distribution. Due to energy conservation, the excitation energy is distributed to the ICD electron and the ionic fragments. In an energy correlation diagram this energy conservation creates characteristic line structures (Figure 2.11).

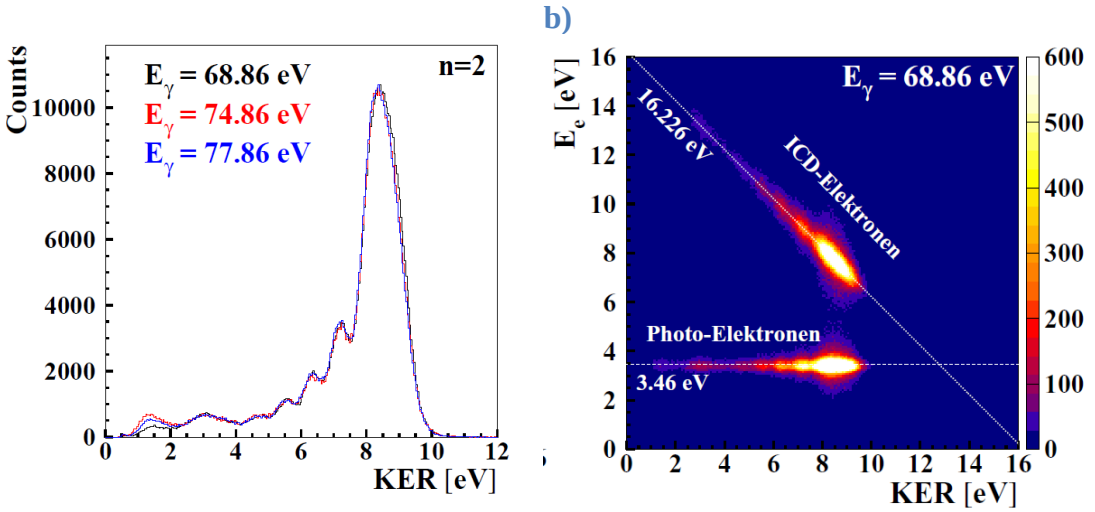

Figure 2.11: a) KER distribution for two helium ions emerging from a Coulomb explosion of a helium dimer after ICD. The peak structures on the left side of the maximum are due to vibrational excitation of the charged helium dimer. **b)** This picture shows the energy correlation between ICD electron and KER which is characteristic for ICD. Energy conservation creates a diagonal line with negative slope in this diagram. The diagrams are taken from **[8]**.

2.5.2 Fragmentation dynamics of helium clusters

Similar to helium dimers, helium clusters are also very loosely bound compounds which can be subject to ICD after single photon ionization and excitation with VUV radiation. Disregarding their quantum hydrodynamic properties as a superfluid, they can be treated in a naive way as an agglomeration of cold individual helium atoms. Every atom inside the cluster shares several of its next neighbor atoms with other atoms from the cluster. VUV photons can penetrate deep into the cluster and interact with helium atoms of the surface and the cluster core. If the photons induce ICD inside the clusters the Coulomb explosion of the created ion pair deposes a large amount of kinetic energy into the cluster ripping it apart. However, the exact ion dynamics inside the cluster is still not clear and is the main target of the experimental approach presented in this work.

Semi-classical simulations of the ion dynamics inside the cluster have been made in 2013 and 2014 by N. Sisourat [36] [37]. He solved the Hamilton's equations for all atoms and two helium ions inside clusters of fixed size. At the same time, he recorded the trajectories and the kinetic energies of the ions as well as the size of the fragments consisting of residual parts of the cluster sticking on them. For the interaction between the different particles simple potentials have been assumed. Starting from the Coulomb explosion the simulation uses the Coulomb potential to characterize the interaction of the two ions.

$$V_{Coulomb}(r) = \frac{1}{r} \tag{2.31}$$

The interaction between ions and neutral helium atoms is approximated with the Morse-potential:

$$V_{Morse}(r) = D_e\left(e^{-2\alpha(r-r_e)} - 2e^{-\alpha(r-r_e)}\right) \tag{2.32}$$

where D_e is the spectrometric dissociation energy which defines the depth of the potential, r_e is the equilibrium bond distance, the internuclear distance with the lowest potential energy, and α is a constant which describes the width of the potential.

The Lennard-Jones potential is employed to describe the interaction between two neutral particles:

$$V_{L.J.}(r) = 4\epsilon\left[\left(\frac{\sigma}{r}\right)^{12} - \left(\frac{\sigma}{r}\right)^{6}\right] \tag{2.33}$$

The initial distance of the particles to their equilibrium positions which are well known for Lennard-Jones clusters [38] is randomly varied within a Gaussian distribution. The initial velocities of the atoms are set to zero consistent with the fact that nuclear motion at these very low temperatures is almost frozen whereas the velocity of the ionic fragments after acceleration in the strong Coulomb potential is predominant. In this simulation no charge exchange between particles is included.

The simulation has confirmed a dependence of the fragment sizes on the size of the initial clusters (Figure 2.12) and has also revealed a correlation of the KER and both, original cluster size and fragment size. Large fragments carry less kinetic energy than smaller fragments while both energies are lower for bigger clusters (Figure 2.13). However, the comparison with the experiment is problematic because the size of the target clusters in [5] could not be clarified due to inaccurate temperature data.

In Figure 2.14 the simulated KER distributions of different sized cluster fragments done in [36] are compared to the experimental data presented in [5]. Both, experiment and simulation show a decreasing KER for larger fragments. However, the experimental results reported in [5] have revealed a significantly smaller KER than suggested by theory.

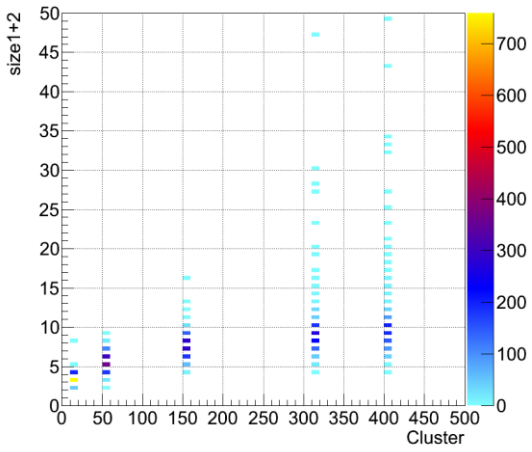

Figure 2.12: Sum of the fragment sizes for the fragmentation of helium clusters depending on the cluster size as simulated by **[36]**. Plot is taken from **[5]**.

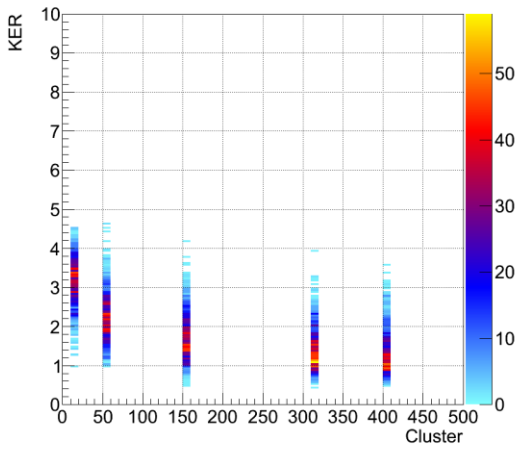

Figure 2.13: Simulated KER distribution for different sized clusters. Taken from **[5]**.

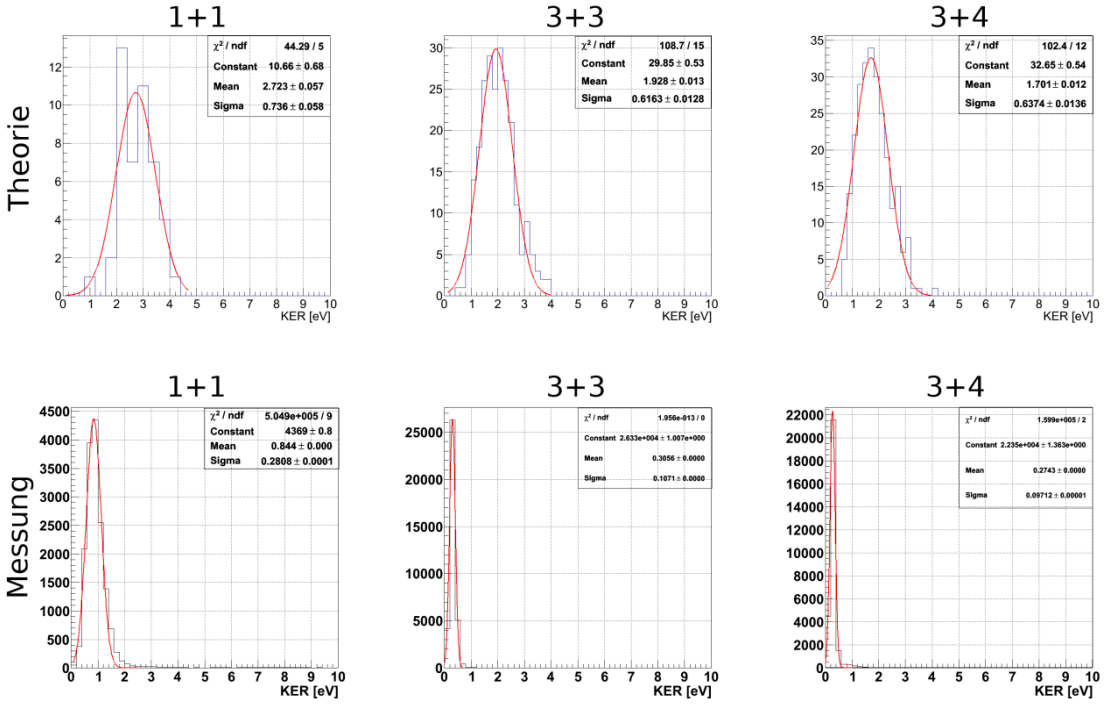

Figure 2.14: Comparison between simulated KER distributions **[36]** (1st row) and the experimental results in **[5]** (2nd row) for different fragmentation channels. The numbers on the top indicate the size of the fragments. In the 3+3 breakup channel the two fragments are singly charged helium trimers. (From **[5]**).

The reason for this discrepancy was object of speculation. C. Müller suggested several effects that could have led to an incorrect reconstruction of the KER or to an energy loss of the ionic fragments on their way through the cluster. He discussed several scenarios such as that the ionic fragments could have stripped off neutral particles before leaving the clusters or could have evaporated neutral atoms on their way from the interaction zone through the COLTRIMS setup to the detector. This would have caused an incorrect reconstruction of the KER from the recorded experimental data[1]. He also discussed the possibility that the ionic fragments have been scattered from neutral atoms inside the clusters. On base of his analysis of the underlying experimental data he came to the conclusion that this explanation is implausible due to the reconstructed momenta of the detected ions. As can be seen in equation (2.30) the momentum vectors of two ions after a Coulomb explosion are strict oppositely directed. If there is no deflection, the 180-degree angle between the two momentum vectors is preserved and can be measured in an ion momentum spectrometer.

The experimental data provided in [5] exhibit a very broad distribution of this breakup angle with an obvious maximum at 180 degrees (Figure 2.15). C. Müller interpreted this as an indication for the irrelevance of scattering processes for the observed energy loss. Nevertheless, new experimental data collected for this work reveal a characteristic and quantitative connection between fragment energy and breakup angle which brings scattering processes as a plausible explanation back into play.

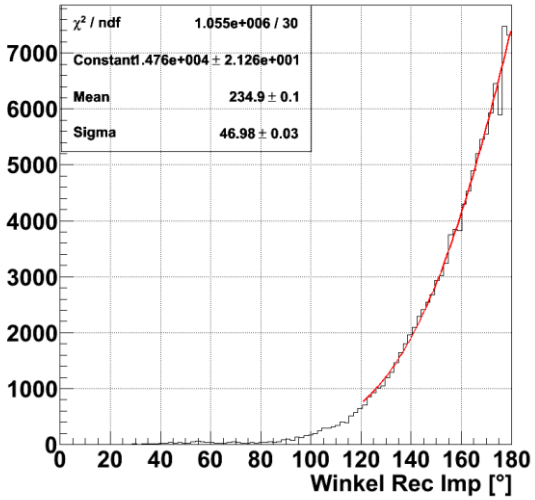

Figure 2.15: Distribution of the breakup angles between two ions as found in **[5]**. The distribution shows a distinct maximum at 180°.

[1]A variable fragment mass affects their time-of-flight which is an integral part of the KER reconstruction.

2.5.3 Elastic scattering

The experiment done in [8] has found a KER of about 8 eV for the ICD-induced dimer fragmentation. The initial kinetic energy of the fragment ions in case of a cluster fragmentation is therefore expected to be below 4 eV per ion. Considering the various excitation levels in helium (cf. Table 2.2), the fragment ions are not fast enough to transfer kinetic energy by impact ionization or impact excitation to neutral atoms. In case of ion scattering from a neutral cluster atom the kinetic energy carried by the projectile ion is shared with its collision partner. The residual energy of the ion fragment after an elastic scattering depends only on the mass relation of the collision partners and on the deflection angle of the projectile.

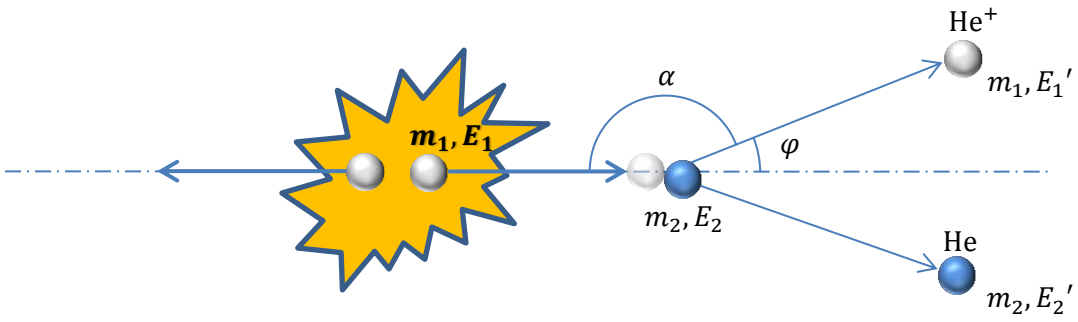

Figure 2.16: Elastic scattering of a fragment ion from a neutral cluster atom. Starting from the Coulomb explosion the two ions fly back-to-back. The angle $\boldsymbol{\alpha}$ between the momentum vectors can be measured by COLTRIMS.

The projectile energy after collision can be written as [39]:

$$E_1' = E_1 - \eta E_1 \tag{2.34}$$

$$\eta = \frac{2m_1 m_2}{(m_1 + m_2)^2}(1 - \cos(\delta)) \tag{2.35}$$

where δ is the scattering angle in the center of mass frame, while m_1 is the mass of the ion emerging from the ICD-induced Coulomb explosion and m_2 is the mass of its neutral collision partner before and after the collision. Due to the negligible thermal

motion in the cluster, the neutral collision partner is assumed to be initially at rest. For the reverse transformation into the laboratory frame the following relation applies:

$$\cos\delta = -\frac{m_1}{m_2}\sin^2(\varphi) + \cos(\varphi)\sqrt{1-\left(\frac{m_1}{m_2}\right)^2 sin^2(\varphi)} \tag{2.36}$$

where φ is the scattering angle in the laboratory frame (cf. Figure 2.16). By using the COLTRIMS method, the angle α between the momentum vectors of the detected fragment ions can be measured. After a Coulomb explosion the initial momentum vectors are strictly opposite. The altered projectile energy after a collision can therefore be expressed relative to α as (Figure 2.17):

$$E_1'(\alpha) = E_1 - \frac{2E_1 m_1 m_2}{(m_1+m_2)^2}\left(1+\frac{m_1}{m_2}\sin^2(\pi-\alpha) - \cos(\pi-\alpha)\sqrt{1-\left(\frac{m_1}{m_2}\right)^2 sin^2(\pi-\alpha)}\right) \tag{2.37}$$

Due to the extremely weak bond[1] of the neutral helium atoms to their neighbors in the cluster, the elastic scattering of the fragment ions from cluster atoms can be treated as an interaction of an ionic fragment with just single helium atoms from the cluster (2.38).

$$\frac{m_1}{m_2} \geq 1 \tag{2.38}$$

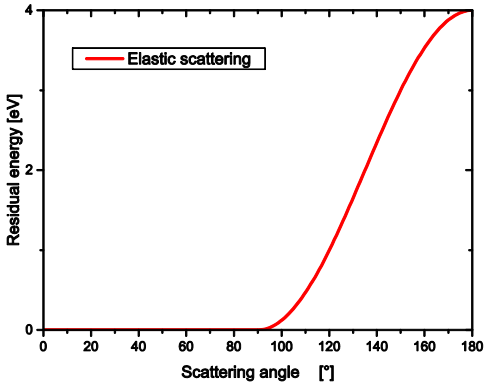

Figure 2.17: Residual energy $\boldsymbol{E_1'}$ of the fragment ion after ion-atom elastic scattering in case of $\boldsymbol{m_1 = m_2}$. The projectile energy is set to $\boldsymbol{E_1 = 4\ eV}$.

[1]The binding energy of helium atoms in the cluster is about 7000 times smaller than the projectile energy.

Chapter 3

Experimental setup

This chapter describes the experimental setup. It presents the COLTRIMS apparatus used for this experiment as well as the experimental facility at which this experiment has been carried out. A general overview on the physical conditions during the experiment as well as on the data acquisition will be given in this chapter. The focus is set on the three essential components of the experimental setup, namely, the cold gas target, the projectile source which is the BESSY II synchrotron light source, and the momentum spectrometer.

3.1.1 Supersonic gas jet

In order to minimize background events, it is essential to enclose the spectrometer in an ultra-high vacuum. This also allows the projectile photons from the synchrotron light source to reach the target zone unabsorbed. A molecular gas jet is used to provide a sufficiently dense and localized gas target in middle of this ultra-high vacuum environment. Such supersonic gas jets can travel across vacuum chambers without contaminating the vacuum. The supersonic gas jet can then be intersected with the photon beam creating a localized interaction zone in the center of the momentum

spectrometer (Figure 3.3). As described in 2.2.1, the jet is formed in an adiabatic expansion of pressurized gas streaming through a thin nozzle. The nozzle used in this experiment has a diameter of 5 µm and is attached to a flow cryostat which can be cooled with liquid helium. The temperature of the cryostat (CRYO INDUSTRIES, RC110H) is electronically controlled by a cryostat controller (CRYOCON, 32B) which regulates the temperature by using a heating element and two temperature sensors. The cryostat provides a very good temperature stability of ± 0.1 K in the temperature range of 10 to 15 K which is applied in this experiment. A thin stainless steel gas supply line leads from the nozzle to the outside of the chamber and can be pressurized with helium gas. To prevent contaminants in the helium gas such as residual water from freezing and blocking the tiny nozzle, the helium gas is led through a liquid nitrogen cooled filter. The gas pressure is regulated by a single stage pressure reducer attached to a high purity (99.9999 %) helium gas cylinder. To provide a better pressure measurement, a digital manometer is additionally connected to the supply line.

3.1.2 Creation of helium clusters

Depending on the desired cluster size the stagnation pressures and the nozzle temperatures are set to fixed points between 10 K and 15 K and 1.5 to 25 bar defining the starting conditions for the adiabatic expansion (Figure 2.4). If the precooled gas exits the nozzle, it expands and creates a supersonic shock wave in front of the nozzle.

a) **b)**

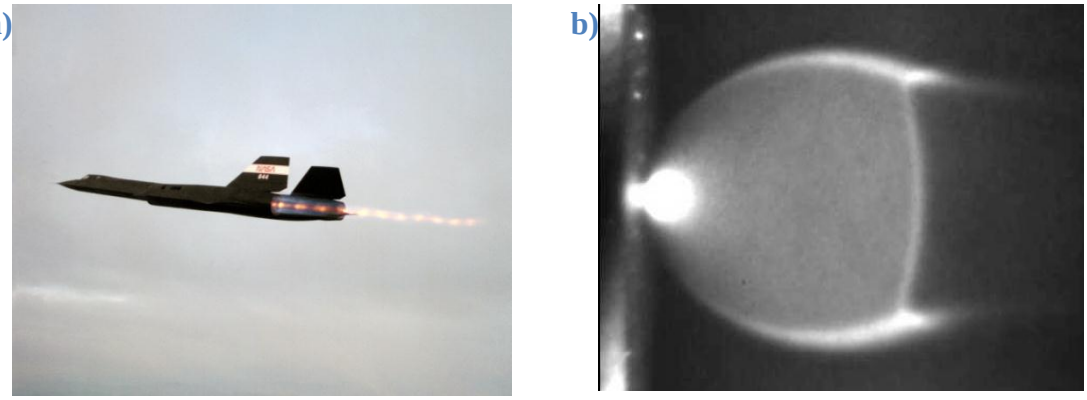

Figure 3.1: a) Lockheed SR-71 blackbird during a supersonic flight. **b)** A nitrogen gas jet leaving a nozzle. The space behind the nozzle and before the gas reaches the first Mach disc is called zone of silence.

This effect is well-known from jet engines when hot exhaust passes through the nozzle behind a turbine and creates a characteristic, glowing exhaust plume which can be referred to the creation of so-called Mach diamonds.

The gas inside the nozzle has a higher pressure then the ambient pressure. As a result, the gas expands into the vacuum (Figure 3.2). While exiting the nozzle, the supersonic stream creates oblique shock waves on the edges of the nozzle which are inclined at an angle to the direction of the flow **(1)**. These waves guide the flow while it turns outwards and reduces its internal pressure **(2)**. The shock waves then hit their equivalent from the other side of the nozzle **(3)** and are reflected from them towards the free jet boundary[1]. The shock waves then travel through the flow until they reach the contact discontinuity between gas jet and vacuum where they are reflected and focused back inwards again **(4)**. If the back focused shock waves are strong enough, they can merge and create a so-called compression fan **(5)**. Passing through this series of shock waves the supersonic gas flow is pent up by the compression fan creating a normal shock front[2]. Temperature and pressure inside this shock front increase dramatically while the first Mach disk is formed **(6)**. The temperatures and pressures inside this shock cause the gas to expand again and the process repeats itself [40] [41] [42]. The space between the nozzle and the first shock diamond is called "zone of silence" which has a length x of approximately:

$$x = 0.67\, D_0 \sqrt{\frac{P_0}{P_1}} \tag{3.1}$$

where D_0 is the nozzle diameter, P_0 is the flow pressure and P_1 is the ambient pressure.

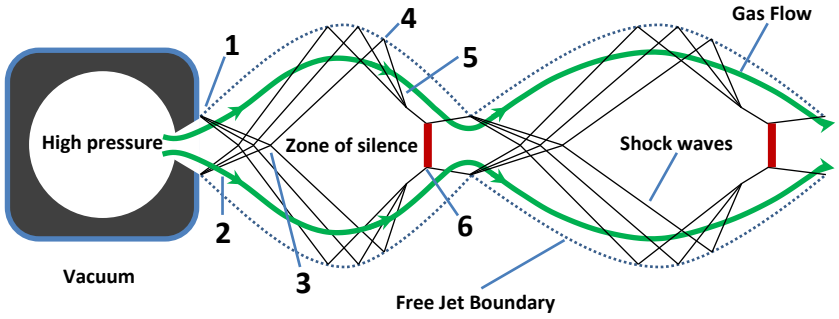

Figure 3.2: Expansion of high pressured gas into vacuum. Adapted from **[40]**.

[1] The free jet boundary marks the contact discontinuity between the free gas jet and the vacuum.
[2] Shock waves propagating perpendicular to the direction of the flow are called normal shock waves.

For this experiment the zone of silence is of particular importance because the temperature of the adiabatic expansion reaches its minimum inside this zone. Temperatures can drop below 1 mK which is essential for the formation of helium clusters. In order to prevent the gas from heating up again by getting hit from shock waves, the gas stream inside the zone of silence containing the clusters has to be extracted. This can be achieved by using a small conically shaped “skimmer”. This tiny metal funnel is placed in front of the nozzle with its narrow side pointing towards the gas stream extending into the zone of silence. The gas jet then passes the skimmer shielded against shock waves and forms a narrow beam of cold gas. In this experiment two copper skimmers of 300 µm diameter[1] are used in a cascade to direct the jet into the main vacuum chamber hosting the momentum spectrometer. Inside the spectrometer the jet is brought to an overlap with the projectile beam creating a small interaction volume. After passing through the interaction zone, the gas stream is dumped on the other side of the vacuum chamber. In this experimental setup the jet dump is built of two nested thin metal tubes which prevent a backflow of gas into the main chamber. The pressure inside the two stages of the jet dump can be measured with pressure gauges to monitor the gas throughput.

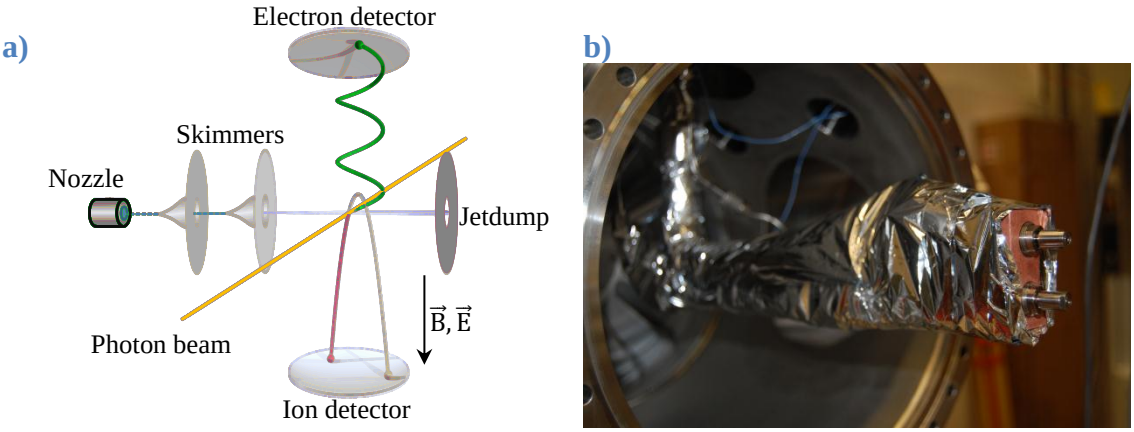

Figure 3.3: a) Schematic representation of a typical gas target experiment at a synchrotron light source. The gas jet is created in a free jet expansion into the vacuum. A narrow gas stream is then cut out from the zone of silence by using two conically shaped skimmers. The supersonic jet is then intercepted by the photon beam defining the reaction volume before it gets dumped in the jet-dump. **b)** The nozzle used in this experiment. Two nozzles of different sizes are mounted on a horizontal copper nozzle holder which is attached to the cryostat.

[1] At the narrowest spot. The skimmers used in this experiment are hyperbolic-shaped.

3.2 Synchrotron radiation

As mentioned before, the projectile beam in this experiment consists of extreme ultraviolet photons. Photons as projectiles are an important tool to study the physical properties of molecules and atoms. Nevertheless, the construction of a tunable VUV light source of high spectral purity and intensity as well as defined polarization is challenging and requires advanced techniques.

Only a few suitable VUV generation techniques exist such as rare gas discharge, laser high-harmonics generation and synchrotron light sources. The principle of generating synchrotron radiation is based on the effect of bremsstrahlung which is emitted from accelerated or decelerated charged particles.

At the BESSY II synchrotron in Berlin (Figure 3.5) which is used as a light source for this experiment, electrons are accelerated to relativistic energies of up to 1.9 GeV, bunched together into buckets, and directed into an electron storage ring and onto a circular path by a series of strong bending magnets. While flying through the magnetic field, these electron bunches are deflected and, as a result, emit photons tangentially to the Lorentz force. In many synchrotrons the electrons also pass through so-called undulators located between two consecutive bending magnets. These devices which are consisting of a series of magnets with changing polarity direct the particles onto a sinusoidal trajectory causing them to emit photons on their path (Figure 3.4).

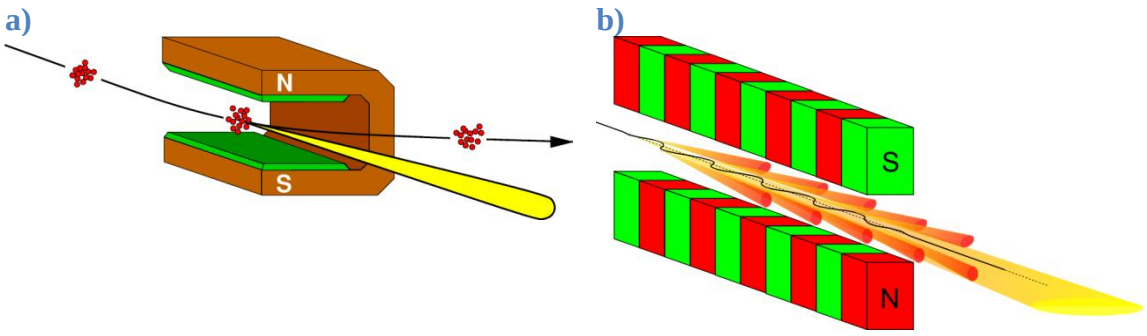

Figure 3.4: a) Electron bunches flying through a bending magnet. **b)** Undulator. Due to relativistic effects, synchrotron radiation is emitted in a narrow cone tangentially to the Lorentz force.

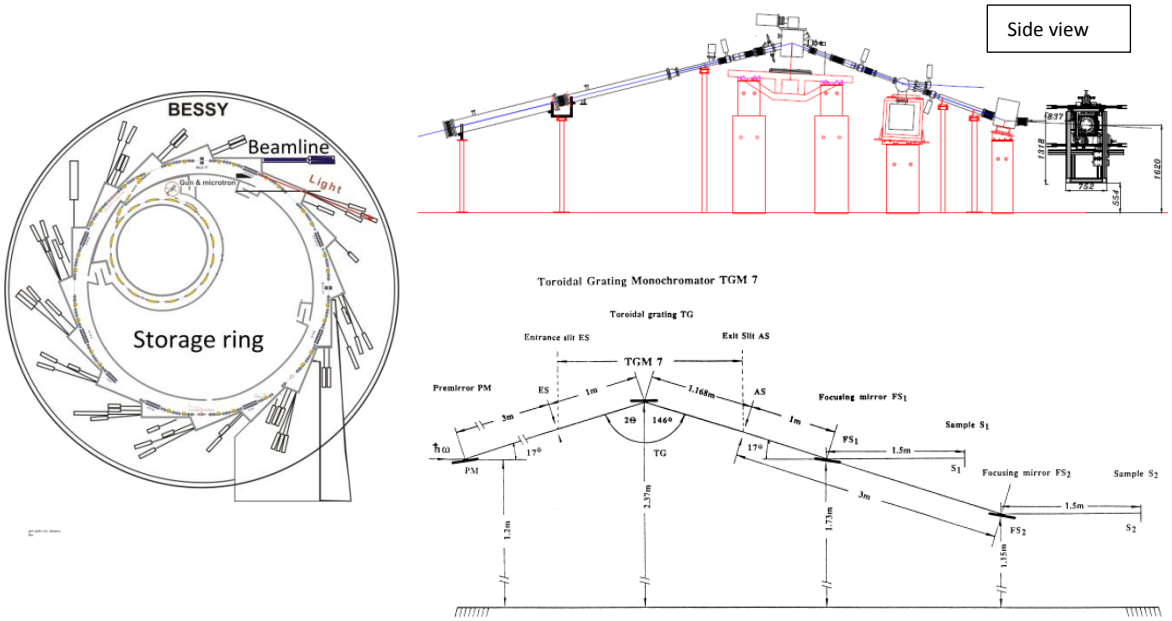

Figure 3.5: Schematic of the BESSY II synchrotron building. Blueprint of the experimental chamber attached to the TGM-7 beamline (right).

Due to the electron bunching, the light coming from the synchrotron is not continuous but pulsed. Depending on the number of electron bunches stored together in the synchrotron ring, the time spacing between two light pulses changes. This experiment uses the "single-bunch mode" of BESSY II with a time spacing of 800 ns between two light pulses of 20 ps pulse duration.

The emitted light covers a very broad spectral range from visible light to hard X-ray radiation which is why this "white light" has to be filtered for the desired photon wavelength. This is done by placing diffraction gratings and metal filters into the optical beam path.

The photon energy in this experiment is set to 67.65 eV slightly above the ICD threshold (cf. equation (2.26)). The experimental chamber is attached to the TGM-7 (**T**oroidal **G**rating **M**onochromator-7) beamline of BESSY II (Figure 3.5). This beamline uses the synchrotron light coming from a bending magnet and covers almost the whole VUV spectral range of photon energies from 8 eV to 120 eV with a relative energy resolution of ±0.2 %. The photon beam is horizontally polarized and provides a total photon flux[1] in the order of 10^{13} photons per Å and second depending on the beam current in the electron storage ring, the desired wavelength and energy resolution [43].

[1] Integrated over the entire beam profile.

3.3 COLTRIMS

A COLTRIMS setup consists of three fundamental parts, first of all the momentum spectrometer consisting of several electrodes and a pair of Helmholtz coils creating electric and magnetic fields to guide and separate charged particles according to their momenta, secondly the detectors mounted on both ends of the spectrometer and thirdly a vacuum-chamber which encloses the spectrometer.

Corresponding to their momenta and charge, particles which exit the interaction zone are guided by electric and magnetic fields to different spots on two position and time resolving detectors. By measuring the "time-of-flight" (**TOF**) of the charged particles inside the spectrometer field and their position of impact on the detectors, the initial momenta can be entirely reconstructed.

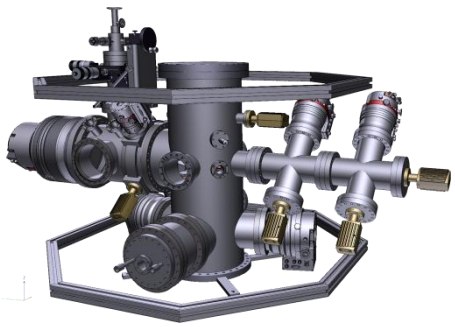

Figure 3.6: CAD-model of the vacuum chamber.

3.3.1 The spectrometer

The momentum spectrometer is unarguably the centerpiece of every COLTRIMS setup. Its geometrical design determines the momentum range, momentum resolution and the covered solid angle for the detection of ions and electrons leaving the interaction zone. The spectrometer used for this experiment consists of 62 thin phosphor bronze plates (150 × 150 × 0.25) mm with a center hole of 120 mm which create a homogeneous electric field in a certain part of the spectrometer.

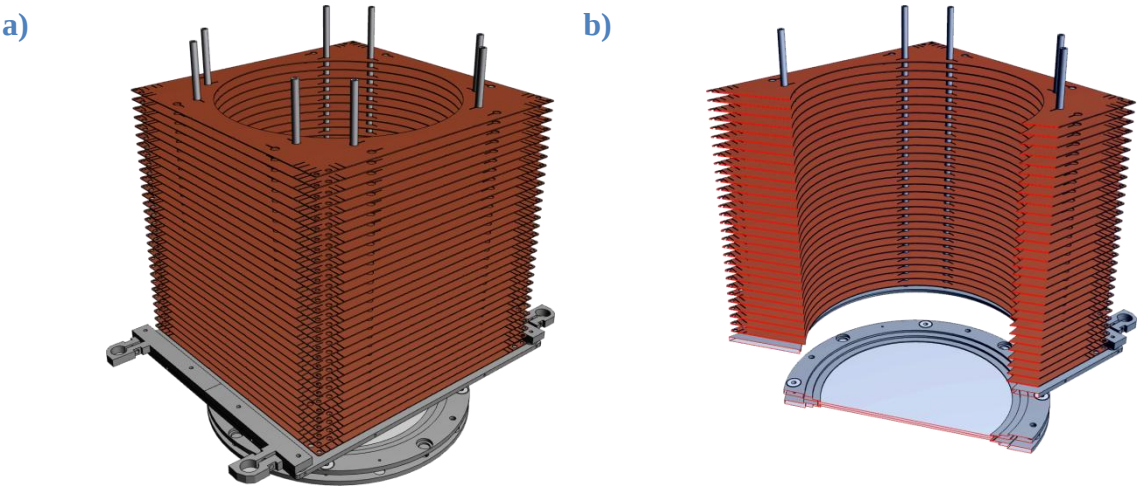

Figure 3.7: a) CAD-model of the momentum spectrometer. The spectrometer plates are lined up on eight ceramic rods. b) Sectional view of the spectrometer and the detector.

The metal plates are lined up on eight ceramic rods with insulating ceramic spacers between them keeping a distance of 5 mm from plate to plate (Figure 3.7). Each plate is connected with a 100 kΩ[1] resistor to the following plate (Figure 3.8).

By applying a voltage to both ends of the spectrometer, a constant current runs through all resistors and creates a constant voltage drop over each resistor which sets the spectrometer plates on a defined potential. This potential creates a homogeneous electric field from one end to the other end of the spectrometer. When the target zone where the photon beam crosses the gas jet is placed inside this field, charged particles are extracted from this zone. Depending on their charge, the field separates electrons and ions and guides them into opposite directions. Looking from the position of the target zone, the part to which the electrons are led is called the "electron arm" while the other side is called "ion arm".

In addition, sections with constant potential are added behind the acceleration regions of both arms. These sections of the spectrometer contain no electric field so that charged particles drift inside these regions until they reach the detectors. The interplay between length of each acceleration section and drift section determines the time focusing capabilities of each arm.

[1] The variation of the resistance of a few selected resistors results in an inhomogeneous electric field at that spot which can be desired in some cases.

A spectrometer geometry is called time-focusing if charged particles with equal momenta starting at different spots inside the interaction zone hit the detector at the same time. This time-focusing geometry is required because the interaction zone has a finite spatial extent. Thus, particles which start from a spot closer to the detector pass through a smaller potential difference than particles starting farther away. These particles are therefore accelerated over a longer distance reaching higher velocities before they can finally catch up with the slower particles at a certain spot inside the drift region. The particles hit the detector at the same time if the detector is placed on that specific spot. A frequently used time-focusing geometry which fulfills this condition is the so called "1:2"- or "Wiley McLaren-geometry" where the drift region has twice the length of the acceleration region of the corresponding spectrometer arm. The exact length of each arm as well as the spectrometer field has to be chosen such, that the desired 4π solid angle of acceptance for ions and electrons with the expected kinetic energies in this experiment is achieved.

The spectrometer used in this experiment has an ion acceleration length of 35.5 mm with a subsequent drift of 75.2 mm. The electron acceleration section opposite to the ion acceleration is 74.5 mm long and is followed by a drift of 161.5 mm (Figure 3.9).

To create regions of constant electric potential the bronze plates in the drift regions are short-circuited instead of being interconnected with resistors. The field-free drift zones are separated from the acceleration regions and the detectors by thin metal meshes with a 140 µm mesh opening which provide more than 78% transmission.

Figure 3.8: Resistors which connect the spectrometer plates.

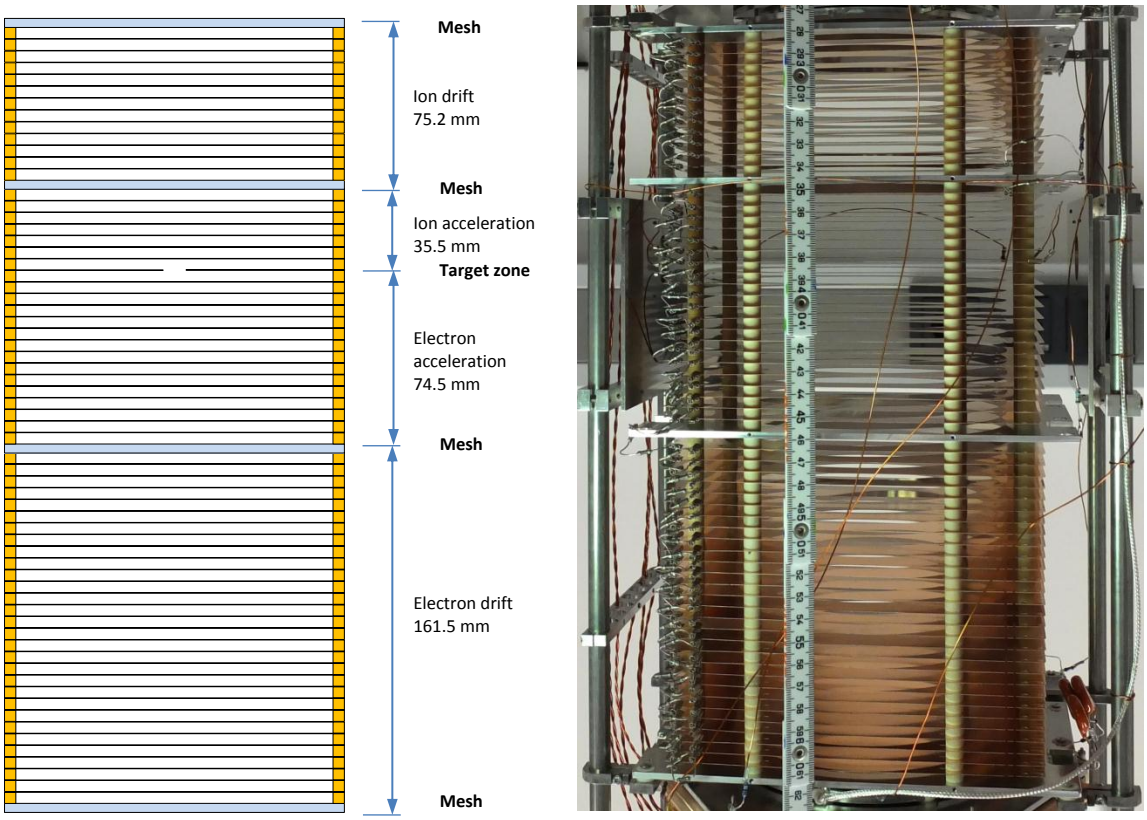

Figure 3.9: Sketch of the momentum spectrometer used in this experiment (left) and fully assembled spectrometer (right).

To prevent fast electrons with initial momentum vectors perpendicular to the electric field from leaving the spectrometer, the electrons are forced onto a spiral trajectory along the electric field vectors by superposing the electric field with a homogeneous magnetic field of several Gauss[1]. The field is induced by a pair of large Helmholtz coils which surround the whole vacuum chamber. Each coil has a diameter of 150 cm with 16 windings of an insulated copper pipe. The distance between the two coils amounts to 70 cm according to the Helmholtz condition[2]. Water flowing through the conductive copper pipes prevents them from heating up during operation. A high current of about 33.8 Amperes flows through the coils and creates a sufficiently strong magnetic field. The magnetic field inside the spectrometer is estimated with 6.63 Gauss. However, the magnetic field found in the field calibration in chapter 4.6.2 is almost 6% weaker.

[1] See also chapter 4.6.2

[2] The Helmholtz condition is fulfilled if $\nabla \times \vec{\mathbf{B}} = 0$.

3.3.2 The detectors

As the charged particles fly inside the spectrometer, they are dispersed in time as well as in the spatial direction according to their initial momenta and masses. The detectors on both ends of the spectrometer are built to identify the position and the instant in time when the particles hit the detector plane after having passed through the spectrometer field. For this reason, time- and position-sensitive detectors are used which are composed of a position-sensitive delay line detectors together with two pairs of cascaded micro-channel-plates (**MCP**s) in front of each delay line detector. The MCPs serve as a charge amplifier for the delay line detectors and as a time-sensitive detector. The charge of single ions and electrons is several orders of magnitude too small to be detected. Thus, an amplification of the incoming charge is indispensable to induce measurable signals in the delay lines. The MCPs used for this purpose are thin glass plates of 80 mm diameter perforated with thousands of small channels. These micro tubes have a diameter of about 25 µm with a spacing of 32 µm between each tube. The channels pierce the plates inclined at an angle of 8 degrees to the surface normal of the MCPs and are coated with a semiconductor from the inside. To set the front and back side on a potential of a few kilovolts both sides are coated with a thin metal film. If a particle hits the semi conductive coating inside the micro channels with a sufficiently high energy, secondary electrons are emitted from the surface and experience acceleration in the high potential inside the channels. When these electrons keep hitting the walls of the tilted tube, more and more electrons are detached and create an electron avalanche which exits the MCP on the back side (Figure 3.10). This multiplication effect increases the effective charge by a factor in the order of 1000. In order to enhance the gain even more two MCPs are stacked in this experiment.

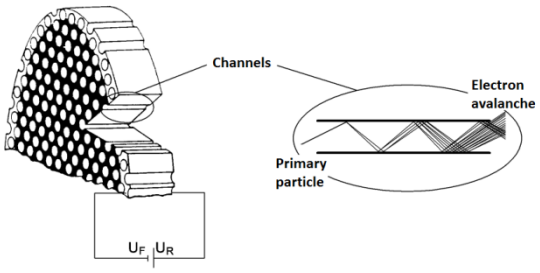

Figure 3.10: Illustration of a micro-channel-plate (MCP). Illustration adapted from **[5]**.

An electron burst on the MCPs leaves a charge deficiency which can be coupled out and serve as a voltage signal for the time-of-flight measurement.

To determine the exact position of a hit on the MCPs, a delay line anode serves as a position-sensitive detector. Each delay line anode used in this experiment consists of three pairs[1] of long and thin copper wires. The different wire pairs are wrapped around an insulating hexagonal frame creating three different layers of windings which are rotated by 120 degrees with respect to each other (Figure 3.11). The anodes are placed behind the MCPs. If an electron avalanche leaves the back side of the MCPs and hits a wire pair of the anodes on a certain spot, a signal is induced in the line which propagates to both ends of the wire pair. Due to the finite propagation speed and depending on the impact position, the signal reaches each end of the delay line at a different time. The exact position of the hit on the wrapped delay line can be reconstructed by measuring the difference of the signal propagation times to both ends of the wires.

a) **b)** **c)**

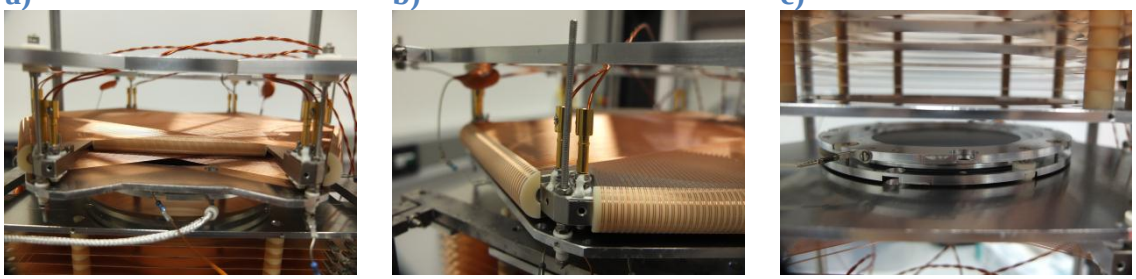

Figure 3.11: a) Delay line anode. **b)** Paired delay lines. **c)** Stacked MCP on top of the delay line anode.

In this experiment two different types of delay line detectors are used. The electron side of the spectrometer is equipped with a hexagonal delay line anode (“Hex-Anode”) while the ion side uses a detector which consists essentially a hexagonal anode but with two long and one shortened layer (Figure 3.11a).

The anodes are set on a positive potential relative to the back side of the MCP to suck away the electron avalanche leaving the MCP stage. One of the paired delay lines lies on a slightly higher potential whereby electrons tend to create a signal just on this wire. Electromagnetic interferences have a uniform influence on both wires and can be averaged out by means of signal subtraction.

[1] Using paired wires as Lecher lines instead of single wire Goubau lines improves the high frequency capabilities of the delay line as well as the susceptibility by means of differential amplification.

3.3.3 Signal processing and data acquisition

The raw analog timing signals arising from each hit on the detectors are processed through a series of intermediate steps for the final fully automated digital data acquisition and storage. First up is the amplification of the weak signals coming from the detectors on both spectrometer arms by a fast pre-amplifier (**FAMP**). The differential amplification of the anode signals is implemented with a broad band signal transformer followed by a FAMP. After obtaining usable signals they are passed to constant fraction discriminators (**CFD**s) in order to produce digital norm timing signals which can be interpreted by the subsequent digital logic. The CFDs act as voltage discriminators which perform a signal transformation of incoming "analog shaped" pulses of varying height but almost constant width to sharp rectangle pulses with a constant height (**NIM** pulses). The outgoing NIM pulses occur in a fixed timing relation to the peak maximum of the incoming analog pulses independent of the actual pulse height.

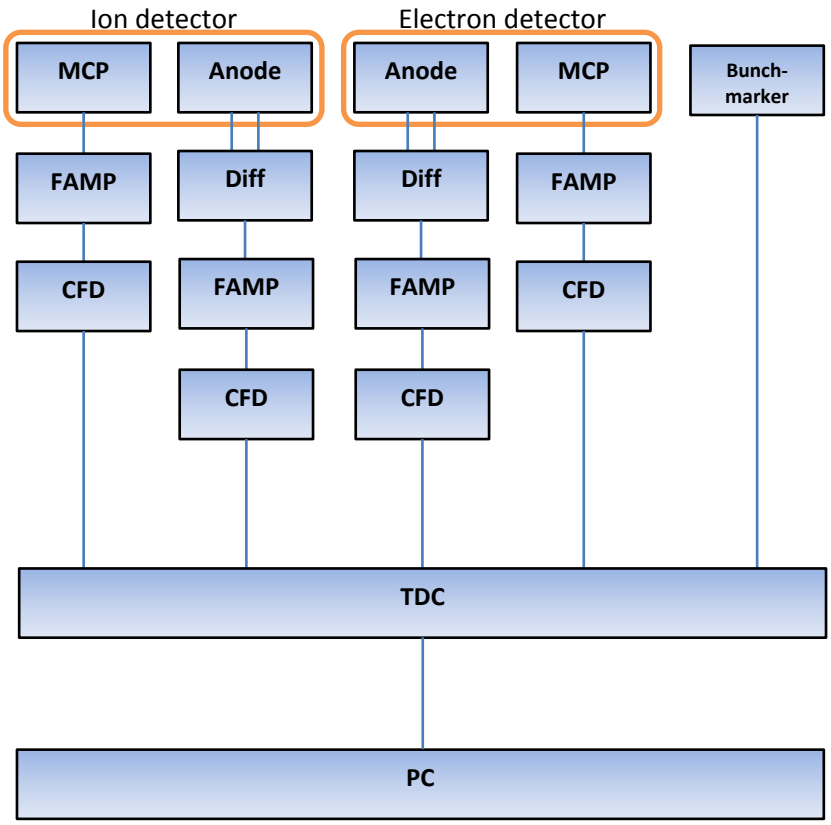

Figure 3.12: Block diagram of the signal processing and data acquisition.

The NIM pulses are then sent to the time to digital converter (**TDC**). The TDC device in this experiment is realized with two stacked PCI express cards which provide a 16-channel interface to the measurement PC. The TDC converts the time difference between each incoming NIM signal and a reference signal to a digital value which is then handed over to the PC.

In this experiment all twelve signals coming from the delay line anodes (two ends of the three layers on each detector), two signals coming from the MCPs and the "bunchmarker" signal are fed into the TDC. The bunchmarker signal is synchronized with the electron bunch circulating inside the storage ring. It is provided by the synchrotron light source and marks the instant[1] when a light pulse is sent through the beamline to the experiment. Thus the bunchmarker serves as a reference signal for the time-of-flight measurement. The large number of hits on the detectors can be delimited to events that, for instance, produce pairs of ions which hit the ion detector in coincidence by adding logic AND gates in combination with delay stages creating a defined time window for a double hit.

In this experiment the timing data of every event is recorded by the TDC while the gating on coincidences is done by the data acquisition software. The used software (COBOLD and LMF2Root) is capable of extracting the positioning and timing information for the reconstruction of the detector images and the time-of-flight measurement. All timing data are written to a list mode file which then undergoes further data processing and analyzing steps described in the next chapter.

[1]The constant temporal offset between bunchmarker and light can be subtracted afterwards.

3.3.4 Experimental chamber

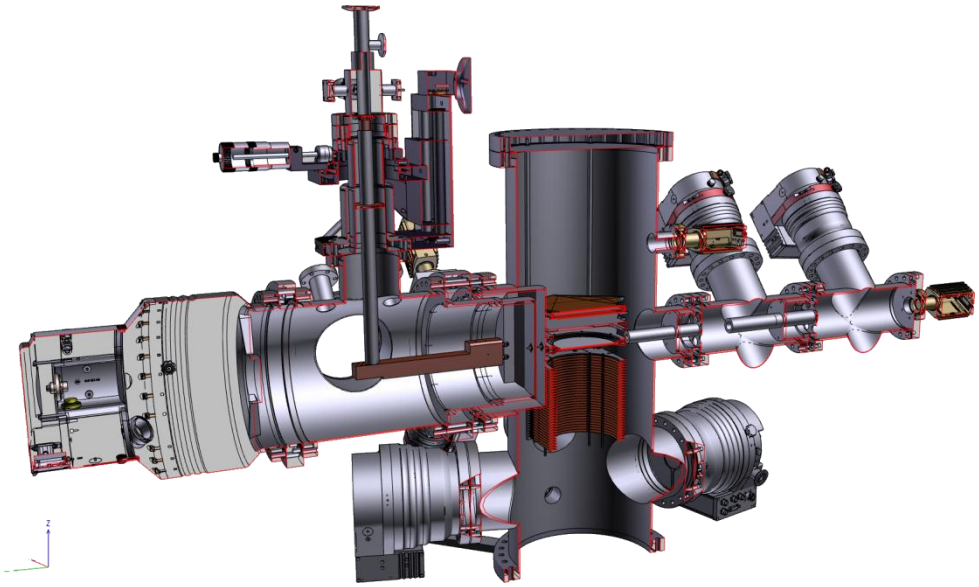

Figure 3.13: Lateral cut through the CAD-model of the vacuum chamber.

As mentioned before, an ultra-high vacuum is essential for the operation of the detectors and to minimize the interaction of the VUV photons with the residual gas inside the chamber. The vacuum system is built of three subunits, namely the two-stage expansion chamber, the main chamber and the two-stage jet dump. The supersonic gas jet is formed inside a two-stage expansion chamber which is separated from the main chamber by a “cup-shaped” partition which holds the two skimmers. A HiPace® 2300 turbo pump provides 1900 l/s of pumping speed to maintain a good vacuum in the first expansion stage while a gas load is applied through the nozzle during jet operation. First and second expansion stages are modeled as two nested cups creating a volume between them. The HiPace® 80 turbo pump which evacuates the volume between the two cups has a pumping speed of about 67 l/s. The nozzle is mounted on an L-shaped cryostat extending into the first expansion chamber. The whole cryostat is mounted on a linear xyz-manipulator stage which allows moving the nozzle in front of the skimmers. The jet dump is located right opposite to the expansion chamber and is built of two CF-100 crosses. The two stages of the jet dump are nested. Small differential tubes between them reduce the backflow of gas into the main chamber. Each stage is equipped with a HiPace® 300 turbo pump which provides a pumping speed of 260 l/s.

The main chamber is evacuated with two HiPace® 700 turbo pumps which in turn provide a pumping speed of about 690 l/s each. To attain an ultra-high vacuum, the main chamber is heated up to temperatures above 100 °C to evaporate adhesive water from all surfaces. In addition, a cold trap is installed on the main chamber which is filled with liquid nitrogen to freeze out residual water vapor and improve the vacuum. To analyze the residual gas (and for jet optimization), mass spectrometers are mounted on the target chamber and the jet dump. During jet operation, the pressure in the main chamber (target chamber) is in the order of 10^{-10} mbar. The vacuum in the synchrotron beamline though is one order of magnitude lower, which is why a differential pumping stage is used to connect the target chamber to the beamline. The differential stage is built out of two evacuated volumes which are connected through a differential tube. This tube inhibits the gas flow between the two pumped volumes but lets the photon beam pass through. The differential stage is connected to the beamline from one side while the other side is connected to the target chamber through an aperture. The aperture maintains a pressure gradient between the differential stage and the target chamber. The volumes are pumped separately by two TMH 260 turbopumps which each provide a pumping speed of 210 l/s.

To build up and maintain a sufficiently good rough vacuum for the operation of the turbo molecular pumps, a combination of rootspump and scrollpump is used as a pumping station. The following chart shall give an overview on typical values for the vacua in the different chamber sections during the experiment.

Section	Pumping speed	Vacuum
Expansion 1	1900 l/s	$2.2 \cdot 10^{-4}$ mbar
Expansion 2	67 l/s	$2.5 \cdot 10^{-6}$ mbar
Target chamber	2 x 690 l/s	$7.9 \cdot 10^{-10}$ mbar
Jet dump 1	260 l/s	$1.2 \cdot 10^{-9}$ mbar
Jet dump 2	260 l/s	$1.6 \cdot 10^{-8}$ mbar
Differential stage	2 x210 l/s	$1.0 \cdot 10^{-9}$ mbar

Table 3.1: Vacua during operation of a 25 bar/12K helium jet.

3.4 Handling the experiment

As mentioned before, the experiment was carried out in January 2014 at the synchrotron BESSY II in Berlin. After the transport of the experimental setup along with all necessary equipment the first step was to move the chamber to the beamline and bring it to an exact alignment with the photon beam. A thorough alignment is crucial because the intersection of jet axis, spectrometer axis and the µm sized focus of the photon beam defining the interaction region must be centered inside the spectrometer. More importantly, a bad alignment entails the risk of hitting metal parts of the chamber and the spectrometer with the VUV beam creating a vast amount of secondary electrons. A reference line was provided on the floor right in front of the beamline which marks the optical axis of the photon beam and was used to line up an optical theodolite. The alignment was checked by using the zero order white light of the monochromator.

As a second step the helium jet was brought to alignment with the jet dump by moving the nozzle in front of the skimmers and by maximizing the pressure in the second dump stage as well as the readout of the mass spectrometer for helium. After these setup processes, the COLTRIMS system is started up for calibration measurements.

The spectrometer field is set to **18.27 V/cm** by applying negative potentials of -408 V on the end of the ion side and -207 V on the electron arm. By pulling the whole spectrometer to a negative potential (the potential of the vacuum chamber defines GND ≡ 0 V), electrons from outside the spectrometer are repelled. The MCP front sides are set on a negative bias of -1943 V on the ion side and -70 V on the electron side while the ion delay line anode is brought to +163 V and the electron anode to +1920 V. The electric current running through the Helmholtz coils is adjusted to 33.8 A.

To calibrate the photon energy of the beamline, the wavelength is “scanned” over the helium ICD threshold. As explained in more detail in chapter 4.6.1, the comparison of the displayed energy with the energy at which helium double ionization can be observed reveals the energy offset of the beamline.

For the measurement this beamline offset has to be taken into account. All values for the photon energy given in this work are already adjusted to the beamline offset so they display the real photon energy. The photon energy is scanned once again in order to take a reference measurement for an energy calibration of the electron spectrometer.

After the calibration measurements the actual experiment on helium clusters is performed. Therefore, the cryostat is cooled down to temperatures of approx. 10 K. The following Table 3.2 shall give an overview on the different settings for temperatures and pressures applied to the cluster source during the one week beamtime.

During the experiment the synchrotron is operated in "top-up" single-bunch mode whereas the current inside the synchrotron storage ring is held constant.

To create low energetic photoelectrons from the $\mathbf{He}_2^{+*}(n=2) + e_{photo}^-$ ionization and excitation, the photon energy is set to **67.65 eV** slightly above the ICD threshold for helium dimers at 65.4 eV (cf. equation (2.26)). The photon flux is regulated by adjusting the width of the exit slit behind the monochromator (Figure 3.5) to limit[1] the hit rate on the electron detector to 25 kHz. In this case the ion detection rate reaches values of about 1 kHz up to 5 kHz. For some settings displayed in Table 3.2 the photon energy is as well tuned to 25 eV to estimate the cluster size distribution of the target. This photon energy is chosen slightly higher than the single ionization threshold at 24.59 eV in order to produce singly charged clusters for a time-of-flight mass spectroscopy without producing high energetic photo electrons which could potentially interact with the clusters in a destructive way.

The mean cluster sizes listed in (Table 3.2) are estimated according to the experimental results from [19] (see also chapter 2.2.1) because they provide a good estimation of the mean cluster sizes for the widest temperature and pressure range.

Measurement	Photon energy	Mean Cluster size N	P_0 / T_0
I	67.65 eV	2	1.5 bar / 12.4 K
II	67.65 eV, 25 eV	5000	10 bar / 12.4 K
III	67.65 eV, 25 eV	6500	25 bar / 14.5 K
IV	67.65 eV, 25 eV	15000	25 bar / 12.0 K
V	67.65 eV	30000	25 bar / 11.6 K
VI	67.65 eV	200000	25 bar / 11.1 K
VII	67.65 eV	>200000	25 bar / 10.8 K
VIII	67.65 eV	3500000	50 bar / 10.8 K

Table 3.2: Mean cluster sizes in distinct measurements estimated according to **[19]**.

[1] An excessively high impact rate on the MCP causes loss of efficiency so-called "efficiency-holes"

Chapter 4

Data processing and analysis

This chapter will guide the reader through the processing and calibration of the raw data accumulated during the experiment. By processing the raw ".lmf" (list mode file) data the momenta and the energies of the detected fragments are reconstructed from the positions of impact on the detectors and the time-of-flight information collected for each hit on the detectors and saved in a ".root"-file for subsequent analysis and plotting. Together with an exact calibration and presorting it forms the foundation of all following interpretation of the data.

4.1 Coordinate Systems

A Cartesian coordinate system serves as a frame of reference. Its origin is placed in the intersection of jet axis, photon beam axis and an axis parallel to the surfaces normal of the detectors. The direction of the photon beam marks the x-axis while the jet points in y-direction. The z-axis is also called the "time-of-flight axis" and is defined by an axis through the electron detector pointing vertically towards the ion detector. The z-axis is oriented perpendicular to the horizontal polarization plane of the synchrotron light.

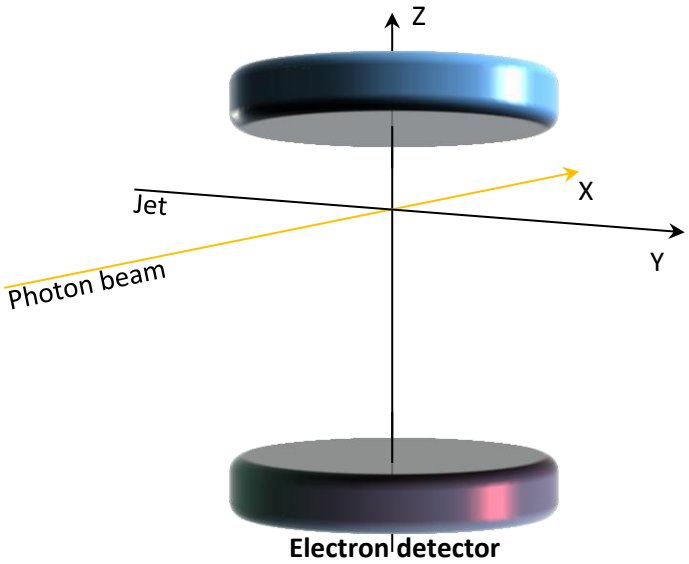

Figure 4.1: Cartesian coordinate system used as a frame of reference. The origin is located in the intersection of photon beam and jet axis.

With regard to this Cartesian coordinate system the particles escaping from the interaction region have a spherical momentum distribution (momentum sphere) around the origin. Owing to this spherical geometry and its ring-like projection on the detector planes a second set of suitable coordinates is defined which considers the spherical geometry:

The two angles **θ** and **ϕ** are defined relative to the just defined z-axis as can be seen in Figure 4.2 where **ϕ** is used as azimuthal angle while **θ** denotes the polar angle. These two angles represent the emission angles of the particles from the interaction zone and play an important role during the detector calibration described later in this chapter.

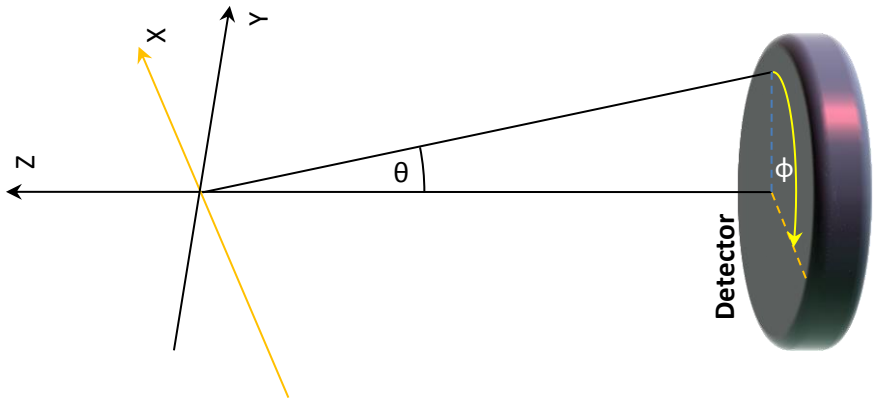

Figure 4.2: The angles θ and ϕ denote the emission direction of particles from the target zone.

4.2 Time-of-flight measurement

Measuring the time-of-flight of each charged particle is a key aspect of COLTRIMS. The flight-time through the well-defined acceleration field is a measure of the particle mass[1] and is indispensable for the calculation of the KER from the ion momenta.

Heavy particles have a higher inertia with respect to the constant Coulomb force which is reflected in their longer time-of-flight. The charged particles in this experiment have a wide range of different times-of-flight (TOF). Compared to the ions, the ICD and photoelectrons have much shorter TOFs resulting from their in the order of 10^4 times smaller mass. However, whereas each individual hit on the detectors provides a well-defined "stop signal" for the TOF measurement the "start- signal" though is not as clearly given. The bunchmarker signal which serves as timing reference has a period of 800 ns and is recorded over several periods for each hit on the detectors. Assuming the electron TOF (**eTOF**) to be much shorter than this lapse of time the assignment of each electron hit to a specific bunchmarker can be done by a modulo 800 operation on the raw electron TOF.

Even though, the bunchmarker signal is synchronized with the electron bunch it has a constant time offset to the light pulses reaching the experiment. The exact instant of interaction is therefore reconstructed from the electron TOFs by taking their gyration period into account which is also employed to calibrate the magnetic field:

Due to the Lorentz force induced by the magnetic field of the Helmholtz coils, electrons are forced onto spiral trajectories around the z-axis. The gyration period t_g is the time which electrons, starting in the interaction zone at $t = 0$, need to pass through a full cycle in the xy-plane. The gyration period and frequency are given by:

$$t_g = \frac{2 \cdot \pi \cdot m_e}{e \cdot B} \text{ and } \omega = \frac{t_g}{2 \cdot \pi} = \frac{m_e}{e \cdot B} \tag{4.1}$$

where B is the magnetic flux density (in Tesla) and $\frac{m_e}{e}$ is the electron mass-to-charge ratio.

[1] In this experiment all ions are singly charged so that their TOF depend only on their mass.

The right picture in Figure 4.3 shows the gyration period of electrons in this experiment. In this diagram the spatial position (x-coordinate) of each hit on a detector is plotted versus its time-of-flight.

For the spectrum shown in Figure 4.3 the electric field is varied over a wide range without altering the magnetic field. As a result, the electron TOF is also varied revealing several nodes along the time-of-flight axis which correspond to the moments when the electrons have passed through another full cycle in the xy-plane. The distance of the nodes on the time-of-flight axis is on average **57.1 ns**.

Taking the position of the first node into consideration the time offset of the electron TOF mentioned before can be reconstructed:

$$t_0 = t_{n1} - t_g = -\mathbf{7.1}\,\boldsymbol{ns} \tag{4.2}$$

The position of the first node on the TOF axis t_{n1} is at 50 ns. The TOF-offset of 7.1 ns has to be added to all raw eTOF values.

a) **b)**

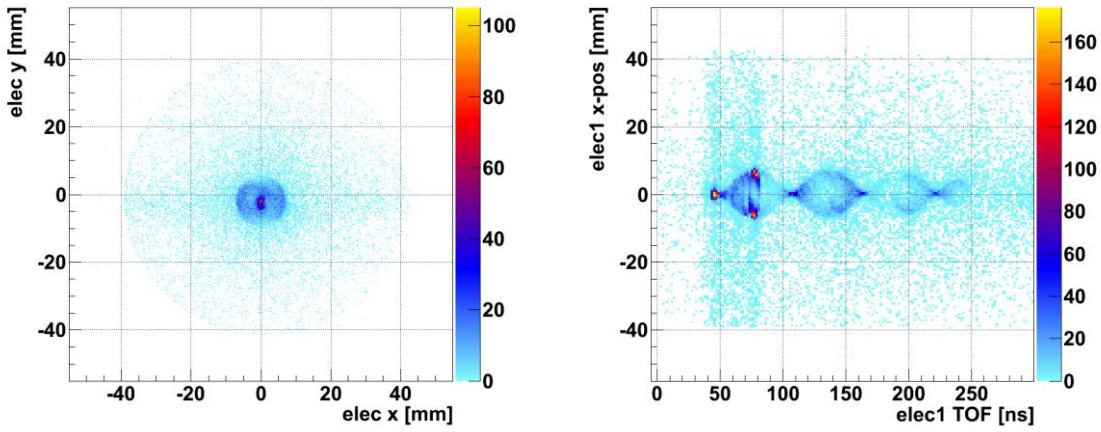

Figure 4.3: a) A detector raw image of the electron detector. Photoelectrons hit the detector on a ring shaped distribution. **b)** The x-coordinate of the electron hits plotted versus the electron time-of-flight. The distances between the nodes (57.1 ns) correspond to the gyration period of the electrons.

Compared to the eTOFs the ion times of flight (**rTOF**) are much longer. The ion TOFs in this experiment are in the order of several microseconds (Figure 4.4). Thus the ion TOF is also larger than the period of the bunchmarker signal. Assuming that the time difference between electron- and ion-TOF stays the same the ion TOF is reconstructed by adding the time difference between raw electron- and raw ion-TOF to the corrected electron times of flight.

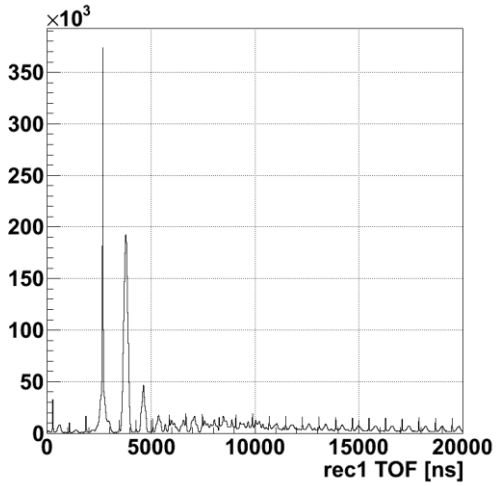

Ion	TOF
$\mathbf{He}^+$	2674 ns
$\mathbf{He_2}^+$	3782 ns
$\mathbf{He_3}^+$	4632 ns
$\mathbf{He_4}^+$	5348 ns
$\mathbf{He_5}^+$	5979 ns
$\mathbf{He_6}^+$	6550 ns
$\mathbf{He_7}^+$	7075 ns
$\mathbf{He_8}^+$	7563 ns
$\mathbf{He_9}^+$	8022 ns
$\mathbf{He_{10}}^+$	8456 ns
$\mathbf{He_{11}}^+$	8869 ns
$\mathbf{He_{12}}^+$	9263 ns

Figure 4.4: Ion time-of-flight spectrum recorded in setting IV. Ions with different masses are dispersed by their TOF. The peaks below 5 µs belong to He^+, He_2^+ and He_3^+.

4.2.1 The PIPICO diagram

The photoion-photoion-coincidence diagram (PIPICO diagram) is a simple but nevertheless very powerful tool to evaluate COLTRIMS datasets and identify physical processes by means of momentum and energy conservation. A PIPICO diagram contains time-of-flight information from pairs of ions detected in coincidence. For this purpose the TOF of one ion is plotted versus the TOF of the other ion. Physical processes such as ionization processes described in chapter 2.5.1 which generate pairs of ions can be identified by the characteristic traces they generate in PIPICO spectra. Figure 4.5 shows a PIPICO spectrum as observed for the ICD experiment on helium dimers in measurement **I** (cf. Table 3.2).

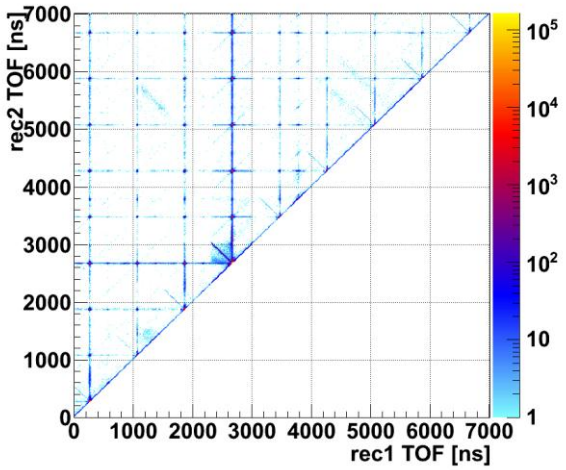

Figure 4.5: PIPICO spectrum for the ICD experiment on helium dimers recorded by applying setting **I** (Table 3.2).

Without any further restrictions all data points appearing in a PIPICO spectrum belong to paired ions which have been detected in coincidence within a short time window. The PIPICO spectrum presented in Figure 4.5 shows a series of continuous horizontal and vertical lines which can be assigned to uncorrelated ions in random coincidences.

Since a plenty of ions with no specific charge, TOF or masses are present inside and outside the spectrometer there is a certain probability for each hit on the ion detector to be incidentally registered together with other ions. In this way all possible time relations between the two ions are observed which is reflected in continuous horizontal and vertical lines emerging from accumulation points in the TOF- plane. Most of the structures in the PIPICO histogram shown in Figure 4.5 recur with lower intensities shifted by multiples of 800 ns on both TOF axes. These artifacts are produced if electrons and ions which have their origin in two different events (separated in time by multiples of the bunchmarker period) are incorrectly assigned to the same event.

Besides the straight structures some shorter diagonals with a negative slope (also called PIPICO lines) appear in the spectrum showing a clear correlation of the ion TOFs. These diagonals give evidence for real physical processes yielding ions which fulfill the momentum condition $\vec{p}_1 = -\vec{p}_2$ (cf. equation (2.30)). According to [8] the process which brings up the predominant PIPICO line in the present spectrum at about 2700 ns can be identified as the breakup of helium dimers into pairs of singly charged helium ions.

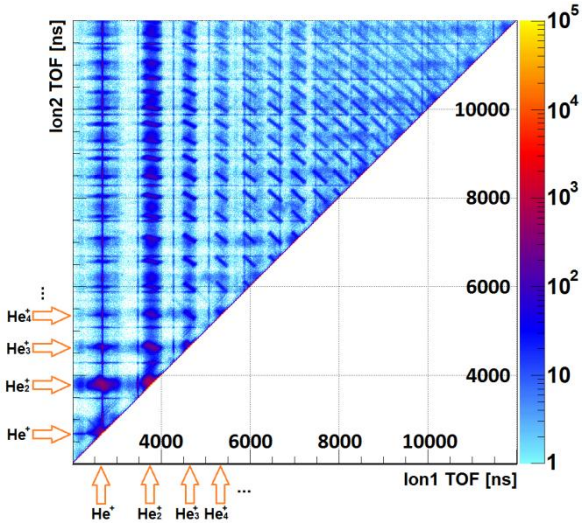

Figure 4.6: A PIPICO spectrum recorded with setting III. The short diagonal lines in the TOF-map indicate the existence of numerous breakup channels of large helium clusters (N~6500) after photoionization.

The PIPICO spectrum displayed in Figure 4.6 is taken with setting **III** and shows an abundance of PIPICO lines which indicate the existence of a variety of breakup channels for larger helium clusters into smaller fragments after photo double ionization. By looking at the PIPICO plane as quasi divided by rows and columns of short diagonals, each row can be attributed to a specific fragment size which is detected in coincidence with a second fragment of a size attributed to the respective column. Looking from the bisector of the plane to longer TOFs the size of the fragments increases by each column and from row to row. PIPICO lines which take their origin right at the bisector (just like the dimer line in Figure 4.5) can be assigned to symmetric breakups of clusters into equally sized fragments while lines which are found further away from the bisector go to the account of asymmetric fragmentations.

All datasets taken under settings **II-VI** show qualitatively the same PIPICO spectra. However, the structures seen in those datasets cannot be observed in the PIPICO spectra obtained from **VII-VIII**.

The PIPICO diagrams give a first insight to the COLTRIMS-datasets and form as well the basis of a more detailed data processing described in chapter 4.6.5.

4.3 Position measurement

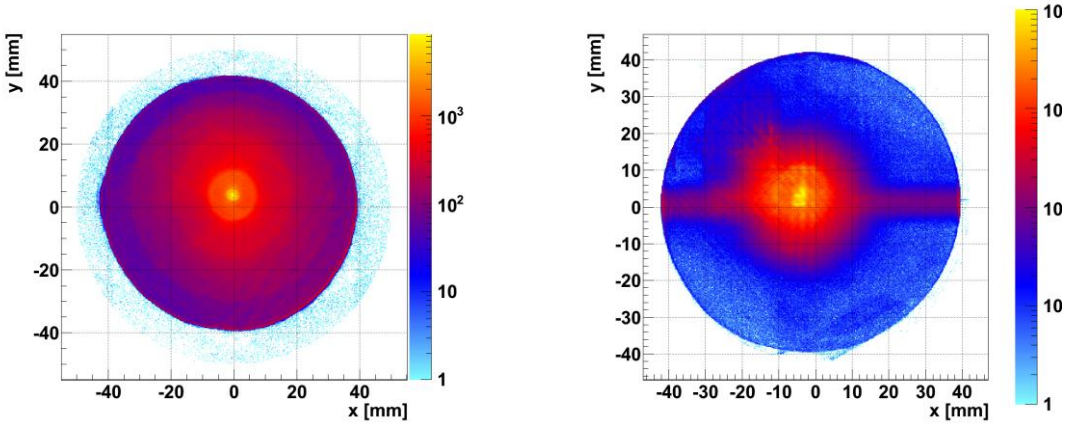

Figure 4.7: Detector raw-images of the electron detector (left) and of the ion detector (right). The center of the electron- and ion-hit distributions is not located in the origin of the xy-plane. The ion detector image shows a continuous horizontal stripe which is caused by the synchrotron beam when ionizing the residual gas in the experimental chamber.

The signals coming from the detector MCPs provide TOF data which give a first insight in the fragmentation of helium clusters. However, to understand the actual dynamics by reconstructing the fragment momenta, the hit position of each individual fragment on the detectors is required in addition.

The hit position on each layer (*u*-, *v*-, and *w*-layer) of the delay line anode is deduced from the propagation times to both ends by introducing conversion factors c_u, c_v, c_w converting time to length.

$$u = c_u(t_{u1} - t_{u2}) \tag{4.3}$$

$$v = c_v(t_{v1} - t_{v2}) \tag{4.4}$$

$$w = c_w(t_{v1} - t_{v2}) \tag{4.5}$$

The hit position in a Cartesian coordinate system can be easily expressed by a suitable linear combinations of u, v, w and two arbitrary offsets o_x and o_y , for instance by [44]:

$$x_{uv} = u + o_y \quad \text{and} \quad y_{uv} = \frac{1}{\sqrt{3}}(u - 2v) + o_y \tag{4.6}$$

4.4 Position and TOF correlation

The hit positions of electrons and ions on the detectors can be plotted versus the recorded time-of-flight for each hit as already done in Figure 4.3b.

Figure 4.8 shows the x- and y-coordinate of the ion hit positions in dependence of the measured time-of-flight for each ion. Singly ionized $\mathbf{He}_N^+$ cluster ions of fragment size N have a mass-dependent time-of-flight inside the spectrometer (as listed in Figure 4.4) and bring up different maxima in the histograms depicted in Figure 4.8. The predominant maximum at approx. 4 µs can be assigned to $\mathbf{He}_2^+$ ions. A series of maxima are visible in Figure 4.8b which show a time-dependent position offset along the y-axis. This time-dependent offset ("jet-offset") can be referred to the motion of the target clusters inside the supersonic gas jet. The helium clusters leave the cluster source with the same flow velocity ("jet-velocity") of $v_{jet} \approx 265\, m/s$ which is superposed on the velocity of the clusters gained in the spectrometer field after ionization. Larger cluster ions show a larger position offset due to their longer time-of-flight.

The periodic maxima visible in Figure 4.8b which show no jet-offset are caused by incorrect assignment of hits on the ion detector to specific events.

a) b)

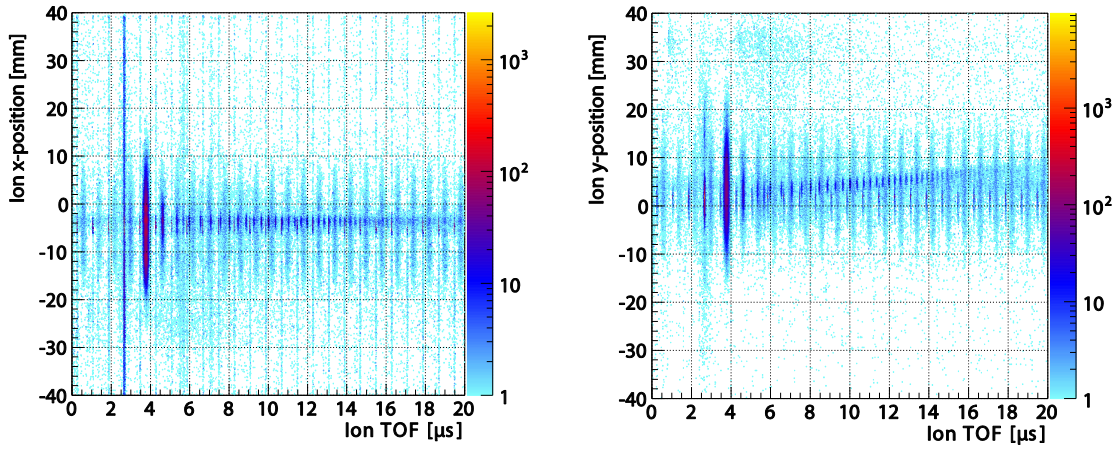

Figure 4.8: Spatial x-coordinate (a) and y-coordinate (b) of the hit positions on the ion detector plotted versus the measured time-of-flight. The spectra are obtained from photo single ionization of helium clusters with mean cluster size of N~6500 (measurement **III**) by using 25 eV synchrotron radiation. The time-dependent y-position offset of the hit maxima in (b) is caused by the supersonic motion of the clusters inside the gas jet.

4.5 Momenta and energies

The particle momenta have to be calculated from their time-of-flight together with their impact positions on the detectors. The electron and ion energies as well as the KER are thereon derived from the relative momenta before they are subject to further calibration.

4.5.1 Electron momenta

Based on the spectrometer geometry described in chapter 3.3.1 and with a magnetic field oriented in parallel to the electric field the equations of motion for electrons in this spectrometer field in x- and y-direction, dependent on their TOF t, can be expressed as:

$$x_e(t) = \frac{p_x}{m_e\omega}(\cos(\omega t) - 1) + \frac{p_y}{m_e\omega}\sin(\omega t) \tag{4.7}$$

$$y_e(t) = \frac{p_y}{m_e\omega}(1 - \cos(\omega t)) + \frac{p_x}{m_e\omega}\sin(\omega t) \tag{4.8}$$

where m_e is the electron mass and ω is the cyclotron frequency given in (4.1). The components $p_{x,y}$ of the particle momenta can be derived from (4.7) and (4.8):

$$\boldsymbol{p_x} = \frac{m_e(-\beta \cdot y_e - \gamma \cdot x_e)}{\beta^2 + \gamma^2} \tag{4.9}$$

$$\boldsymbol{p_y} = \frac{m_e(\gamma \cdot y_e - \beta \cdot x_e)}{\beta^2 + \gamma^2} \tag{4.10}$$

by using the following substitutions:

$$\beta = \frac{1 - \cos(\omega t_e)}{\omega} \quad , \quad \gamma = \frac{\sin(\omega t_e)}{\omega} \tag{4.11}$$

Different from the motion of the electrons in the xy-direction the motion in the TOF-direction along the z-axis is not influenced by the magnetic field but dominated by the electric field. Tough the field-free drift region located behind the electron acceleration region has to be taken into account for the calculation of the p_z-momenta.

Until reaching the drift region the motion of the electrons in the z-direction is constantly accelerated and the equation of motion is given by:

$$z_A(t) = \frac{1}{2}\frac{|\vec{E}| \cdot e}{m_e} \cdot t^2 + v_0 \cdot t^2 \tag{4.12}$$

where $|\vec{E}| = E$ quantifies the acceleration field in z-direction and v_0 the initial velocity parallel to $\vec{E}$. After the specific time t_A the electrons have traveled the corresponding distance z_A through the acceleration section and reach the drift region. While drifting through this section the motion of the electron is described by a new equation:

$$z(t) = z_A + z_D(t) = \frac{p_z}{m_e} \cdot t_A + \frac{1}{2}\frac{|\vec{E}| \cdot e \cdot (t_A^2 + t_D^2)}{p_z^2 + z_A \cdot |\vec{E}| \cdot e} \tag{4.13}$$

which can be solved analytically as explained in more detail in [45], [46] or [47]:

$$\boldsymbol{p_z} = m_e\left(-\frac{1}{3}s + \frac{c+d}{|c+d|} \cdot |c+d|^{\frac{1}{3}} + \frac{c-d}{|c-d|} \cdot |c+d|^{\frac{1}{3}}\right) \tag{4.14}$$

by using the following substitutions:

$$c = -\frac{u}{54} \qquad d = \sqrt{\frac{1}{4}\frac{1}{27}u^2 + \frac{1}{27}\left(\left(2\frac{e|\vec{E}|}{m_e}z_A - \frac{1}{3}s^2\right)^3\right)} \tag{4.15}$$

$$u = (2s^3 - \frac{e|\vec{E}|z_A}{m_e}18s + 27\left(\left(\frac{e|\vec{E}|}{m_e}\right)^2 z_A t_A - \frac{\frac{z_D^2}{2}e|\vec{E}|}{m_e t_A} - (z_A + z_D)2z_A\frac{e|\vec{E}|}{m_e t_A}\right) \tag{4.16}$$

$$s = \frac{1}{2}\frac{e|\vec{E}|}{m_e}t_A - \frac{z_A + z_D}{t_A} \tag{4.17}$$

4.5.2 Ion momenta

The magnetic field has only a negligible influence on the trajectories of the ions. In good approximation the equations of motion in the x- and y-direction are just TOF-dependent and can be expressed as:

$$x_r(t) = \frac{p_x}{m_r} t \tag{4.18}$$

$$y_r(t) = \frac{p_y}{m_r} t \tag{4.19}$$

In contrast to the calculation of the electron momenta the ion mass m_r is variable for each breakup channel and depends on the fragment size which also affects the time-of-flight of the fragments.

$$\boldsymbol{p_x} = \frac{m_r \cdot x_r}{t} \tag{4.20}$$

$$\boldsymbol{p_y} = \frac{m_r \cdot y_r}{t} \tag{4.21}$$

Just as for the electrons the time focusing geometry including a drift region in the ion arm has to be taken into consideration for the momenta in z-direction. The equation of motion is similar to the one for the electrons:

$$z_A(t) = \frac{1}{2} a \cdot t^2 + v_0 \cdot t^2 \tag{4.22}$$

where the acceleration vector $\vec{a}$ is parallel to the electric field and depends on the ion charge q.

$$\vec{a} = \frac{\vec{E} q}{m_r} \tag{4.23}$$

The ions pass through the full length of the acceleration region z_A until they reach the drift region at the time t_A with a new velocity v_A gained in the electrostatic potential:

$$t_A = -\frac{v_0}{a} \pm \sqrt{\frac{v_0^2 + 2 \cdot a \cdot z_A}{a^2}} \tag{4.24}$$

$$v_A = \sqrt{v_0^2 + 2 \cdot a \cdot z_A} \tag{4.25}$$

The drift time t_D through the field-free region is simply:

$$t_D = -\frac{z_D}{v_A} \tag{4.26}$$

The total ion time-of-flight t_{tot} in the Wiley McLaren geometry can be approximated for slow ions[1] which suffice the condition (4.28) as shown in [48] and [49]:

$$t_{tot} = t_A + t_D \approx -\frac{v_0}{a} + 2\sqrt{\frac{z_D}{a}} \tag{4.27}$$

$$v_0^2 \ll 2 \cdot a \cdot z_A \text{ and } \mathbf{E_0} \ll \left|\vec{E}\right| \cdot q \cdot z_A \tag{4.28}$$

For slow ions the momenta in z-direction can already be derived from (4.27):

$$\boldsymbol{p_z} = 2\sqrt{\left|\vec{E}\right| q m_r z_D} - \left|\vec{E}\right| q t_{tot} \tag{4.29}$$

[1]As not expected for the fragment energies in this work and atypical for Coulomb-exploding molecules

Due to the spectrometer geometry the time-of-flight distribution of the ionic fragments is symmetrical around the center time-of-flight of the ions with vanishing initial momenta $\boldsymbol{p_z} = 0$. Thus equation (4.29) can then be further reduced to [48]:

$$\boldsymbol{p_z} = |\vec{E}|q(t - t_{cor}) \tag{4.30}$$

by using the correction factor t_{cor} for the TOF of an n-sized ionic fragment (4.31)

$$t_{cor}(\mathbf{He_n^+}) = t_{\mathbf{He_1^+}} \cdot \sqrt{n} \tag{4.31}$$

The time-of-flight for the singly charged helium ion $t_{\mathbf{He_1^+}}$ can be experimentally determined.

However, if the fragment energies don't meet the conditions (4.28) for slow ions equation (4.27) has to be solved iteratively – for instance by applying Newton's method.

4.5.3 Relative momenta and KER

When looking at the fragmentation of helium dimers and clusters the momentum resolution can be significantly improved by exploiting momentum conservation of all fragments.

According to equation (2.30) the fragments from a Coulomb explosion carry complementary momenta. Therefore, the sum of the ion momenta can be set to zero and the relative momentum of the ions can be expressed in the center of mass system:

$$\vec{p}_1 = -\vec{p}_2 = \frac{\vec{p}_{rel}}{2} \tag{4.32}$$

The relative momenta are obtained therefrom as described in [47]:

$$\boldsymbol{p_{rel,x}} = \frac{m_{r1}m_{r2}(x_{r1} - x_{r2})}{m_{r1}t_{r2} + m_{r2}t_{r1}} \tag{4.33}$$

$$\boldsymbol{p_{rel,y}} = \frac{m_{r1}m_{r2}(y_1 - y_2) + v_{jet}(t_{r1} - t_{r2})}{m_{r1}t_{r2} + m_{r2}t_{r1}} \quad \text{with } v_{jet} = \sqrt{\frac{5}{2}\frac{kT}{m}} \tag{4.34}$$

$$\boldsymbol{p_{rel,z}} = \frac{E}{2}\left(\frac{t_{r2}^2 q_{r2} m_{r1} - t_{r1}^2 q_{r1} m_{r1}}{m_{r1}t_{r2} + m_{r2}t_{r1}}\right) \tag{4.35}$$

The kinetic energy release can be calculated from the relative momenta:

$$\boldsymbol{KER} = \frac{p_{rel}^2}{2\mu} \quad \text{with} \quad \mu = \frac{m_{r1}m_{r2}}{m_{r1} + m_{r2}} \tag{4.36}$$

The interaction zone has a finite spatial expansion in the xy-direction which is not compensated by the time-focusing geometry and leads to an uncertainty of the momentum reconstruction from the hit positions.

Different to the absolute momenta, the reconstruction of the relative momenta doesn't rely on absolute hit positions but rather on the position difference between two hits which per se doesn't depend on the starting points anymore.

On the other hand, the starting point of the ions can be reconstructed from their hit positions on the detector. Since ions and electrons originate from the same point in the interaction zone, this leads to a better momentum resolution on the electron side [8].

$$\boldsymbol{x_{start}} = \frac{t_{r2}m_{r1}x_{r1} + t_{r1}m_{r2}x_{r2}}{m_{r1}t_{r2} + m_{r2}t_{r1}} \quad \text{and} \quad \boldsymbol{y_{start}} = \frac{t_{r2}m_{r1}y_{r1} + t_{r1}m_{r2}y_{r2}}{m_{r1}t_{r2} + m_{r2}t_{r1}} \tag{4.37}$$

However, this approach assumes that there is no subsequent interaction of the fragment ions with other particles after the Coulomb explosion causing momentum transfer and energy dissipation. As will be shown later in this work this is not always the case for the fragmentation of large helium clusters. In this sense the single particle kinetic energies which are calculated from their absolute momenta play a decisive role:

$$\boldsymbol{E_{r,i}} = \frac{\left(p_{x,i} + p_{y,i} + p_{z,i}\right)^2}{2m_{r,i}} \tag{4.38}$$

4.6 Calibration and presorting

The identification of physical processes in the acquired data is substantially reliant on the accuracy of the reconstructed particle momenta and energies. Since the particle momenta are deduced from the position and TOF information under consideration of the spectrometer fields and spectrometer geometry a precise determination of the time zero and precise calibration of the detector images as well as of the spectrometer fields and spectrometer length are essential.

4.6.1 Photon energy calibration

The photon wavelength is selected by tilting the TGM grating of the beamline monochromator relative to the incoming photon beam. When entering values for the photon energy in the beamline control PC the monochromator is mechanically driven to predefined positions which correspond to the respective exit angle of the desired photon wavelength. The assignment of monochromator position and resulting photon energy leaving the beamline shows a systematic deviation which varies for different energy regimes of the beamline. To quantify this offset, the values for the photon energy are changed between 63.5 eV and 65.0 eV in steps of 200 meV considering the resolution of the beamline in this energy regime. When crossing the helium He^{+*}(n=2) excitation threshold, low energetic 1s-photoelectrons are emitted according to equation (2.24).

Slow photoelectrons with almost vanishing kinetic energy can be observed if the value for the photon energy at the beamline control is set higher than 63.75 eV. This leads to the conclusion that the beamline has an energy offset of about **1.65 eV**.

$$65.4\ eV^{1} - 63.75eV = \mathbf{1.65\ eV} \tag{4.39}$$

As discussed later on in section 5.1, it is conceivable that this calibration is not exact due to an energy shift of the ICD-threshold in large helium clusters.

[1] Helium single ionization and excitation threshold.

4.6.2 Calibration of the magnetic field

The electrons generated inside the spectrometer field perform a helical motion around the magnetic field axis. The gyration period of the electrons is of particular importance in two respects. Firstly the gyration period helps to find the time zero for the time-of-flight measurement as expressed further above in equation (4.2). Secondly the gyration period serves as an in situ measure of the magnetic field inside the spectrometer. The relation between magnetic field and electron cyclotron period is given by equation (4.1). The gyration period of the electrons can be deduced from the position of the nodes in the electron spectrum displayed in Figure 4.3. The averaged distance between the two nodes is 57.1 ns from which follows that the magnetic field inside the spectrometer amounts to **6.25 Gauss**.

In fact, the magnetic field calibration is subject to further fine tuning when it comes to the electron energy calibration. The next sections of chapter 4 provide the reader with more detailed information on how the electron and ion energy calibration is optimized by varying detector positions, spectrometer field, geometry, calibration of time zero offset and magnetic field.

4.6.3 Detector calibration

The detector calibration is the first and fundamental calibration to be done. Since the spatial detector images are obtained from the timing information of the delay line signals, the very first step is to obtain distortion-free spatial images of the hit positions on both detectors by choosing suitable delay-to-length conversion factors $c_{u,v,w}$. Doing this, the detector images are stretched and shifted in x- and y-direction until their visual appearance matches to the size of the used MCPs and until they are centered at the origin of the xy-plane.

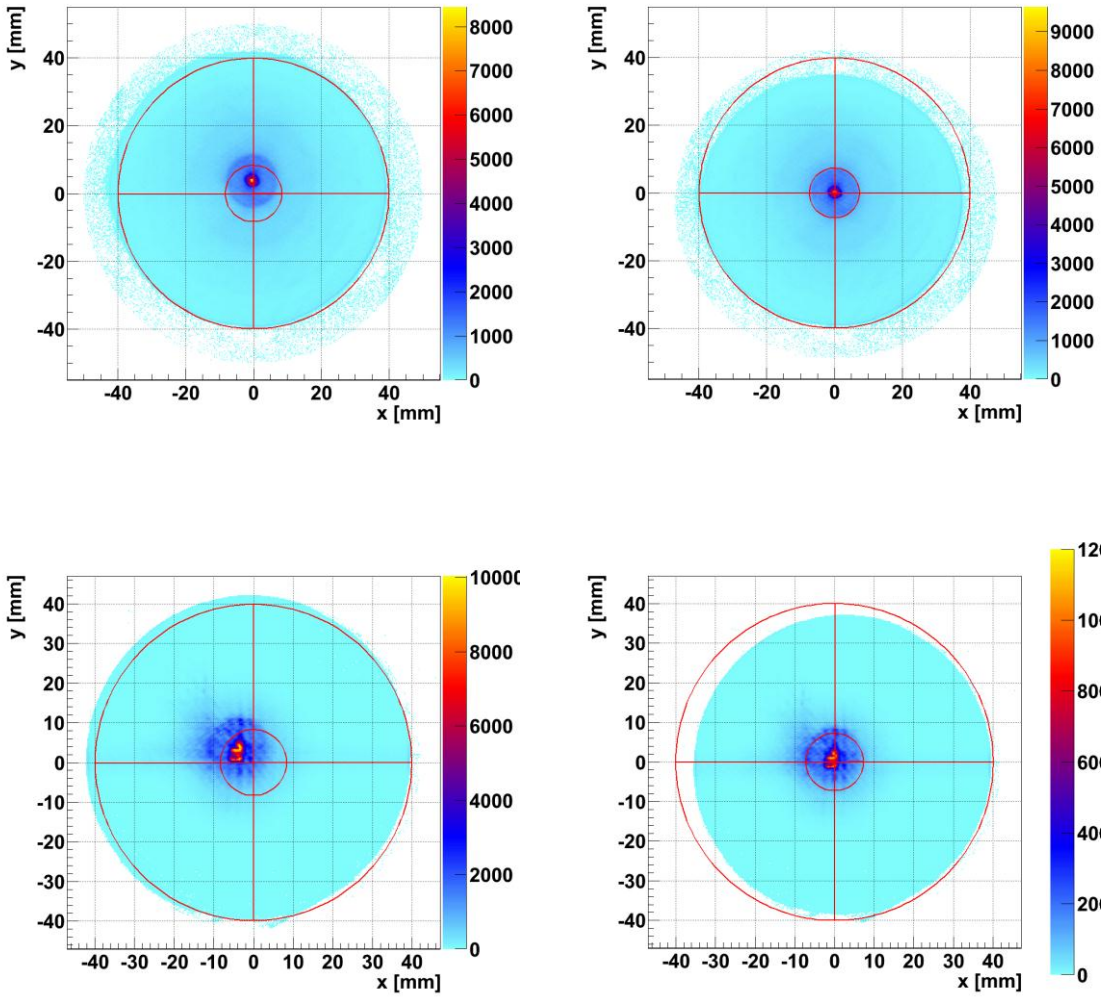

Figure 4.9: Stretching and repositioning of the electron detector image (upper row) and ion detector image (bottom row).

The center of the detector images and the xy-position of the interaction zone are not always congruent (Figure 4.9). Since, however, the electron and ion hit distribution on the detectors represent the projection of the respective momentum sphere spanned around the point of interaction, this incongruity leads to an incorrect momentum and energy reconstruction.

As the projection of the momentum sphere on all three spatial planes is circular, the detector images are shifted and stretched once again in x- and y-direction and by changing the TOF-offset also in z-direction until the projections of the momentum sphere on all spatial planes appear round and centered at the origin (Figure 4.10).

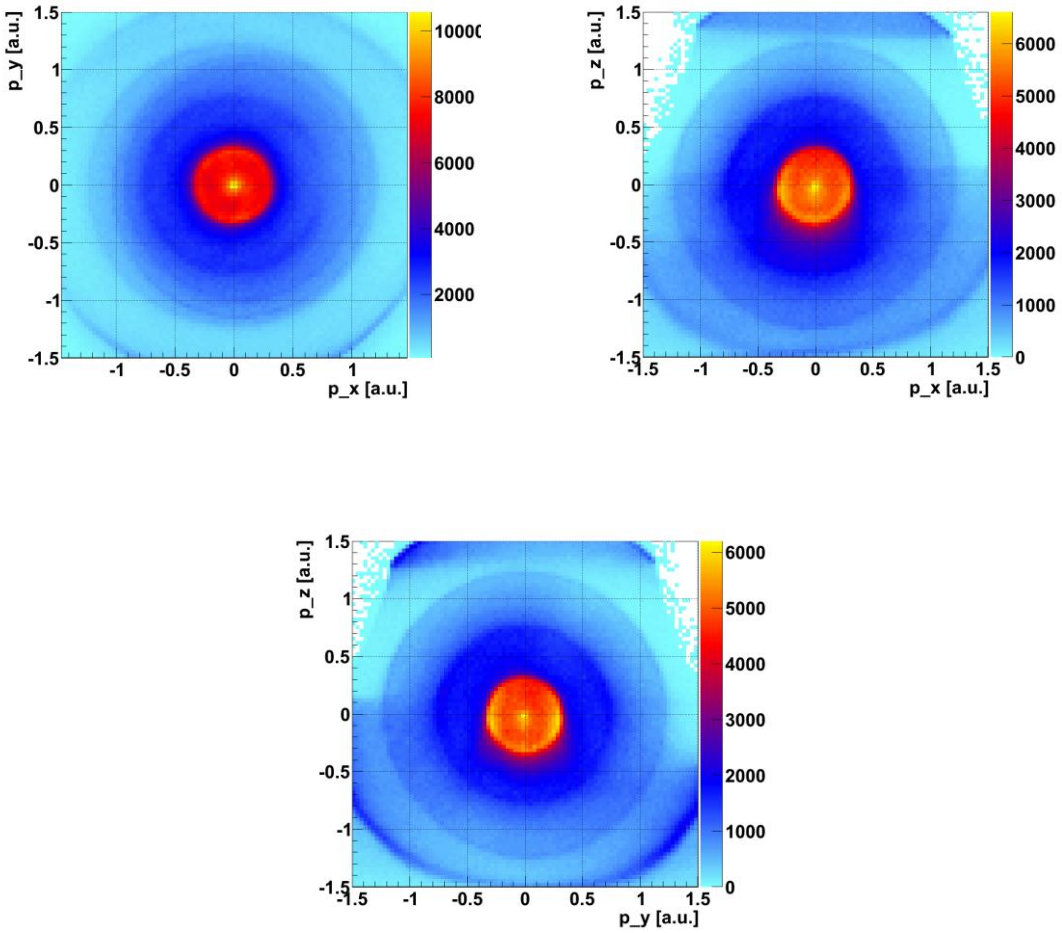

Figure 4.10: Projections of the electron momentum sphere on all three spatial planes. The inner circle can be assigned to the photoelectron while the middle circle corresponds to the ICD electrons.

Figure 4.10 shows the circular and centered projections of the electron momentum sphere on all three spatial planes. The nested circles correspond to an onionskin-like structure containing different shells which are spanned by electrons of different energies. The inner circle has a radius of 0.33 a.u. and can be assigned to 1s-photoelectrons with approximately 1.5 eV from the photoionization-excitation. The middle circle with a radius of 0.79 a.u. stems from comparatively fast ICD-electrons with kinetic energies of around 8 eV while the outer circle indicates the existence of fast electrons with a kinetic energy of about 20 eV. The outermost, cropped circle can be assigned to photoelectrons with about 43 eV from a 1s-photoionisation. The round and centered projections confirm that the electron momenta of all spatial dimensions are mapped correctly.

The projections on the xz- and yz-planes depicted in Figure 4.10 reveal that the electron z-momenta are significantly smeared out in negative z-direction most likely as a result of electron scattering on the spectrometer meshes. The tail-like structure is as well reflected in the reconstructed electron energy which can be clearer seen in the theta-representation of the electron energy spectrum. Therefore, the electron energy is plotted versus the emission angle **θ** in the lab frame (Figure 4.11a). The **θ**-angle is obtained from the z- and absolute momenta while **ϕ** is derived from the hit positions.

$$\boldsymbol{\theta} = arccos\left(\frac{p_z}{p}\right)\frac{180°}{\pi} \quad , \quad \boldsymbol{\phi} = arctan\left(\frac{p_x}{p_y}\right)\frac{180°}{\pi} \tag{4.40}$$

a) **b)**

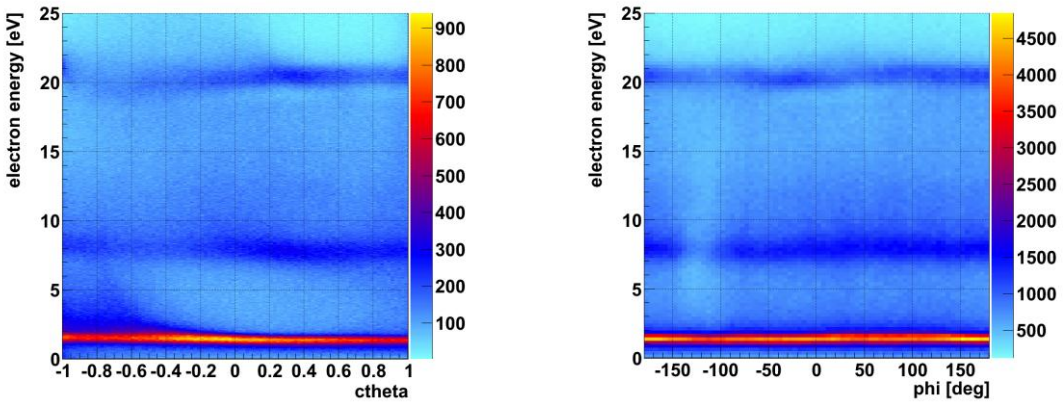

c)

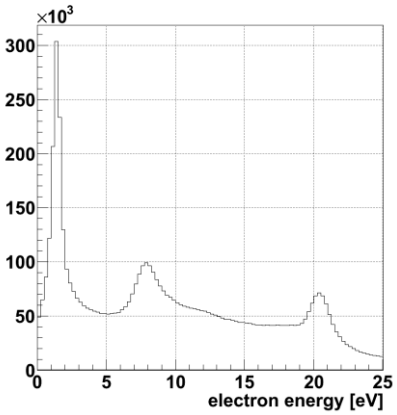

Figure 4.11: a) Electron energy spectrum in the **θ**-representation where **cos(θ)** is used instead of **θ** on the abscissa and **b)** The same spectrum in the **ϕ**-representation. **c)** One-dimensional electron energy spectrum.

When looking at the **ϕ**- and **θ**-representation of the electron energy spectrum the electron detector can be calibrated even more precisely. The reconstructed electron energies of an exactly calibrated detector are independent from the electron emission angles. In the **ϕ**- and **θ**-plots the horizontal lines corresponding to the electron energies are straight and show no major variation in their width. By using the **ϕ**-plot fine correction factors are found to shift and stretch the detector image while the **θ**-plot is used to find a suitable factor for the time-of-flight direction. However, the qualitatively correct energy reconstruction, respectively the correct energy position of the horizontal lines is subject to the spectrometer field calibration described in the next section.

The calibration is done for the ion detector as well. Different from the electrons the ions are detected pairwise so that the relative momenta of two coincident particles create a momentum distribution which can be used to calibrate the ion detector image in a quite similar way as by using the projected momentum sphere of the electrons.

Figure 4.12 shows the **ϕ**- and **θ**-KER distributions after detector calibration found for the helium dimer fragmentation after ICD while applying setting **I**. The KER distributions show no major variations in ϕ- and θ-direction which indicates that the ion detector image is exactly calibrated.

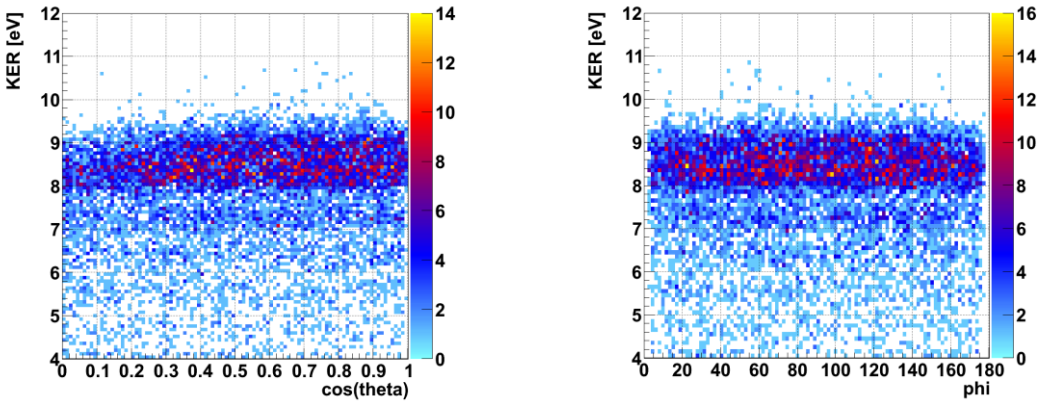

Figure 4.12: KER distributions for a helium dimer fragmentation in two singly charged helium ions. The reconstructed KER stays the same for different emission angles indicating a correct momentum reconstruction.

4.6.4 Energy calibration

The energy calibration is iteratively optimized by involving both, the detector calibration outlined in the previous section and the spectrometer calibration.

To obtain exactly reconstructed momenta the effective fields present inside the spectrometer as well as the exact spectrometer geometry have to be found.

Since the acceleration field is identical on both spectrometer arms in which it affects the trajectories of electrons and ions at the same time, the field strength has to be specified for the momentum reconstruction consistent primarily with both, the observed ion TOFs visualized in the PIPICO histogram and the observed electron z-momenta.

By varying the parameters for field and geometry, the momentum reconstruction is adapted to the observed TOFs for different fragments such as **He**$^+$, **He**$_3^+$ and **He**$_4^+$.

The field calibration indicates an electric field of 18.27 V/cm and a magnetic field of 6.25 Gauss. Deviations from the previously estimated fields (section 3.4) might be a result of magnetic shielding due to the permeability of the 316LN[1] -steel chamber [50].

Finally a correction factor of 0.94991 is applied to all ion momenta to stretch the KER for the dimer fragmentation (Figure 4.13) towards the correct energies according to previous works [5] [8].

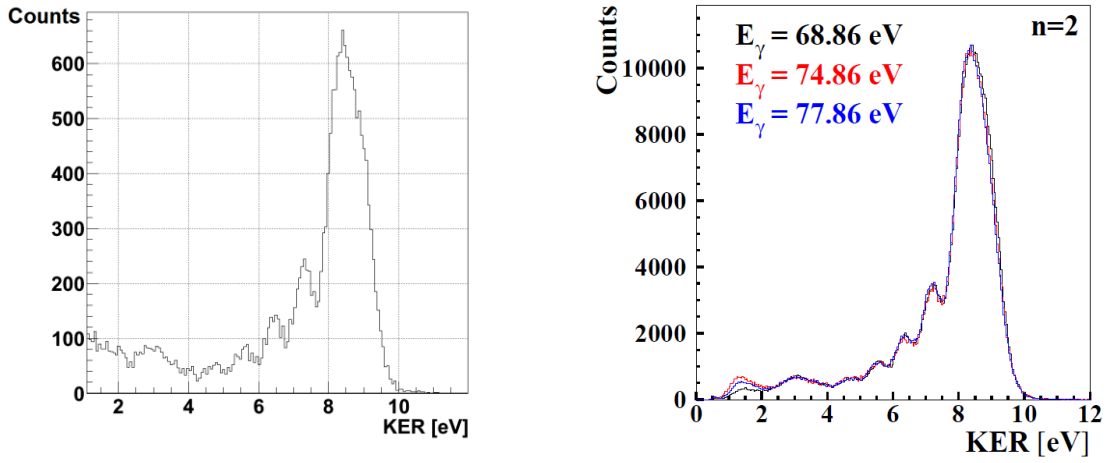

Figure 4.13: KER distribution found for the helium dimer fragmentation at 67.65 eV (setting I) in this experiment (left). The equivalent distribution taken from **[8]** (right). The maximum KER is found at 8.25 eV in both spectra indicating exact calibration.

[1] γ-phase iron alloy containing **Cr** (16%), **Ni** (10%) and **Mo** (2%). Relative permeability $\mu_r < 1.005$

The electron energy calibration is ascertained by taking advantage of the constant sum of ICD electron energy and kinetic energy release of a dimer breakup. In the event of a helium dimer fragmentation the total kinetic energy shared between the two ions after the Coulomb explosion and the ICD electron amounts to 16.22 eV. In an **energy correlation diagram** the kinetic energy of the collected electrons is plotted versus the calibrated KER. Events having their source in an ICD induced dimer breakup produce a high energetic electron and two ions which together fulfill energy conservation and appear on a diagonal line with negative slope. As already shown in Figure 2.11 this correlation has been observed in previous experiments and is now employed to ascertain the exact spectrometer calibration in the energy regime most relevant for this work.

The expected entanglement of KER and ICD electron energy is observed in measurement **I** and is in good agreement with previous experiments [8] as illustrated in Figure 4.14. The diagonal line spanned by KER and electron energy intercepts both x- and y-axis at a value of 16.22 eV which corresponds to the conserved total energy.

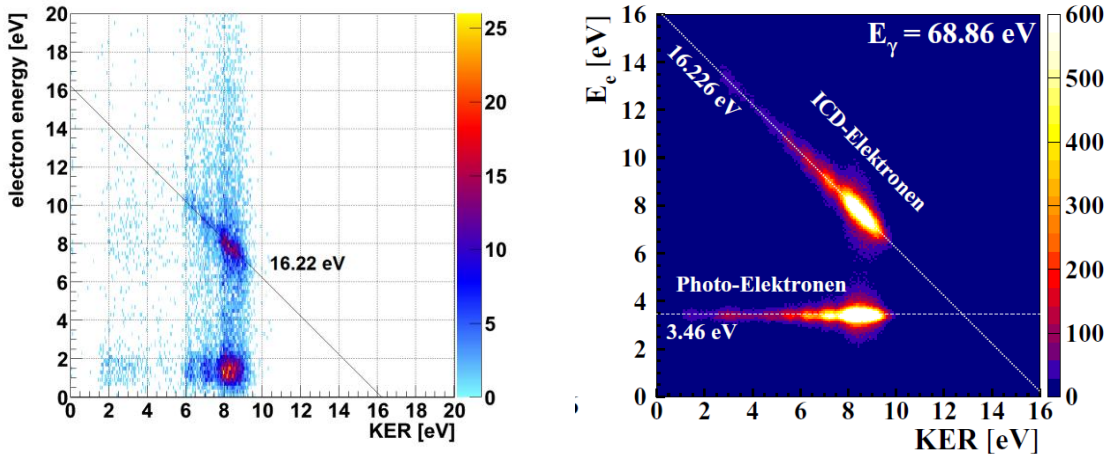

Figure 4.14: Energy correlation diagram of KER and electron energy obtained from dimer breakups in measurement **I** (left). The same energy correlation has been found in **[8]** (right).

4.6.5 PIPICO presorting

As introduced in section 4.2.1 the PIPICO diagram explicitly shows different fragmentation channels of large helium clusters. Since all ionic fragments in this experiment are singly charged their TOFs are directly mass dependent. The momentum

relation between two ions emerging from the same fragmentation causes a relation between their TOFs leading to short diagonal lines in this coincidence diagram. The center of each diagonal is located at a specific center time-of-flight which scales for different fragment sizes with a mass dependent factor as shown in equation (4.31).

The PIPICO histogram depicted in Figure 4.15 is taken from the fragmentation of N~6500 clusters and shows several PIPICO lines which each can be assigned to fragmentations into pairs of specific sized fragments as already done in Figure 4.6.

Based on the processed data the subsequent analysis is carried out for each fragmentation channel separately. By applying conditions on the collected ions which require a strict relation between their TOFs together with specific TOF windows only such events are selected from the calibrated data which belong to specific breakup channels. This implies an isolation of different "islands" in the PIPICO and the assignment of events to defined breakup channels as illustrated in Figure 4.15.

By doing this events from the calibrated dataset are sorted by distinct breakup channels starting from the $\mathbf{He^+ - He^+}$ fragmentation channel up to the $\mathbf{He_{10}^+ - He_{10}^+}$ channel including also asymmetric breakups for instance the $\mathbf{He_3^+ - He_4^+}$ fragmentation channel as done in Figure 4.15.

A new presorted dataset including only events from these channels is written to a new root file which forms the basis of the following data analysis.

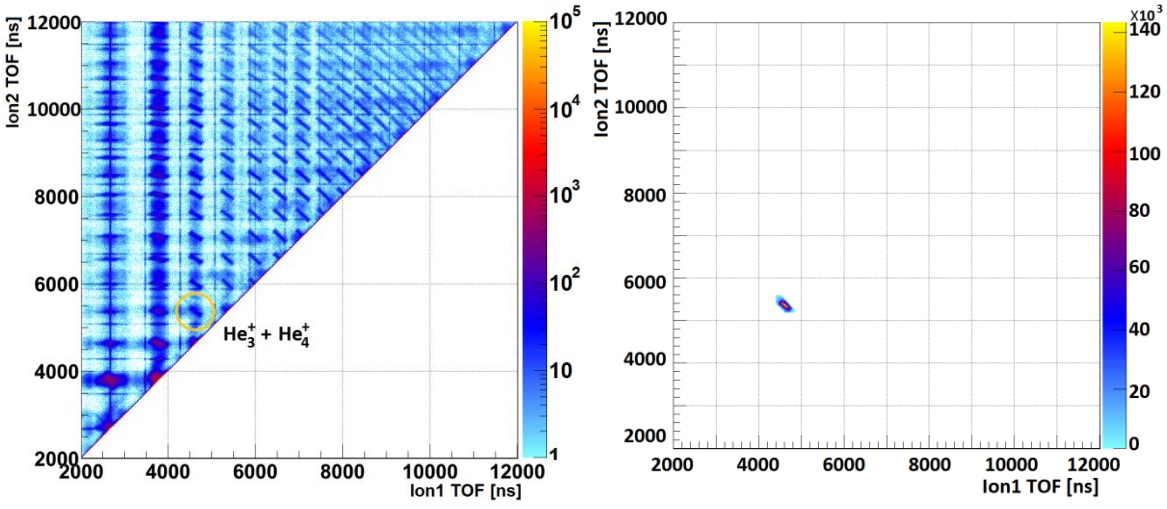

Figure 4.15: PIPICO of the raw dataset III (left). PIPICO of the same but presorted dataset (right). The dataset contains only events from the $\mathbf{He_3^+ - He_4^+}$ fragmentation channel

Chapter 5

Results

This work investigates the fragmentation process of large helium clusters after ICD. A series of datasets has been obtained from the ionization of various cluster targets by applying settings **I-VIII** to the cluster source (as listed in Table 3.2).

As described in the preceding chapter, the datasets have been presorted into distinct fragmentation channels, have been processed to suppress background and prepared for further analysis.

Chapter five presents the results of this analysis and discusses potential processes which have led to these results. At first the electron energy spectra for different fragmentation channels are presented where the detected ICD electron and photoelectron can be identified. Thereupon the numerous fragmentation channels are characterized and the cluster size distributions of the gas targets are determined which show a substantial discrepancy between estimated cluster size and the size distribution measured by using time-of-flight mass spectroscopy of singly ionized clusters.

Finally the kinetic energy release in a selection of different fragmentation channels is presented. Furthermore, the ion ion-energy correlation as well as the KER electron energy correlation is examined for distinct fragmentation channels which reveal a considerable interaction of electrons and ion fragments with the neutral cluster. It is shown that this interaction leads to a massive dissipation of the released kinetic energy.

5.1 Electron energy spectra

A raw electron energy spectrum from all collected electrons, regardless of specific fragmentation channels of dataset **IV** (N~15000), taken at 67.65 eV photon energy has been presented earlier in Figure 4.11. In this section spectra of electrons collected in various breakup channels of datasets I to IV are discussed. All presented spectra show two predominant maxima. The first, low energy peak at **1.5 eV** is caused by 1s-photoelectrons from the helium single ionization-excitation as described in (2.27).
If simultaneous ionization and excitation takes place, the provided photon energy is used for the $1s \rightarrow 2p$ transition and to ionize the other helium 1s-electron. The photoelectron gains as much kinetic energy as available after subtracting those energy portions from the photon energy:

$$E_{e^-} = E_\gamma - E_{ion}(\mathbf{He}) - E_{\mathbf{He}^+}(n=2) = \mathbf{2.3\ eV} \qquad (5.1)$$

However, with the assumed photon energy of 67.65 eV, the photoelectron peak is found **0.8 eV** below the expected energy. Comparisons with [5] suggest that these low energetic electrons stem from the helium 1s-photoionization. It is unclear if this massive deviation can be traced back to imprecise photon energy calibration of the beamline or to energy dissipative processes in the superfluid helium droplets such as excitation of phonons or other effects which lead to a considerable energy loss of photoelectrons as also reported in [51]. The fact that the photoelectrons in the dimer fragmentation measurement **I** are found at the same energy and, at the same time, the ICD electrons are observed at the correct energy leads to the conclusion, that the beamline offset has not been exactly calibrated because a gas target with a high content of large clusters was used. Experiments done in [13] indicate a significantly lowered helium single ionization threshold in large clusters. The authors observed helium single photoionization in large helium droplets (N~8000) already at photon energies between **23 eV** and **24 eV**. This implies a substantially lowered ICD threshold of:

$$\mathbf{63.81\ eV} \leq E_{ICD} = E_{ion}(\mathbf{He}) + E_{\mathbf{He}^{+*}}(n=2) \leq \mathbf{64.81\ eV} \qquad (5.2)$$

Indeed, the beamline photon energy offset calibration depicted in section 4.6.1 has been performed by employing the ICD-threshold as a reference while using a gas target with a high content of large helium clusters (setting **II**, N~5000). The actual amount of large clusters ($8000 \leq N \leq 100000$) in the target can be estimated with equation (2.6) and is in the order of 14% (Figure 5.7). The amount of small clusters (N<100) in the target can be estimated in the same way and is in the order of 10^{-9}. Thus, the helium single ionization-excitation could already have set in at about 0.6 eV lower energies than expected.

The zero-kinetic-energy photoelectrons were observed, as the photon energy was set to 63.75 eV. At this point the photon energy has already reached the ICD threshold in large helium clusters. The ICD threshold in large helium clusters is expected to be at approx. $(64.31 \pm 0.5)\ eV$ (cf. equation (5.2)) due to the lower single ionization threshold according to [13]. Correspondingly, the beamline offset of the TGM-7 beamline is significantly smaller than assumed:

$$(64.31 \pm 0.5)\ eV - 63.75\ eV = (\mathbf{0.56 \pm 0.5})\ \boldsymbol{eV} \qquad (5.3)$$

Taking this into consideration, the photon energy which was believed to be as high as 67.65 eV as stated before is now estimated to be at (67.1 ± 0.5) eV. The photoelectron peak at 1.5 eV can therefore be explained by the lower photon energy and is consistent with the fact that the ICD-electron peak is found at the correct energy:

$$E_{e^-} = E_\gamma - E_{ion}(\mathbf{He}) - E_{\mathbf{He}^{+*}}(n=2) = \mathbf{1.6\ eV} \qquad (5.4)$$

The second maximum in the electron energy spectra is found at 7.86 eV, which can be assigned to ICD electrons. This comparatively broad peak appears in the spectra as soon as the photon energy is set above the ICD threshold whereas it is not visible below the threshold (for instance at 25 eV photon energy). The energy of the ICD electrons found in this experiment is in good agreement with previous measurements [5] [8]. Moreover, a clear correlation between KER and ICD electron energy can be observed (Figure 5.16) and is discussed later in this chapter.

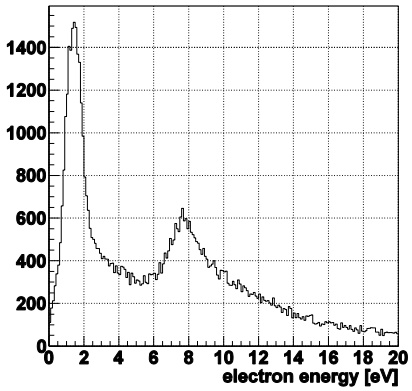

$\mathbf{He^+ - He^+}$

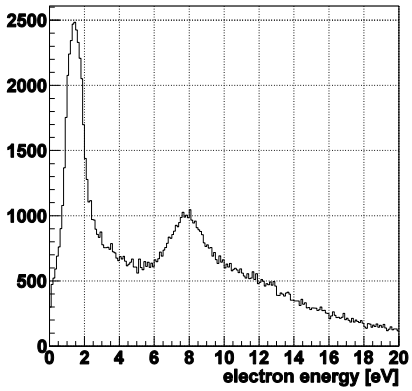

$\mathbf{He^+ - He_2^+}$

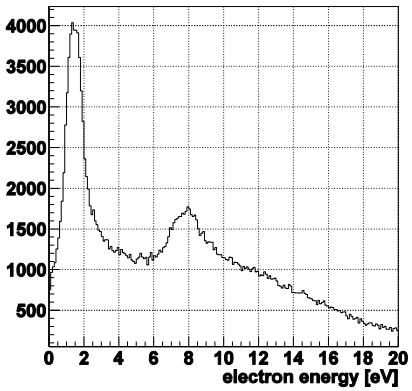

$\mathbf{He_2^+ - He_2^+}$

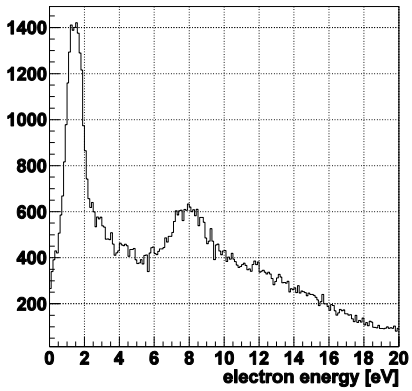

$\mathbf{He_2^+ - He_3^+}$

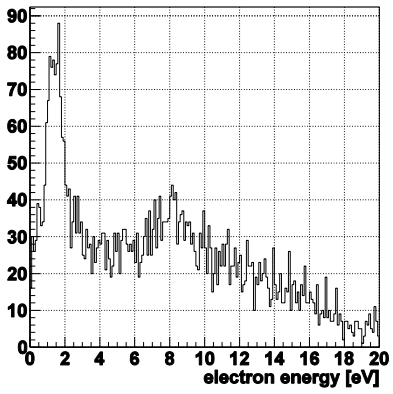

$\mathbf{He_6^+ - He_7^+}$

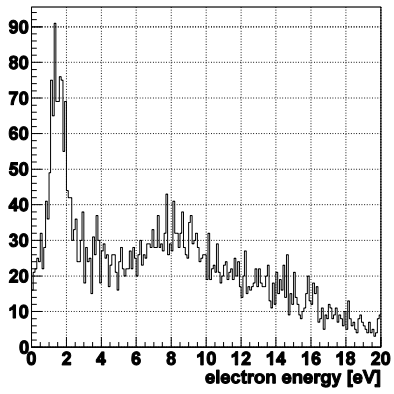

$\mathbf{He_6^+ - He_8^+}$

Figure 5.1: Electron spectra from different breakup channels. Mean cluster size: **N~5000**

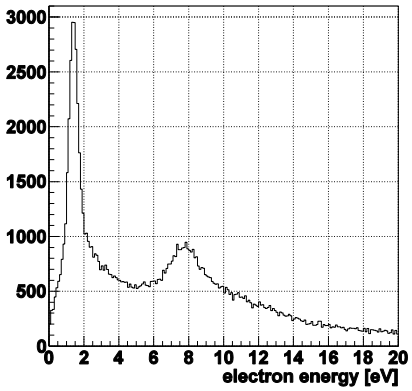

$\mathbf{He^+ - He^+}$

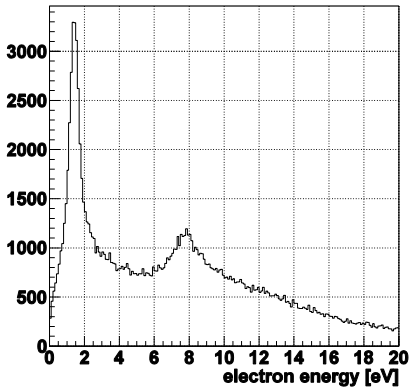

$\mathbf{He^+ - He_2^+}$

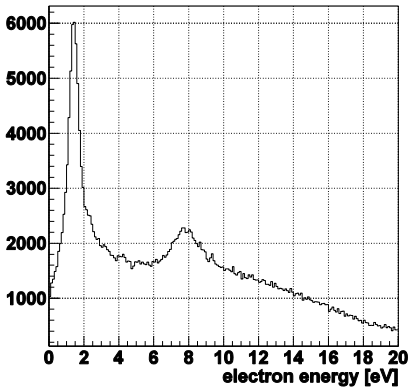

$\mathbf{He_2^+ - He_2^+}$

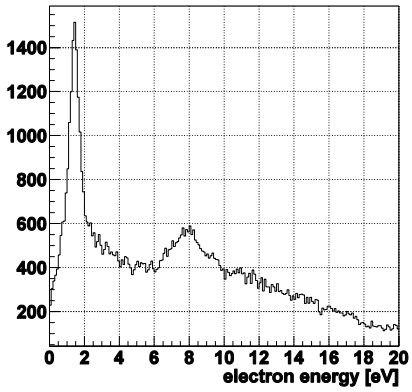

$\mathbf{He_2^+ - He_3^+}$

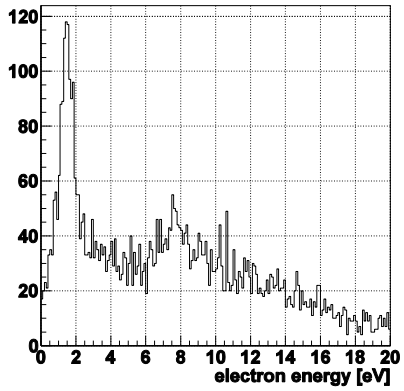

$\mathbf{He_6^+ - He_7^+}$

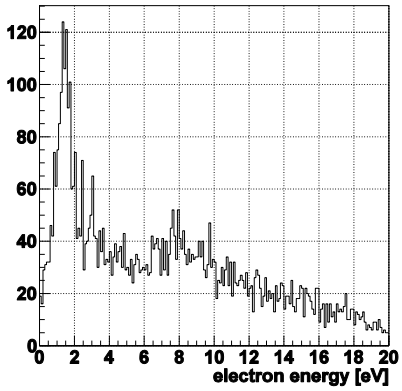

$\mathbf{He_6^+ - He_8^+}$

Figure 5.2: Electron spectra from different breakup channels. Mean cluster size: **N~15000**

5.2 Breakup channels

The PIPICO spectra presented in Figure 4.6 and Figure 4.15 already indicate a decomposition of large helium droplets (N~6500) into comparatively small fragments (N<20) after internal formation of ion pairs. Considering the short islands in the PIPICO diagram as traces of the breakup channels, no fragmentation channels beyond the $\mathbf{He_{20}^+ - He_{20}^+}$ channel can be separated from the background. Even if the background in the PIPICO spectra is suppressed by setting an energy condition (energy gate) which requires a coincident detection of a high energetic ICD electron of an energy of (7.86±0.61) eV, no channels of higher order are disclosed (Figure 5.5). These findings also agree with semi-classical simulations done by N. Sisourat [36] (Figure 2.12). The distribution of breakup channels is found to be surprisingly invariant under alteration of the mean cluster size. As illustrated in Figure 5.3, the channel distribution remains qualitatively[1] unchanged if the mean cluster size is increased from N~5000 to N~30000. For instance, the ratio between coincident fragment pairs and surrounding background caused by random coincidences is shown in Figure 5.4 for the $\mathbf{He_3^+ - He_N^+}$ channels. For mean cluster sizes of N~5000-6500 the number of events in the asymmetric channels declines almost linearly from the $\mathbf{He_3^+ - He_4^+}$ channel to the $\mathbf{He_3^+ - He_{20}^+}$ channel, while the PIPICO diagonals remain clearly defined. The prevalence of breakup channels drops faster for mean cluster sizes of N~15000-30000 where channels below the $\mathbf{He_3^+ - He_{15}^+}$ channel are still clearly delimited. The drop is even more dramatic if the mean target cluster size reaches values above N~200000 atoms. Channels beyond the $\mathbf{He_3^+ - He_7^+}$ channel can't be separated from the background anymore.

The time-of-flight mass spectrometry of the gas target by using photo single ionization at 25 eV (right above the helium single ionization threshold) (Figure 5.6) clearly indicates the separation of small fragments such as $\mathbf{He_2^+}$ and $\mathbf{He_3^+}$ from large helium clusters, even if the photoionization does not produce high energetic cluster fragments. This fragmentation dynamics is qualitatively in good agreement with the time-of-flight mass spectrometry done in [13] at a photon energy of 24.75 eV.

[1] Apart from slight dissimilarities arising from differently sized databases.

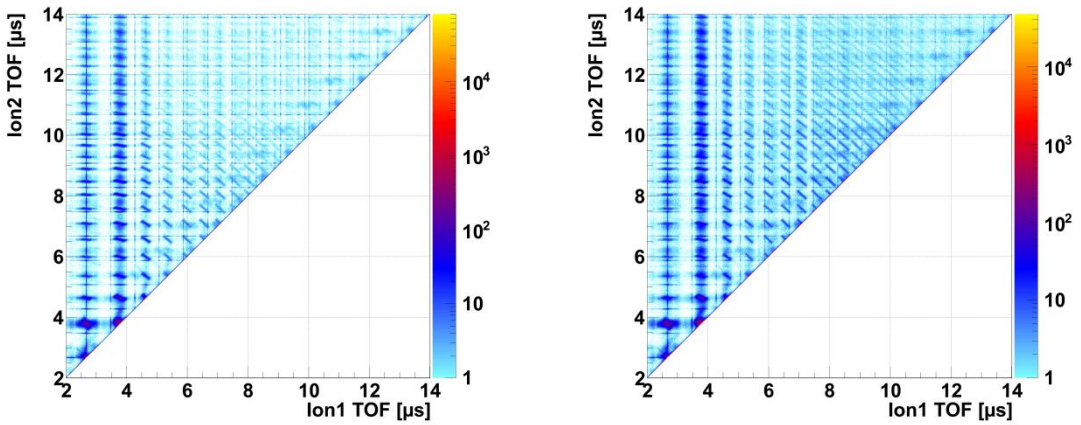

N~5000

N~6500

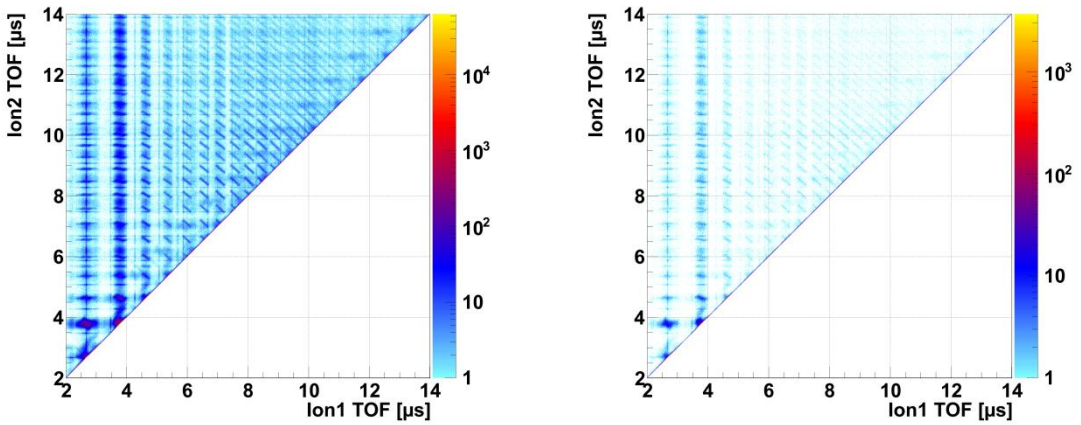

N~15000

N~30000

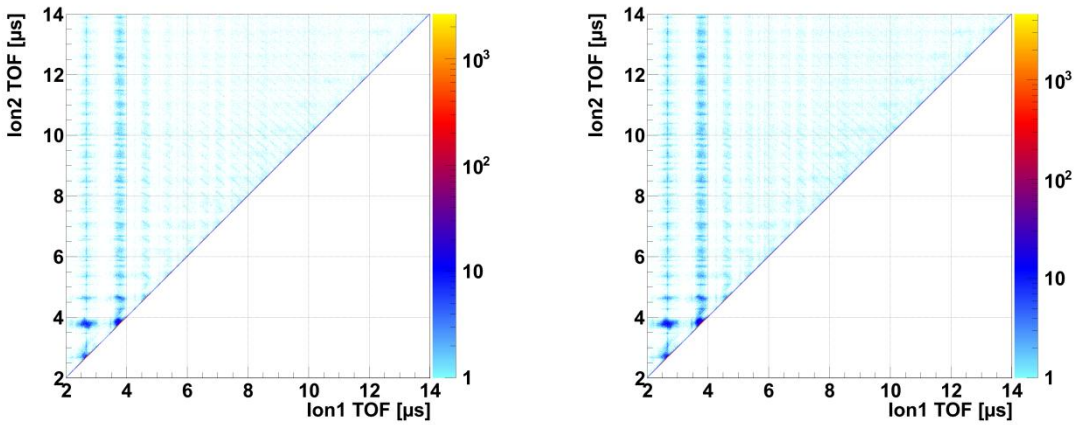

N~200000

N>200000

Figure 5.3: Raw PIPICO histograms obtained for different source conditions (**II-VII**).

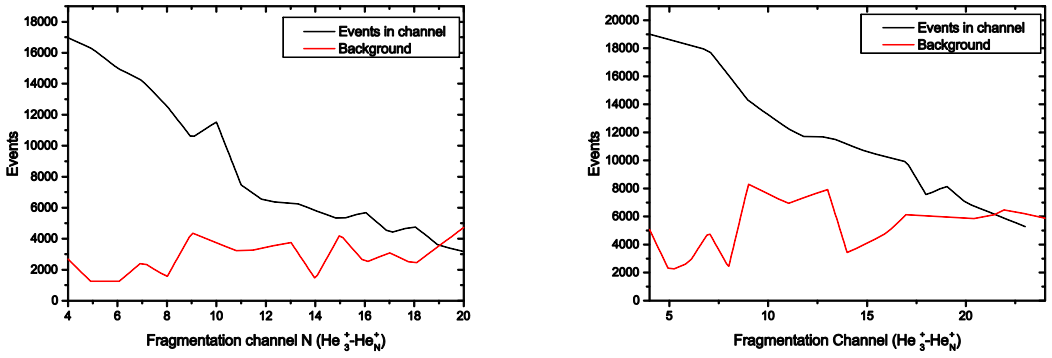

N~5000

N~6500

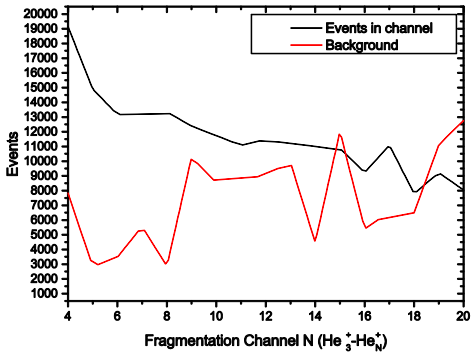

N~15000

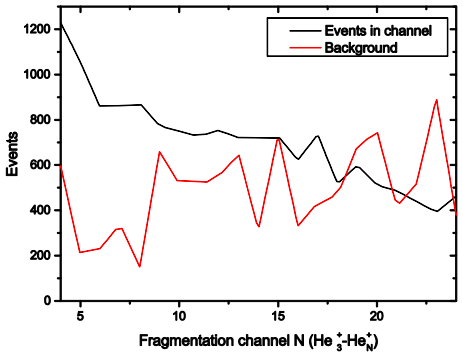

N~30000

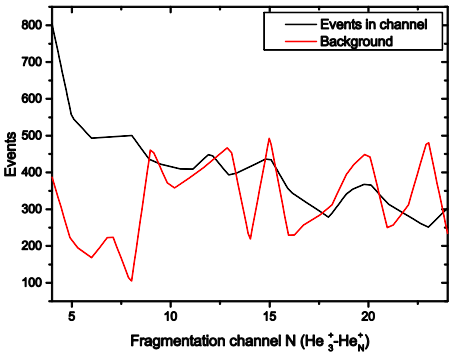

N~200000

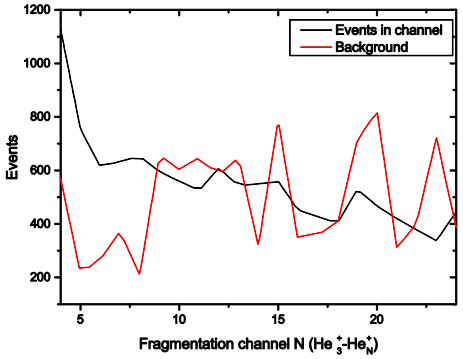

N>200000

Figure 5.4: Events in the $\mathbf{He_3^+ - He_N^+}$ breakup channels for different mean cluster sizes. Breakup channels below the $\mathbf{He_3^+ - He_{19}^+}$ channel are clearly separable from the background while breakup channels of higher order cannot be separated from the background anymore.

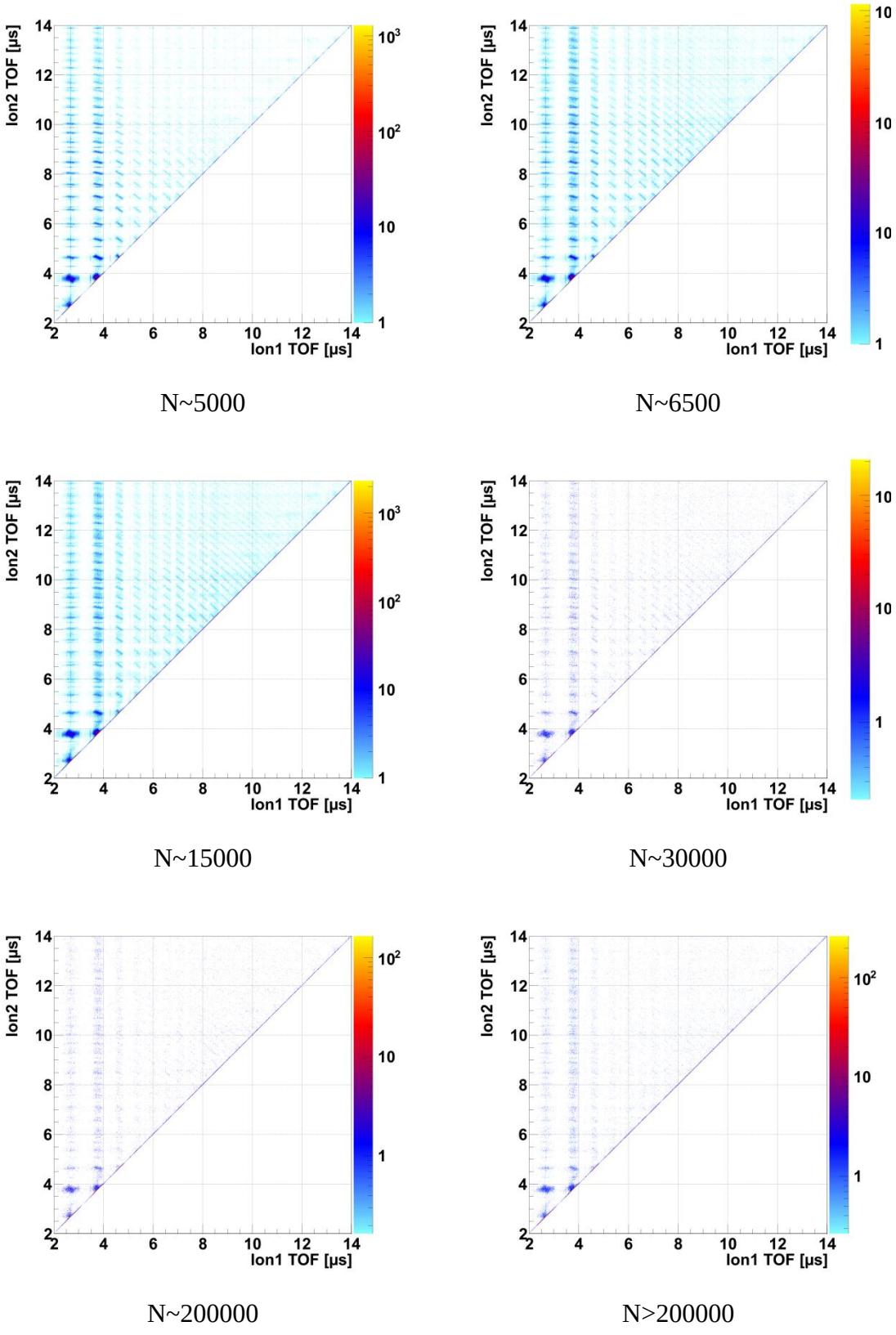

Figure 5.5: Spectra, shown in Figure 5.3 with a gate requiring 8 eV ICD electrons.

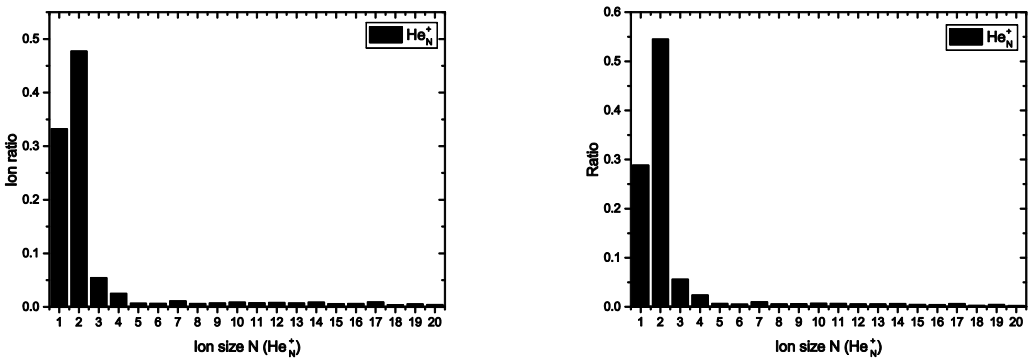

N~6500 N~15000

Figure 5.6: Mass spectra generated from time-of-flight measurements of singly ionized helium clusters by using 25 eV synchrotron radiation. The mean cluster size in the gas-target was set to N~6500 (left) and N~15000 (right). The spectra give clear evidence for a breakup of large clusters into helium monomers, dimers, trimers and tetramers.

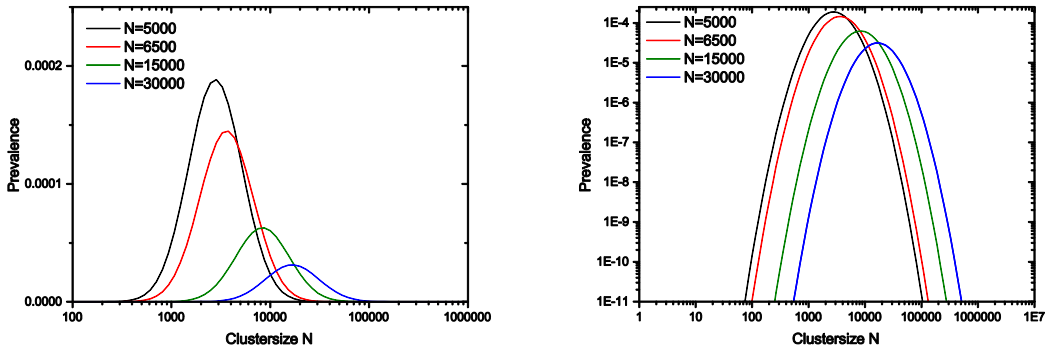

Figure 5.7: Calculated log-normal size distribution (2.6) of helium cluster sizes in the gas target for given mean cluster sizes N~5000 to N~30000 for the different source conditions as listed in Table 3.2.

5.3 Kinetic Energy Release

In the following section ion energy spectra and the kinetic energy release (KER) of the cluster fragmentation is presented for different cluster sizes. The kinetic energy release in different fragmentation channels is reconstructed by using the relative momenta of the detected ions according to equation (4.36). To further reduce the background in the presorted datasets, events with relative momenta below 5 a.u. and above 50 a.u. are discarded (Figure 5.8). This is reflected in an energy cut-off in the KER-spectra below 0.1 eV and above 10 eV.

Independent from the mean cluster sizes present in the gas target, the KER shows a significant decrease for increasing fragment size. In case of N~5000 cluster fragmentations (Figure 5.9), the $\mathbf{He^+ - He^+}$ breakup channel shows a KER maximum at 1.08 eV whereas the kinetic energy release in the $\mathbf{He^+ - He_2^+}$ channel has almost halved to only 0.58 eV. The KER drops further for breakup channels of higher order. The drop depends mostly on the size of the largest fragment in the respective breakup channel (Figure 5.11). As can be seen in Figure 5.10 the KER shows the same behavior for larger clusters N~15000.

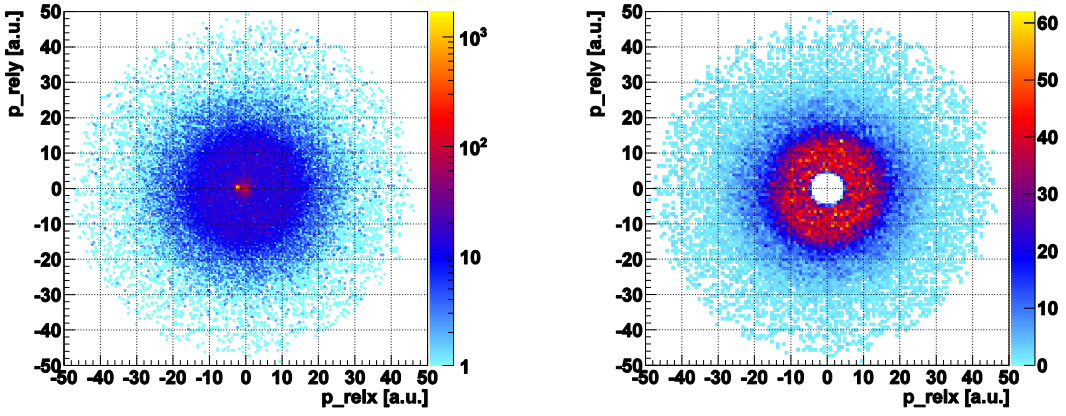

Figure 5.8: Relative momenta of the $\mathbf{He^+ - He^+}$ breakup channel. Events with relative momenta below 5 a.u. (KER < 0.1 eV) are discarded.

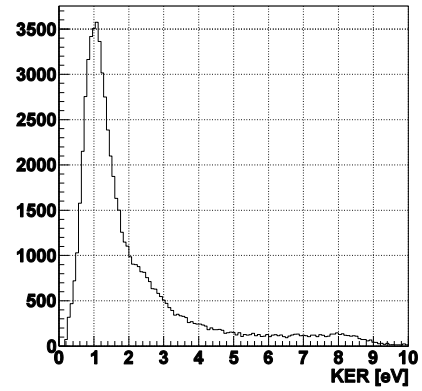

$\mathbf{He^+ - He^+}$

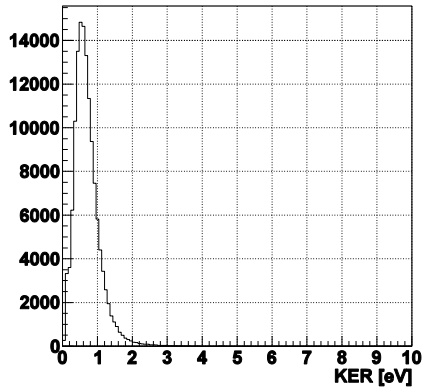

$\mathbf{He^+ - He_2^+}$

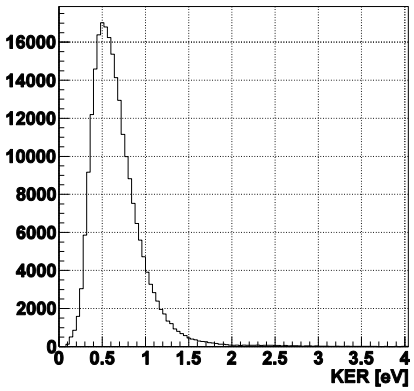

$\mathbf{He_2^+ - He_2^+}$

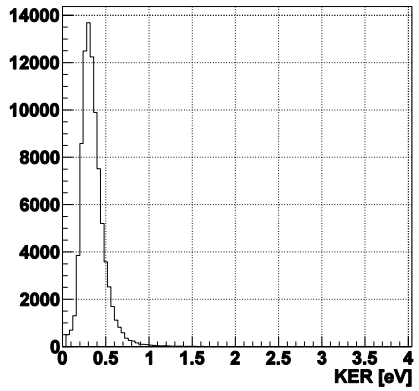

$\mathbf{He_2^+ - He_3^+}$

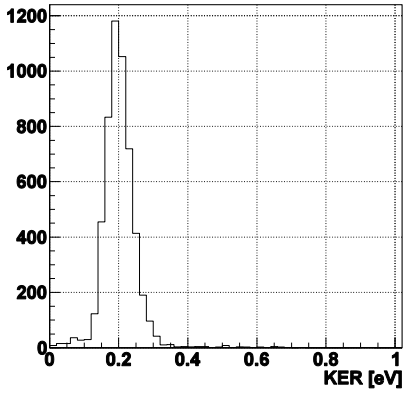

$\mathbf{He_6^+ - He_7^+}$

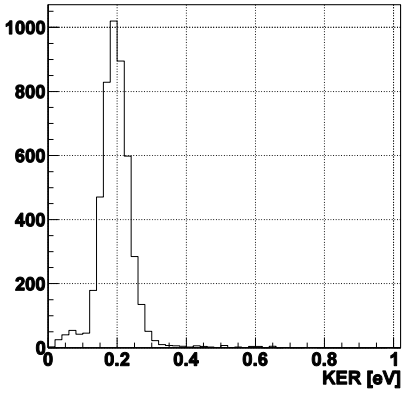

$\mathbf{He_6^+ - He_8^+}$

Figure 5.9: KER spectra for breakups of N~5000 clusters. The KER decreases for larger fragments. The $\mathbf{He^+ - He^+}$ channel contains events with higher KER (>2 eV).

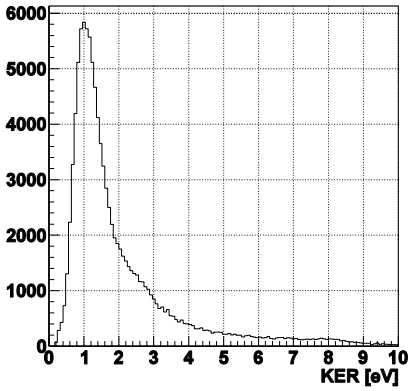

$He^+ - He^+$

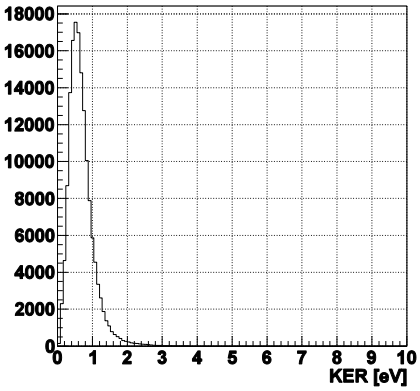

$\mathbf{He^+ - He_2^+}$

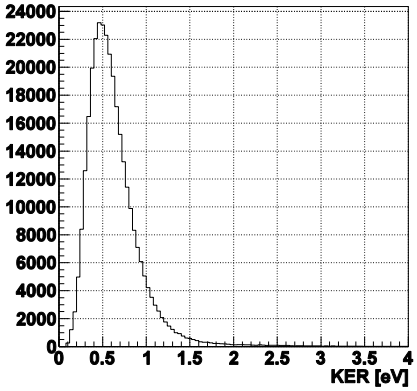

$\mathbf{He_2^+ - He_2^+}$

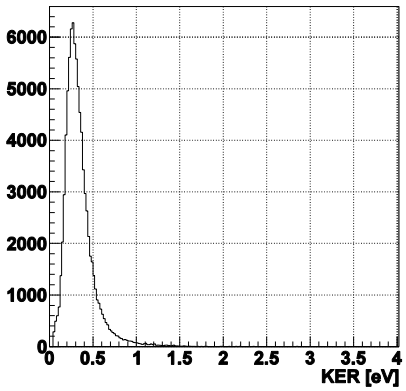

$\mathbf{He_2^+ - He_3^+}$

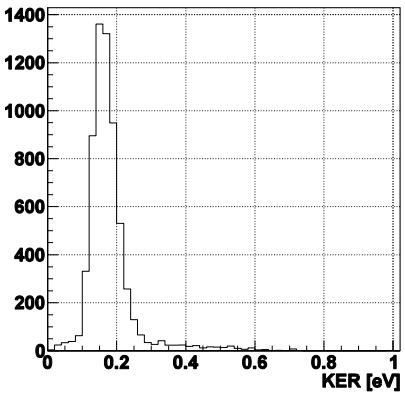

$\mathbf{He_6^+ - He_7^+}$

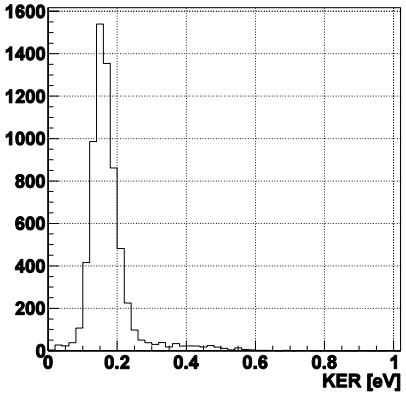

$\mathbf{He_6^+ - He_8^+}$

Figure 5.10: Similar spectra as shown in Figure 5.9, but for larger clusters (N~15000).

A comparison of the KER spectra from N~5000 to N~15000 cluster fragmentations shows slightly smaller values of the KER maxima for increasing cluster sizes. The difference between the KER maxima amounts to about 20% for larger fragments (Figure 5.11). Apparently, the KER in the various breakup channels depends stronger on the size of the larger fragment. The KER distributions observed in this experiment are in good agreement with the KER spectra presented in [5], even though the exact positions of the KER maxima differ by up to 18%. As noticed above, the cluster size related variation of the KER is in the same order of magnitude. Especially by taking into account that the target cluster size in [5] is unclear, this slight discrepancy is not unexpected. It is noteworthy that the KER in the $\mathbf{He^+ - He^+}$ channel shows, independent of the target cluster size, a slightly different distribution than in all other breakup channels that have been investigated.

As can be seen in Figure 5.9 and Figure 5.10, the $\mathbf{He^+ - He^+}$ distribution shows a very broad shoulder to the right side of the KER maximum reaching up to almost 9 eV. The significance of the higher KER becomes more obvious if the kinetic energy of the $\mathbf{He^+}$ ionic fragments is examined in more detail. Figure 5.12 shows ion energy correlation diagrams where the absolute kinetic energy of one helium ion is plotted against the kinetic energy of the ion measured in coincidence. An energy gate (7.86 ± 0.61) eV is set on high energetic ICD electrons.

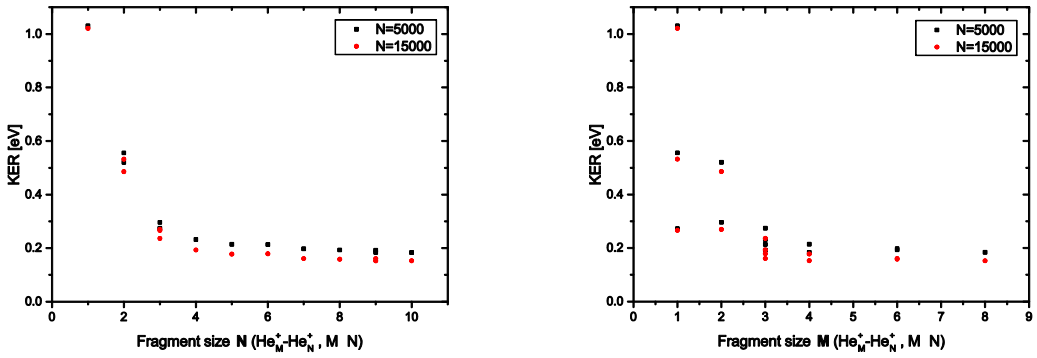

Figure 5.11: Position of the KER maxima in different breakup channels from cluster fragmentations of N~5000 and N~15000 clusters. The KER in each breakup channel $\mathbf{He_M^+ - He_N^+}$ is shown in dependence of the size N of the larger fragment (left) and the size M of the smaller fragment (right). The KER-decrease depends more on the size of the heavier ionic fragment.

The energy correlation diagrams depicted in Figure 5.12 reveal some evident structures. The diagrams can be partitioned in three regions. In **region one** below a sum energy of 3 eV both ions are slow while most events are located on a short diagonal with negative slop, i.e. a constant sum energy. The sum energy along this diagonal is about 1 eV high and leads to the KER maximum in the spectra seen before. In **region two** both ion energies are above 3 eV and an accumulation can be seen on a short diagonal with positive slope at sum energies around 8 eV. This diagonal is most apparent for N~5000 cluster fragmentations. In **region three** at least one helium ion has a high kinetic energy while the other ion has a lower kinetic energy.

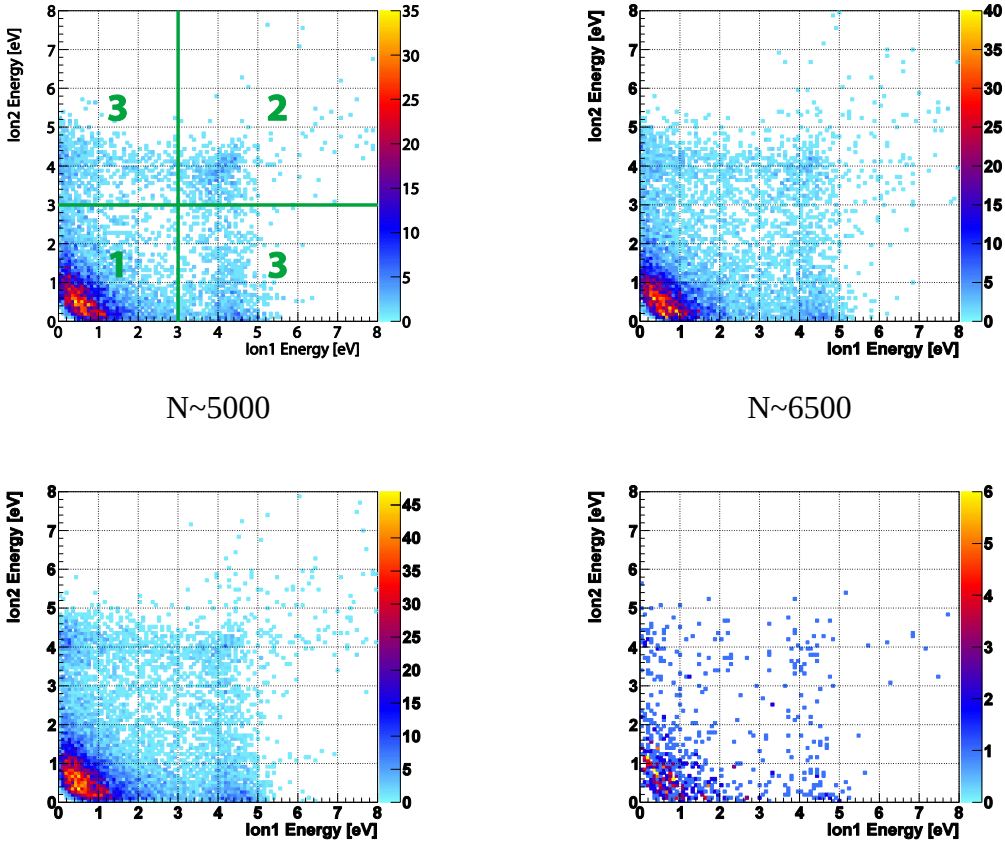

Figure 5.12: Correlation diagrams of the kinetic energies of the two coincident ions in the $\mathbf{He^+ - He^+}$ breakup channel from fragmentation of differently sized target clusters.

We suggest that the high energetic ion pairs from region three are created somewhere near the cluster surface from where the fragments can escape the cluster undisturbed, whereas ion pairs found in region one and two are formed inside the cluster and experience, in some way, massive energy loss on their way to the cluster surface.

A quite similar distribution of the ion energies is also obtained from semi classical simulations of N~5000 helium clusters fragmentations done by N. Sisourat by using the same method as described in chapter 2.5.2. The energy correlation diagrams obtained from the experimental data and the simulation results are depicted in Figure 5.13 and show qualitatively the same regions that are illustrated in Figure 5.12.

Moreover, the simulation have revealed that ions from the $\mathbf{He^+ - He^+}$ channel originate mostly from an about 40 Å thick shell near the cluster surface (Figure 5.14). The results also indicate that a substantial part of the low energetic ions from region one emerges from ICD between not-nearest-neighbor atoms (second shell atoms) on the cluster surface. The distributions of internuclear distances between ion pairs from region one and two at the moment of Interatomic Coulombic Decay are shown in Figure 5.15. The distribution for ion pairs from region one shows a maximum at 6.5 a.u. (3.4 Å) which is equivalent to twice the mean equilibrium distance between two helium atoms in a neutral cluster.

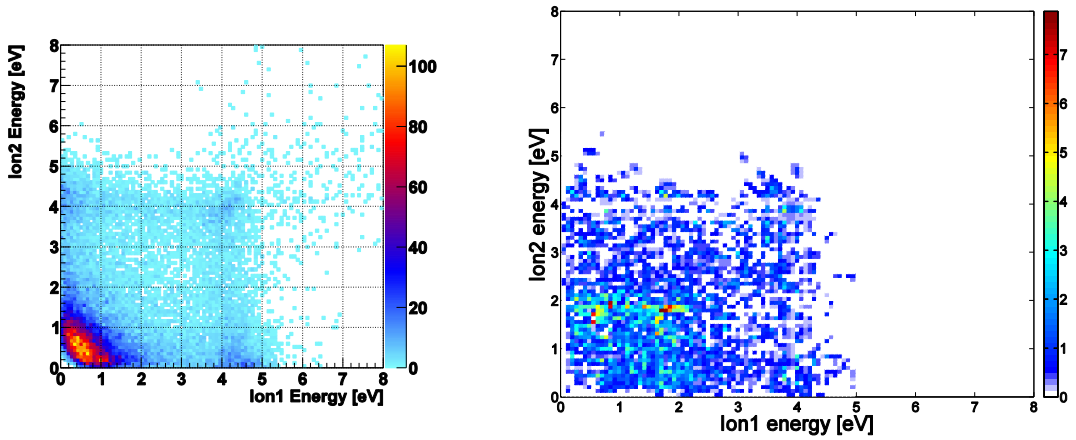

N~5000 Theory (simulation)

Figure 5.13: Ion energy correlation diagram from the simulated fragmentation of N~5000 clusters done by N. Sisourat **[37]** (right). The experimental results (II-V) (left) are qualitatively in good agreement with the simulation.

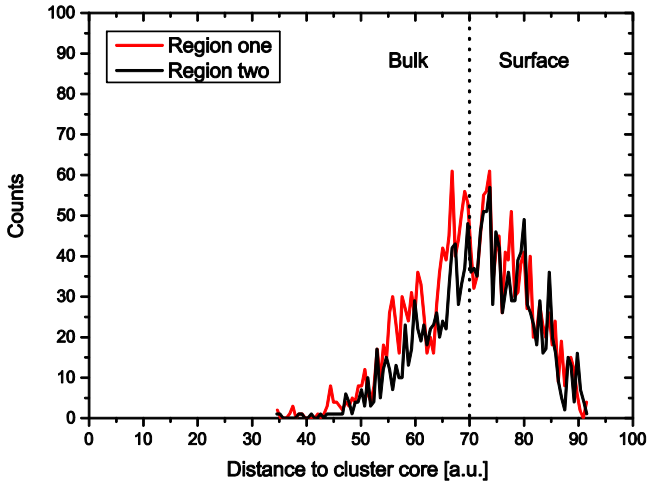

Theory (simulation)

Figure 5.14: Results of simulations done by N. Sisourat **[37]**. The distributions show the distance of cluster atoms and ion pairs of the $\mathbf{He^+ - He^+}$channel from the center of mass of the helium cluster. The red and black distributions indicate that ions in this breakup channel originate mostly from the cluster surface. The red distribution contains events from region two while the black distribution contains events from region one (Figure 5.12).

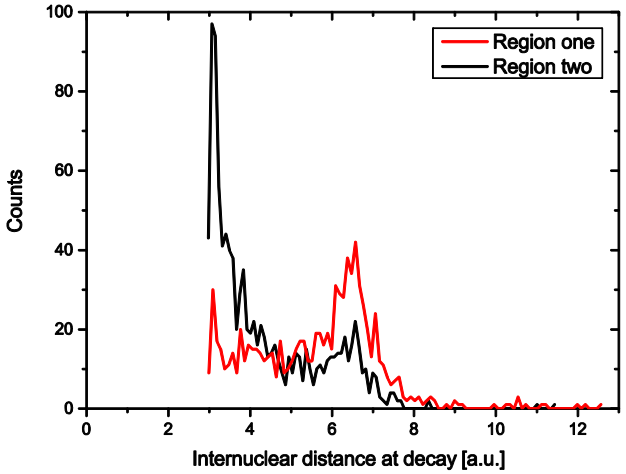

Theory (simulation)

Figure 5.15: Results from simulations done by N. Sisourat **[37]**. The distributions illustrate the internuclear distance of ion pairs from the $\mathbf{He^+ - He^+}$channel at the moment of ICD. The red distribution contains events from region one and shows a maximum at 6.5 a.u. (3.4 Å).

5.4 KER and electron energy correlation

The high energetic ions from region two can be associated to ICD near or on the surface of large helium clusters. Figure 5.16 shows the energy correlation between KER and electron energy with and without a two-dimensional energy gate on events from region two (Figure 5.12). Since the cluster size related KER variation in the $He^+ - He^+$ channel is small (about 9 meV), datasets II, III, IV and V (N~5000, N~6500, N~15000, N~30000) are merged to enlarge the data resource.

With reasonable certainty, events on the diagonal in Figure 5.16 can be associated with ICD in or on the surface layer of large helium clusters. Different to assumptions made in [5] the admixture of helium dimers in the gas targets under settings II to IV is negligible. The total prevalence of helium dimers and small clusters containing less than ten atoms can be estimated with equation (2.6) and is in the order of 10^{-18}.

Just as in [5] the energy correlation of KER and electron energy cannot be observed in any other than the $\mathbf{He^+ - He^+}$ channel (Figure 5.17). As described in the next section a helium ion-atom elastic scattering model can be employed as a plausible explanation for the energy loss of the helium ions. It is likely that larger fragments also interact with the cluster and dissipate kinetic energy which is why no clear energy correlation between ICD electron and decelerated ionic fragments can be observed anymore.

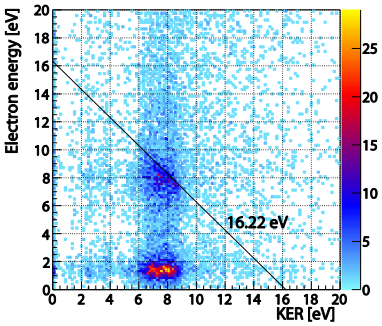

Energy correlation diagram

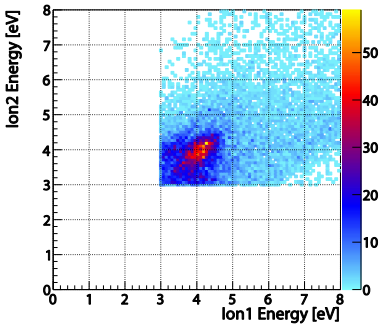

Gate on ion energies

Figure 5.16: Energy correlation diagram of KER and electron energy in the $\mathbf{He^+ - He^+}$ channel (left) with a gate on the ion energies (right). To enlarge the database, datasets II to V (N~5000-30000) have been merged. The diagonal at 16.22 eV marks the region where the decay energy is shared between ICD electron the ionic fragments.

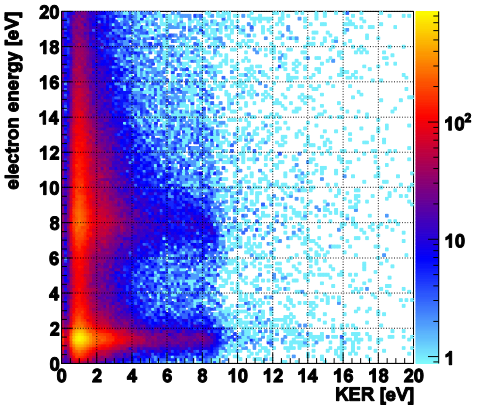

$\mathbf{He^+ - He^+}$

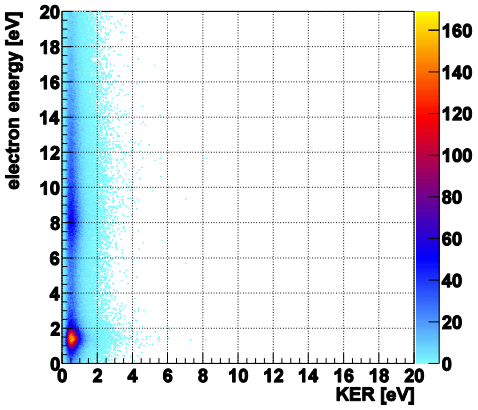

$\mathbf{He^+ - He_2^+}$

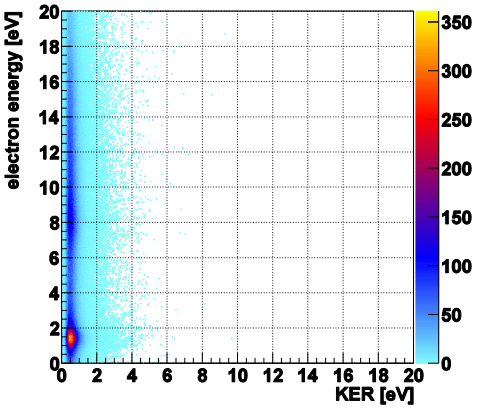

$\mathbf{He_2^+ - He_2^+}$

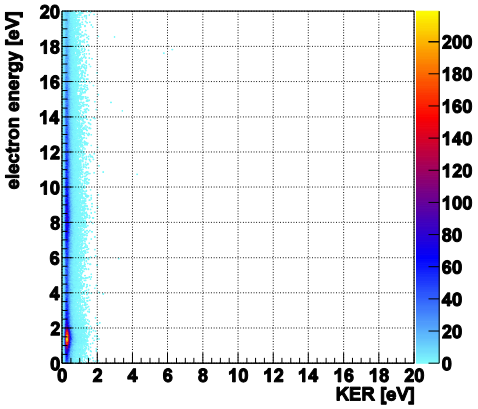

$\mathbf{He_2^+ - He_3^+}$

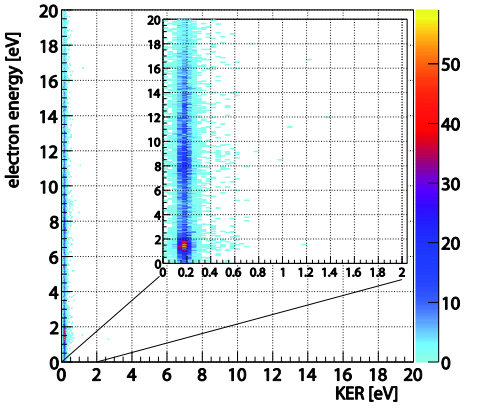

$\mathbf{He_6^+ - He_7^+}$

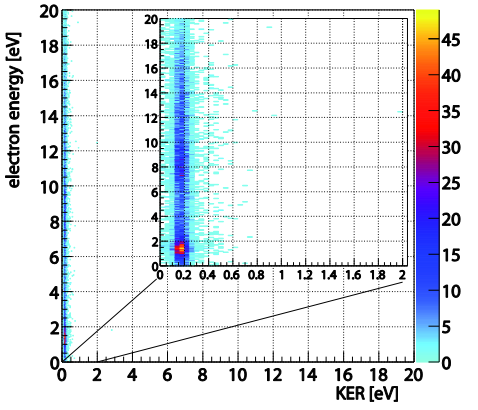

$\mathbf{He_6^+ - He_8^+}$

Figure 5.17: Correlation diagrams of KER and electron energy in different breakup channels without gates on specific ion energies. A clear energy correlation between ICD electron and KER is observed in the $\mathbf{He^+ - He^+}$ channel only. (Datasets II to V).

5.5 Ion angular distributions

Elastic scattering has already been introduced as a possible interaction of ionic fragments with neutral cluster atoms that leads to a massive energy loss of the fragments. As outlined in chapter 2.5.3 the transfer of momentum and kinetic energy to neutral cluster atoms in an elastic scattering process is only dependent of the scattering angle. Since the unaffected ions from an ICD induced Coulomb explosion fly back-to-back, the scattering angle can be reconstructed from the angle between the two ion momenta after interaction. This requires that at least one of the two ions has not been scattered so that the orientation of its momentum vector can serve as a fixed reference axis in space. In this picture the unaffected ions carry a high kinetic energy while the scattered ions are slowed down. The energy correlation diagrams in Figure 5.12 show two regions in which at least one ion has high kinetic energy. With an energy gate on electrons around (7.86±0.61) eV and a two-dimensional energy gate on events from region two and three (Figure 5.18), the absolute kinetic energy of the slower ion can be plotted respectively in relation to the angle between the momentum vectors of the two ions (“breakup angle”).

The energy distribution of the slower ions depicted in Figure 5.19 shows an apparent correlation to the breakup angle. An energy maximum is found around 4 eV where the breakup angle is nearly 180°. At smaller angles the decelerated ions seem to follow the elastic scattering model already known from chapter 2.5.3.

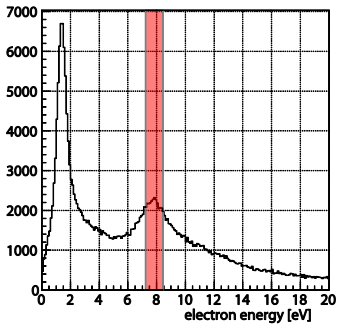

Energy gate on electrons

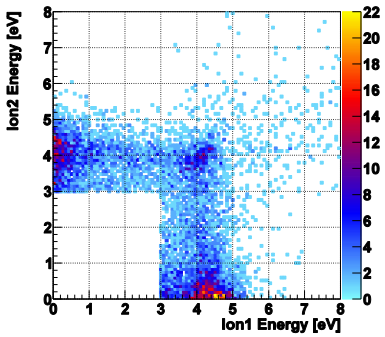

Energy gate on ions

Figure 5.18: Gate on high energetic ICD electrons at (7.86±0.61) eV (left) and two dimensional energy gate on region two and three (right). (Datasets II to V)

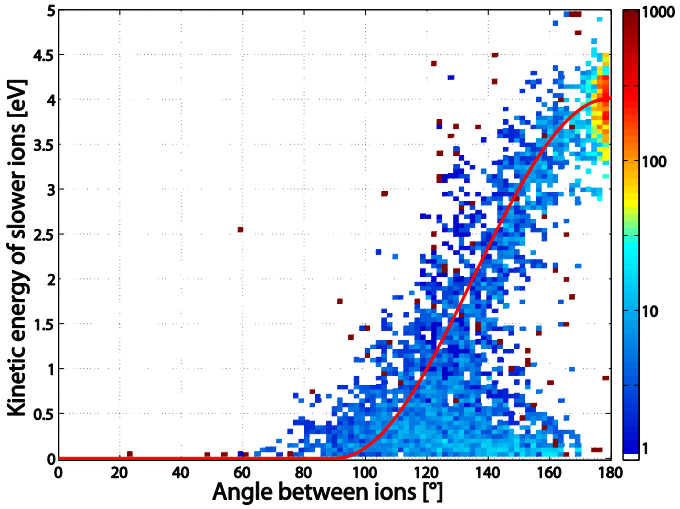

Experimental results

Figure 5.19: Energy distribution of the slower ions from region two and three relative to the breakup angle. The red curve illustrates the angle-dependent energy loss of the scattered particle in case of helium ion-atom scattering according to the elastic scattering model presented in chapter 2.5.3. (Datasets II to V)

Figure 5.19 shows a comparison of the angular distribution of the ion energy observed in this experiment and the elastic scattering model. The parameters for the initial kinetic energy of the scattered ion and the masses of the scattering partners have been set to $E_1 = 4$ eV and $m_1 = m_2 = 4$ amu. Evidently, the angle-dependent energy distribution and the elastic scattering model show a close match. A nonlinear regression of the model parameters to the experimental data, based upon the scattering model, reproduces the presumed mass relation $m_1/m_2 = 1$ for the helium ion-atom elastic scattering. This suggests that the energy loss of ionic fragments can in fact be traced back to binary collisions with cluster atoms. As reported in [52] and [53], classical Monte Carlo simulations, accompanying photodissociation experiments on alkyl iodides embedded in large helium nanodroplets, lead to the same conclusion.

A quite similar angle-dependent kinetic energy distribution of the slow ions from the $\mathbf{He^+ - He^+}$ channel is also obtained from simulations done by N. Sisourat in 2014 [37]. The simulation results depicted in Figure 5.20 and the experimental results presented in Figure 5.19 show a strong analogy. Both distributions suggest that helium ions are deflected from their straight path and lose kinetic energy while making their way through the cluster. However, the distributions differ as far as details are concerned.

While the ion energy in the experimental results lays comparatively close to the ideal curve, the ion energy in the simulation results shows a very wide spread.

Especially at breakup angles wider than 140° and low kinetic energies in the range between 0.5 and 2.5 eV considerably fewer ions are found in the experiment than in the simulation results. By applying a two-dimensional gate on the simulated results, it can be shown that events from this area stem partly from region one (Figure 5.21).

Analyses of the simulation results also indicate that ion pairs in this region could partly have their origin in ICD between second shell neighbors (Figure 5.15). The dissociation of not-directly-neighboring cluster atom pairs results in a lower KER (cf. equation (2.29)) and a higher kinetic energy of the ICD electron (Figure 5.24). The initial energy of the ionic fragments from a second shell dissociation is expected to be approx. 2 eV per ion. A comparison of the simulation results to the elastic scattering model is made in Figure 5.20. The two curves show the angle-dependent energy loss of the scattered particle for two different energies E_1 according to the expected initial energies in case of a first shell or a second shell neighbor dissociation. As can be seen to some degree, the inner rim of the distribution follows the ideal curve for an elastic scattering of high energetic ions from a first shell neighbor dissociation.

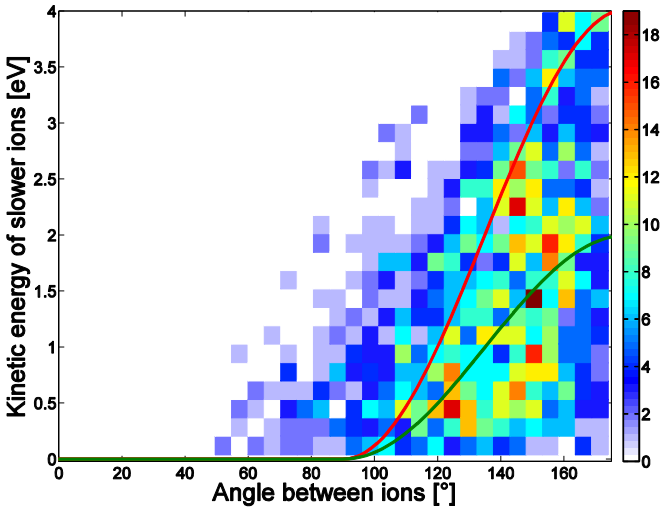

Theory (simulation)

Figure 5.20: Results from simulations done by N. Sisourat **[37]**. The distribution shows the kinetic energy of the slower ions from region two and three relative to the breakup angle. The curves show the energy loss of the scattered particle according to ideal elastic ion-atom scattering if the initial energy is $\boldsymbol{E_1 = 4\ eV}$ (red curve) and $\boldsymbol{E_1 = 2\ eV}$ (green curve).

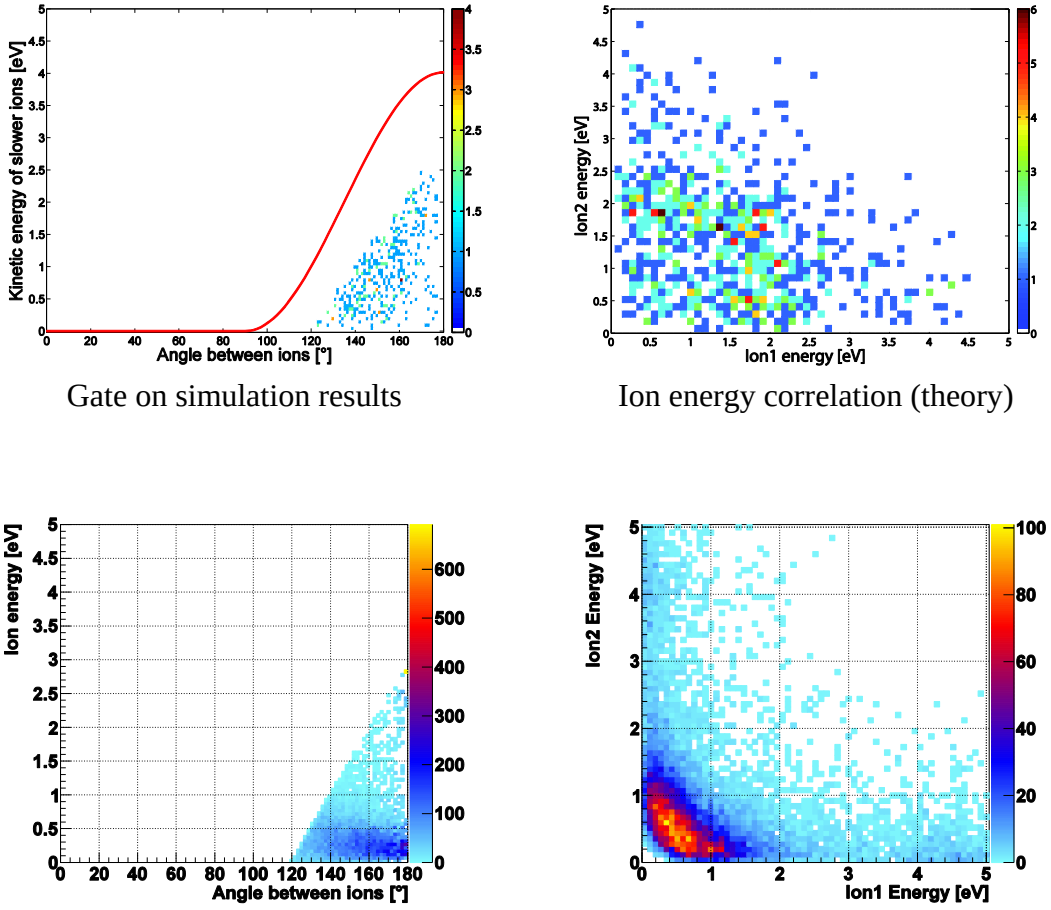

Gate on simulation results | Ion energy correlation (theory)

Gate on experimental results | Ion energy correlation (experiment)

Figure 5.21: Results from simulations done by N. Sisourat **[37]**. The energy correlation diagrams of the ions from the $\mathbf{He^+ - He^+}$ fragmentation channel are depicted in the right column. The applied gates on different areas of the distribution in Figure 5.20 are shown in the left column. (Datasets II to V)

With gates, set on different regions in the angle-dependent energy distribution of the slower ions from the $\mathbf{He^+ - He^+}$ channel, further parallels between experimental results and simulation can be seen. Figure 5.21 shows the ion energy correlation diagram **of slower and faster** ions (right column) from theory and experiment with a gate in the angular distribution of the **slower** ions which requires an kinetic energy between 0 eV and 3 eV and wide breakup angles of more than 120° (left column). Both correlation diagrams (right column) show an accumulation of ion pairs with sum energy of less than 6 eV. Ion pairs with high sum energies above 6 eV are strongly suppressed.

In contrast, Figure 5.22 shows the equivalent correlation diagrams from experiment and simulation (right column) but with a complementary gate in the ion energy angular distribution (left column). Here again, the experimental results and the simulation show qualitatively a close match. The correlation diagrams in Figure 5.22 show substantially more entries with sum energies higher than 6 eV.

However, direct comparisons of the raw ion energy correlation from experiment and simulation as done in Figure 5.13 show that in the experiment both, faster and slower ions in region one, carry about 1 eV less kinetic energy. The kinetic energy of slower and faster ions from region one shows a much wider angular dependence (Figure 5.23).

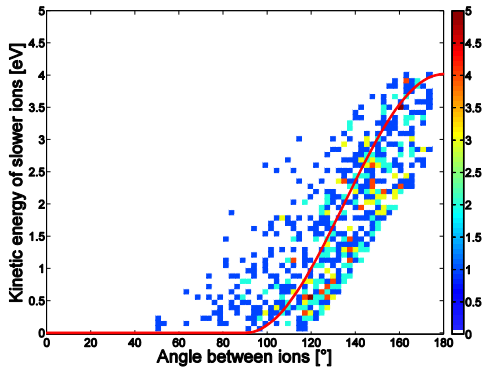

Gate on simulation results

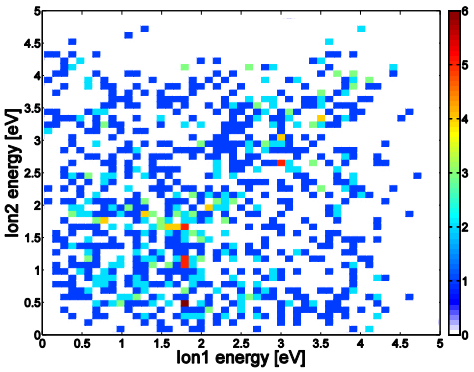

Ion energy correlation

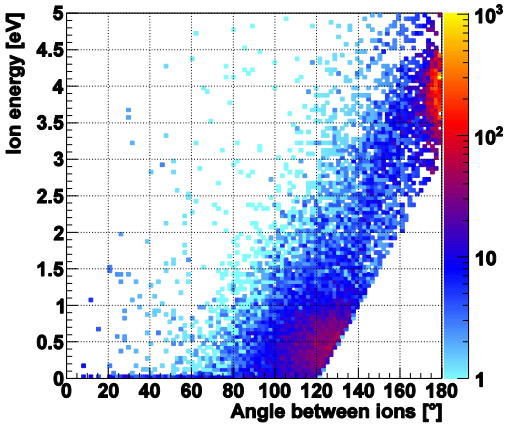

Gate on experimental results

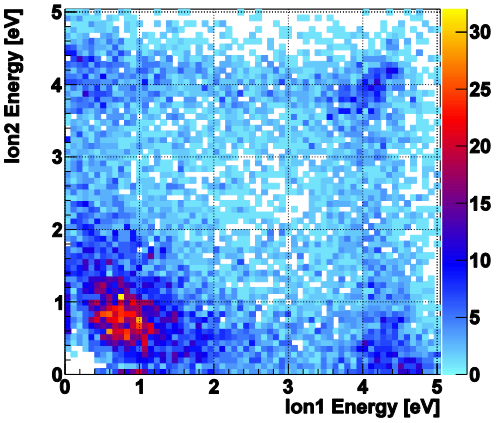

Ion energy correlation

Figure 5.22: Results from simulations done by N. Sisourat **[37]**. Energy correlation diagram of the ions from the $\mathbf{He^+ - He^+}$ fragmentation channel (right column) with gates (left column) on different areas of the spectrum presented in Figure 5.20. (Datasets II to V)

Figure 5.23 shows the ion energy angular-distribution of the slower ions in the $\mathbf{He^+ - He^+}$ channel with a gate set on region one (upper row) and without gate on the ion energy (bottom row). As can be clearly seen, elastic scattering of ions from neutral cluster atoms is observed only for the ions from region two and three whereas the events in region one are found at lower energies and show more isotropic breakup angles wider than 90°. This is an indication that the ions from region one emerge from different ICD processes than ions from region two and three or undergo different energy dissipative processes. Figure 5.24 shows the ion energy correlation of the slower and faster ions in the $\mathbf{He^+ - He^+}$ channel with energy gates set on two different regions of the electron energy. The two gates are set at (7.86±0.61) eV and at (12.04±0.61) eV.

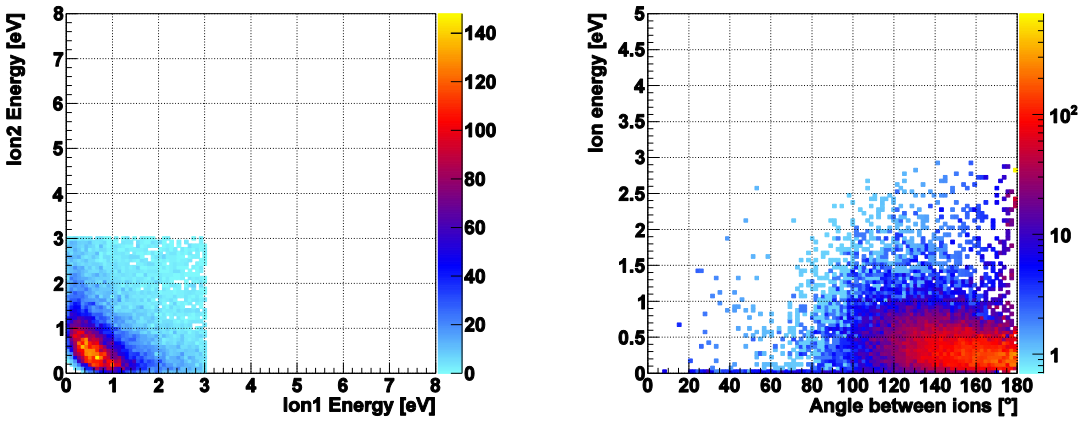

Gate on region one | Slower ions from region one

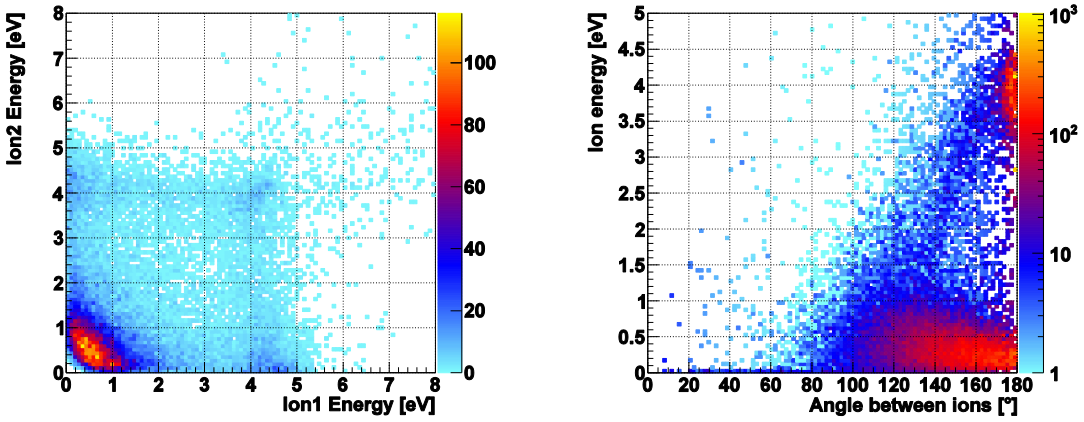

No energy gate | Slower ions from region one

Figure 5.23: Angle dependent energy distribution of the slower with energy gate on region one (upper row) and without energy gate (bottom row). (Datasets II to V).

The energy gates are chosen considering two different KER regions which correlate with first shell or second shell neighbor dissociations. The ion energy correlation diagrams in Figure 5.24 show a slight suppression of events in in region two and three if the gate is set around 12 eV. The relative number of events in region one (relative to the number of events in region two and three) is approx. (12.2 ± 0.2) % smaller with a gate set on ICD electrons of 8 eV. This is an indication that, in fact, events in region one emerge partly from second shell neighbor dissociations which result in a lower KER (larger internuclear distance) and a higher ICD electron energy. It is implausible that the significantly lower kinetic energy of ions from region one can be attributed exclusively to multiple scattering of one or both ions from a first shell neighbor dissociation.

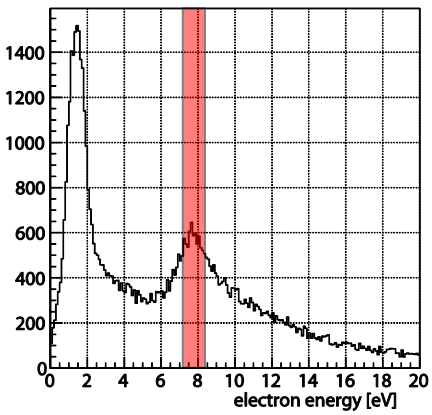

Gate on 8 eV ICD electrons

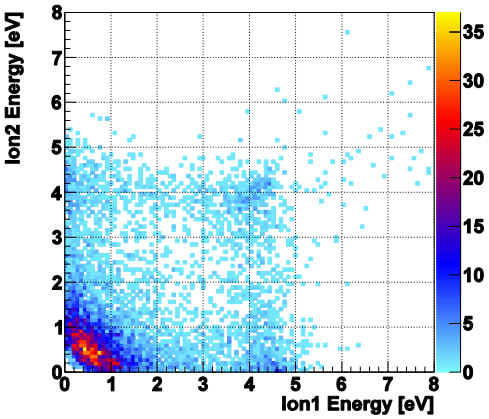

Ion energy correlation

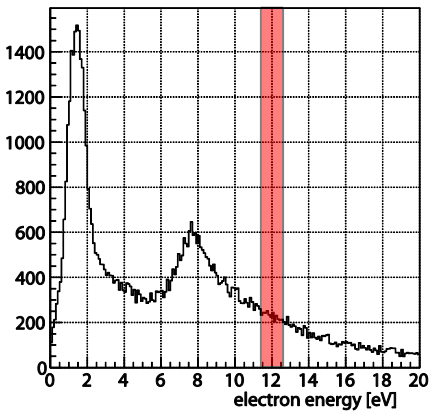

Gate on 12 eV ICD electrons

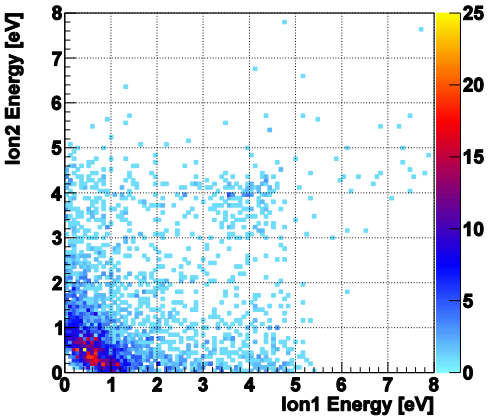

Ion energy correlation

Figure 5.24: Ion energy correlation diagrams with gates on different regions of the ICD electron energy. (Dataset II)

Both ions in region one carry a low kinetic energy while at the same time, the kinetic energy of the ions does not seem to follow a scattering curve (Figure 5.23 upper row). If elastic scattering were significantly contributing to the energy loss of those fragment ions, this would imply that both fragments must have been scattered. In each fragmentation, the momentum vector of the faster ion is employed to define a fix reference axis in space. The breakup angle, respectively the scattering angle, is reconstructed relative to this axis. If both particles are scattered, the orientation of the reference axis is altered and a second scattering angle has to be introduced. As a result, all imaginable combinations of the two scattering angles lead to an equally distributed incidence of all possible breakup angles from 0° to 180° in the ion energy angular-distribution. A similar distribution could also be observed if one or both ions are multiply scattered. In fact, no isotropic distribution is observed in the experiment (Figure 5.23), where only a few events are found at breakup angles smaller than 90°.

With regard to these findings, it is conceivable that the low energetic ions in region one stem partly from second-shell-neighbor dissociations with a lower KER while the fragment energy is additionally absorbed during their flight through the cluster. Experiments reported in [16], [52] and [53] have indicated that in superfluid helium nanodroplets translational energy of ions can be dissipated by excitation of phonons and ripplons and by subsequent evaporation of atoms from the droplet surface. The cooling capacity of N~5000 droplets has been estimated in [16] as large as 3 eV. A quite similar estimation is made in [54] and [55], where the evaporation of about 1800 helium atoms from the droplet surface is suspected to dissipate about 1 eV of thermal energy (~7 K (~0.6 meV) per evaporated helium atom [26]). The timescale for this energy absorption is in the order of less than 1 ps/eV [16]. Considering the initial fragment speed in the order of 10^4 m/s (at 2 eV initial fragment energy), the escape time of the fragment ions from a midsized cluster ($N\sim10^4$) is, depending on the starting point inside the cluster, longer than 1 ps. Additionally, deposited rotational energy and angular momentum of up to several thousand ħ can be absorbed by the formation of quantum vortices in the droplet due to the quantum nature of the superfluid [55] [56]. It is conceivable that the absorption of kinetic energy by the droplet is a continuous process which gradually decelerates the fragments while having a smaller influence on the deflection of the ions compared with the hard sphere scattering process described above.

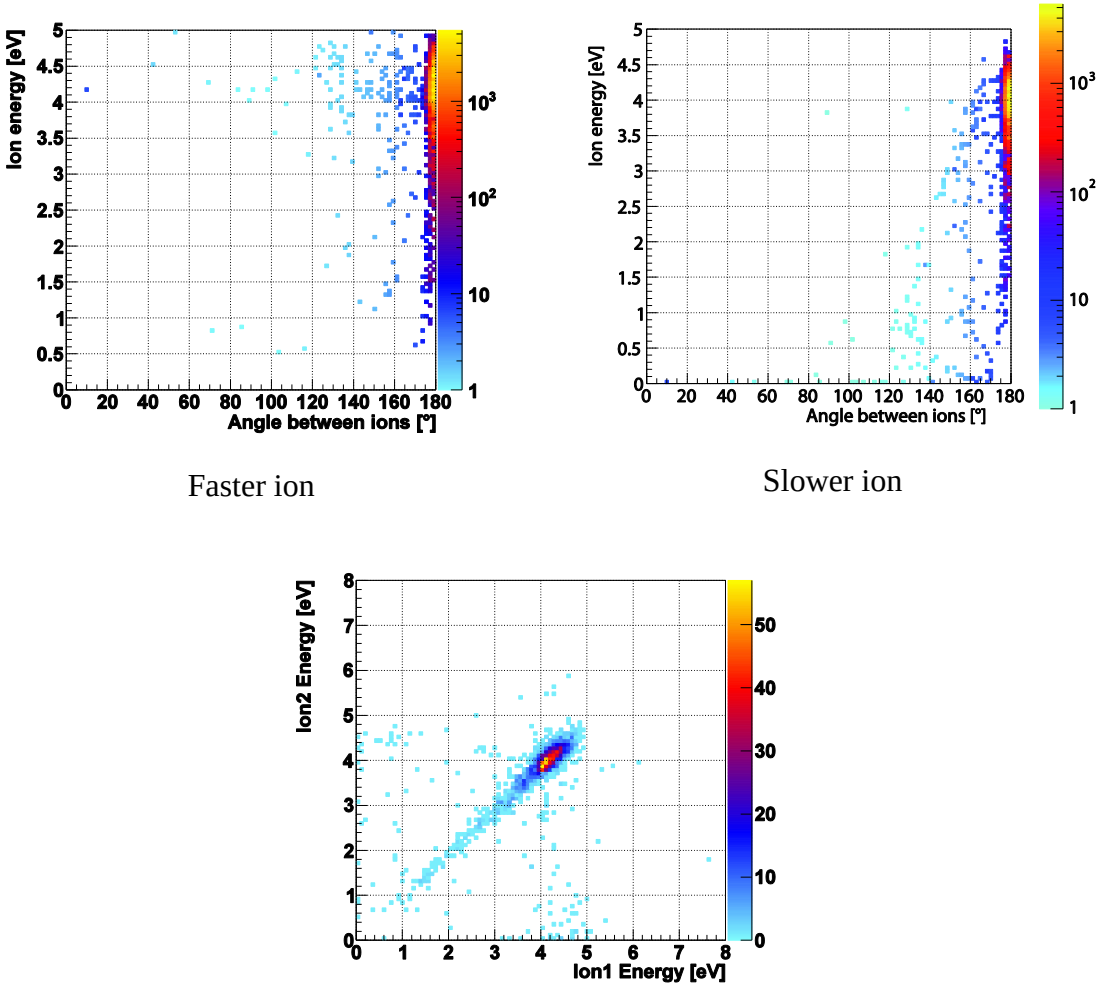

Figure 5.25: Ion kinetic energy angular-distribution of slower and faster fragments from a dimer fragmentation (upper row). Fragment energy correlation (bottom row).

The ion energy correlation in other breakup channels shows only events with small sum energies in region one (Figure 5.26) while the ion energy angular-distributions in those channels shows no indication of an elastic scattering of the fragment ions (Figure 5.27). The ion energy correlation and kinetic energy angular-distribution in the $\mathbf{He^+ - He^+}$ channel from a dimer fragmentation is displayed in Figure 5.25 and shows almost exclusively breakup angles of nearly 180 degrees. This is a strong indication that the correlations seen in the fragmentation of larger clusters is probably not an artifact. The isolated events at smaller breakup angles in Figure 5.25 could stem from few larger clusters (<0.6% of N>10 clusters) in the largely dimer-populated gas target in setting **I**.

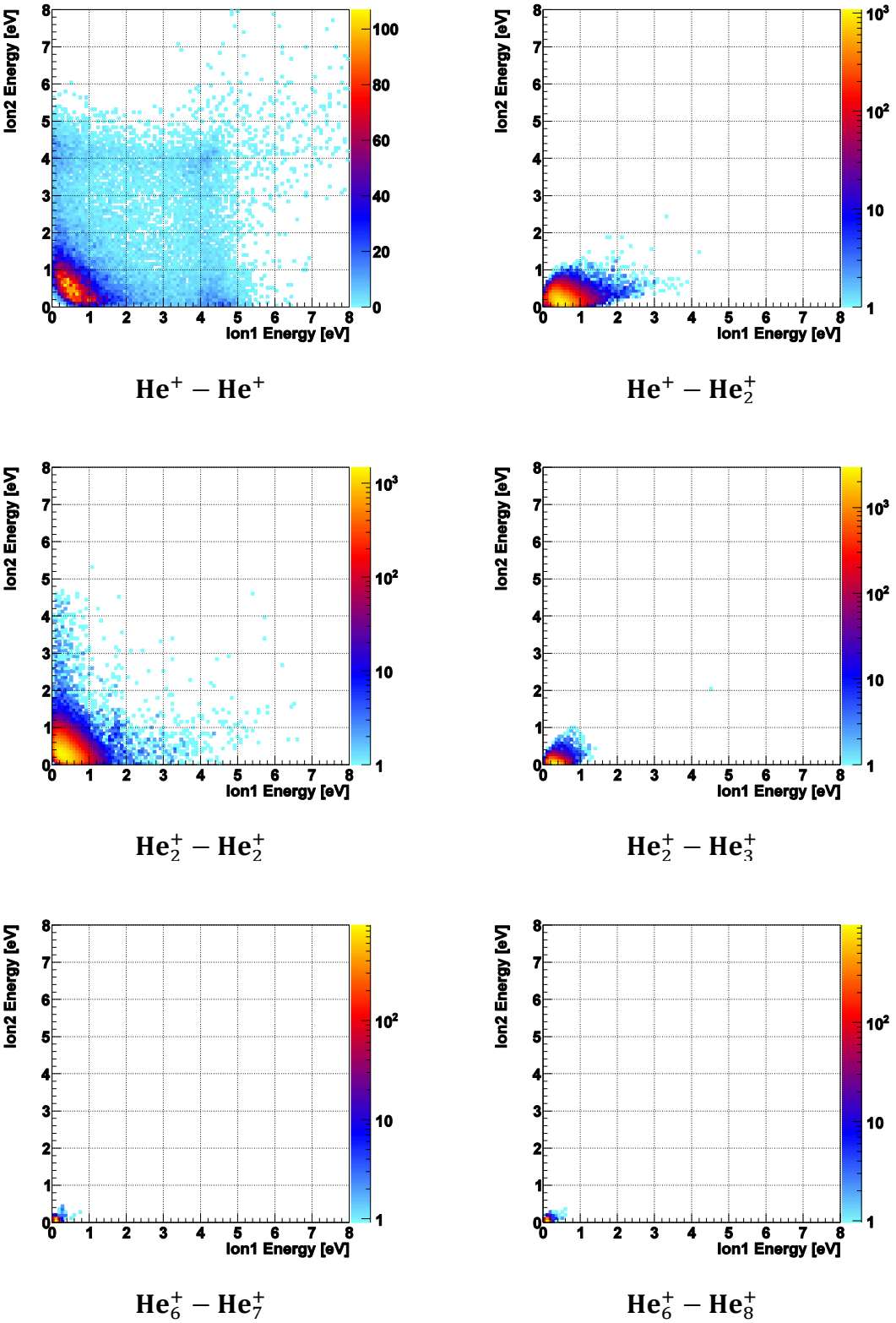

Figure 5.26: Ion energy correlation in different breakup channels. (N~5000-30000).

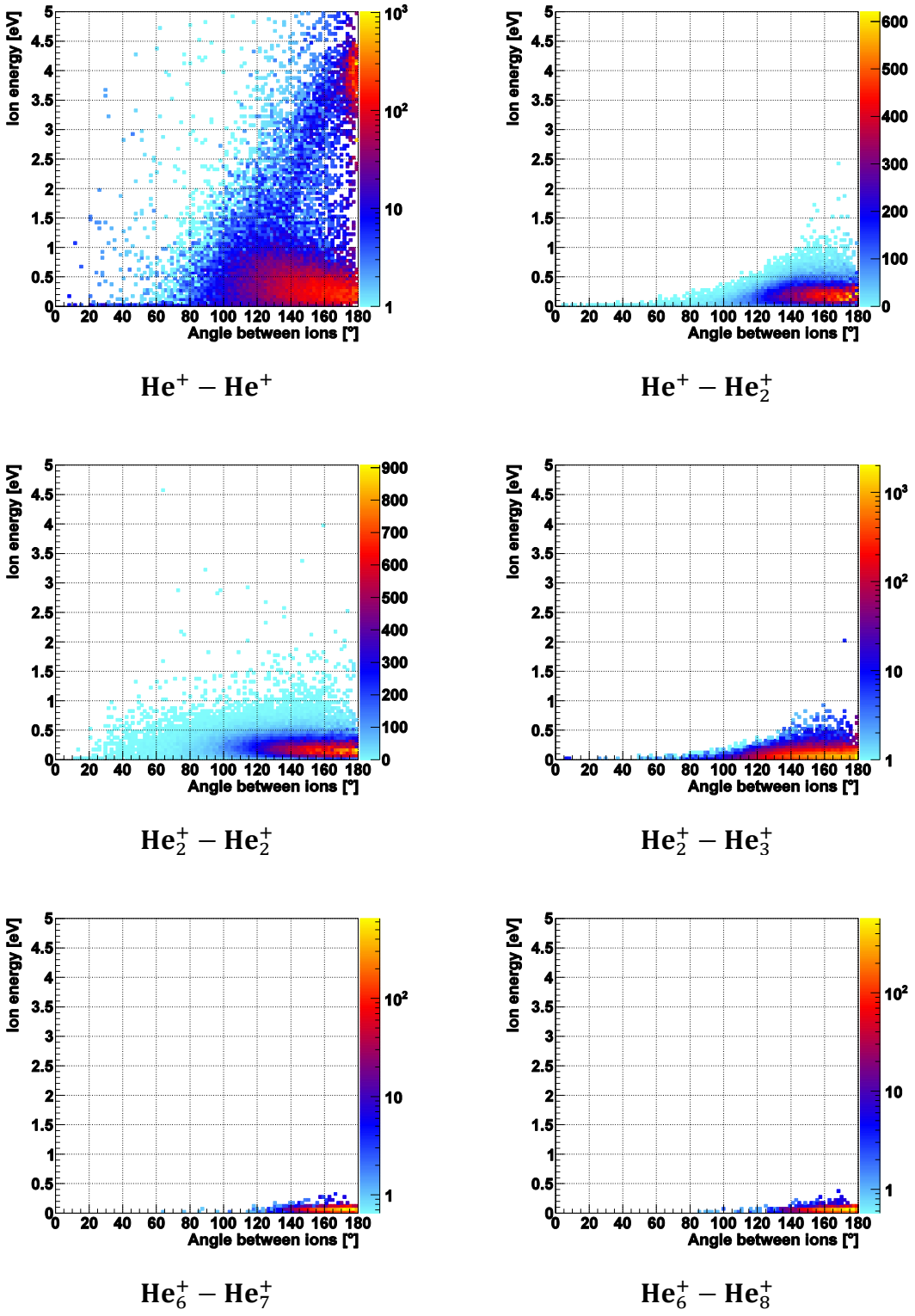

Figure 5.27: Angular distribution of the kinetic energy of the slower fragment in different breakup channels without gate on specific regions of the ion energy correlation diagram. (Datasets II to V)

5.6 Electron angular distributions

The COLTRIMS technique provides a complete overview of the ion dynamics as well as on the dynamics of photoelectron and ICD electron emitted during the cluster fragmentation. The high energetic ICD electrons have been employed as a marker for the ICD induced cluster fragmentation. In the previous section the angular distribution of the fragment ions has been presented showing a significant number of ion pairs with a high kinetic energy and with breakup angles of nearly 180 degrees. Comparisons with the angular distribution of the fragment ions from a dimer fragmentation (Figure 5.25) confirm that these ions emerge most likely from ICD induced Coulomb explosions.

In a Coulomb explosion the ions fly back-to-back along a dissociation axis which is also called the molecular axis. Since the ICD electron is emitted simultaneously to the Coulomb explosion, the emission angle of the ICD electron in the molecular frame can be determined relative to the dissociation axis [8].

The polar plot in Figure 5.28 shows the emission angles of the high energetic ICD electrons (7.86 ± 2.0) eV relative to the molecular axis. A gate has been set on ion pairs from region two (KER >6eV) which show breakup angles wider than 175°. The shape of the electron angular distribution observed in this experiment is qualitatively in good agreement with the shape of the angular distributions presented in [8].

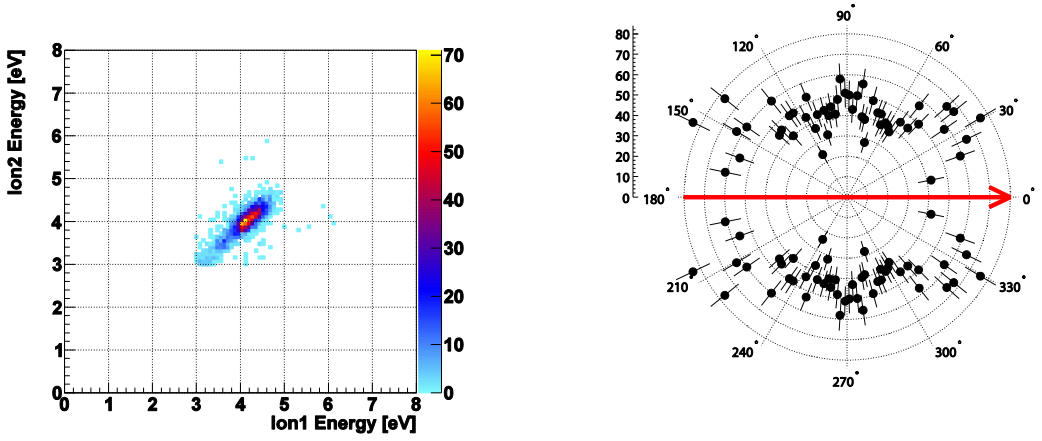

Gate on region 2 Electron angular distribution

Figure 5.28: Angular distribution of the ICD electrons around 8 eV from dimer fragmentations. The angular distribution is shown in the molecular frame relative to the dissociation axis defined by the relative momentum vector of the fragments (red arrow).

The characteristic structures in the angular distribution of the ICD electron relative to the molecular axis observed in the dimer fragmentation experiment (Figure 5.28) are not any more visible in the analog angular distributions obtained from the cluster fragmentation experiment (Figure 5.29). The fine structures are, to some degree, still lightly marked in the electron angular distribution from the region two whereas the emission angles of the ICD electrons relative to the dissociation axes of the fragment pairs are almost equally distributed in region one and three.

It is conceivable that the ICD electrons found in region two are emitted from a dissociation of two helium atoms closer to the cluster surface than in the other regions. Near the cluster surface the particles have a much shorter escape path and lose less kinetic energy which is why the electron angular distribution is not as strongly affected and both fragments retain a high kinetic energy. It is also possible that ion pairs from region two and from region three are created near the droplet surface while ions from region two escape tangentially to surface whereas ion pairs in region three dissociate vertically to the droplet surface so that one ion can escape the cluster with less interaction while the other ion penetrates deep into the cluster and loses kinetic energy.

In case of dimer fragmentations (Figure 5.28), the electron angular distribution indicates an overall preferential emission direction of the high energetic ICD electrons along the dissociation axis. In case of a cluster fragmentation (Figure 5.29), the emission direction of the ICD electrons along this axis is, compared to the 90° emission direction, slightly suppressed in region one and three. Furthermore, the emission direction along the flight path of the slower fragment (pointing in direction of 180°) is also slightly suppressed compared with the emission in direction of the faster ionic fragment (pointing direction of 0°). This could also be an indication that the slower ions in region three are emitted towards the droplet.

All in all, it is not yet fully determined whether the change in the angular distribution of the ICD electron for the different regions of the ion energy correlation diagram is significant and not an artifact.

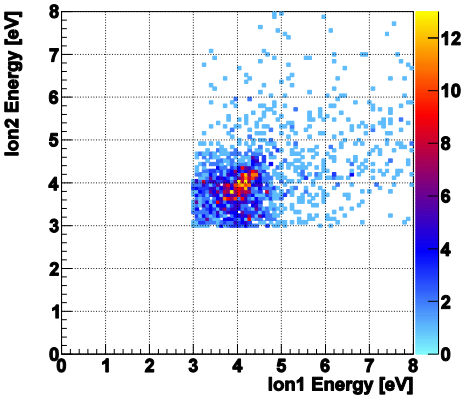

Gate on region 2

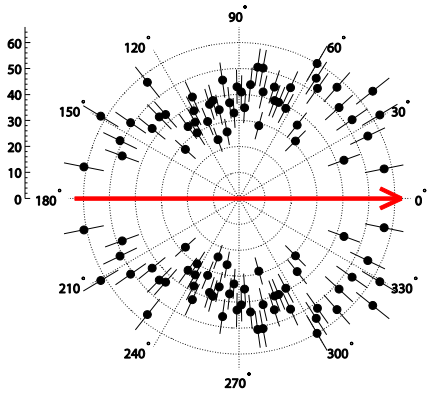

Electron angular distribution

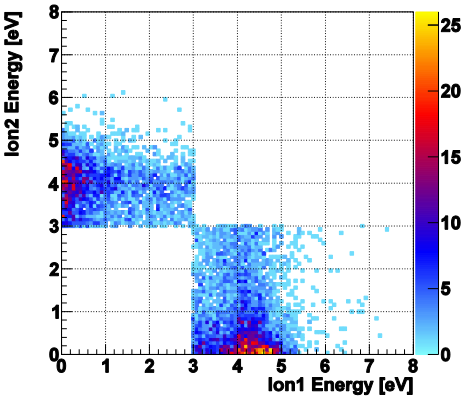

Gate on region 3

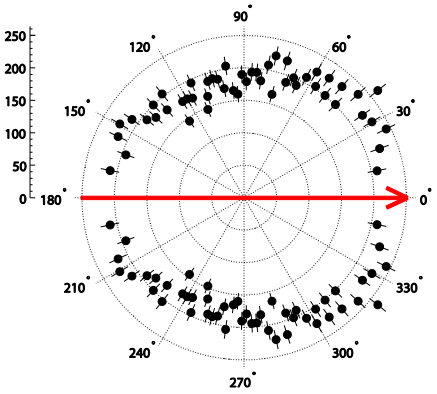

Electron angular distribution

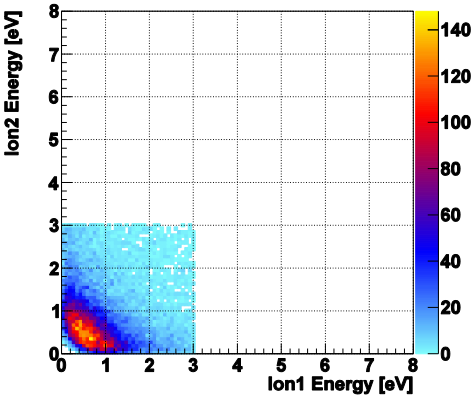

Gate on region 1

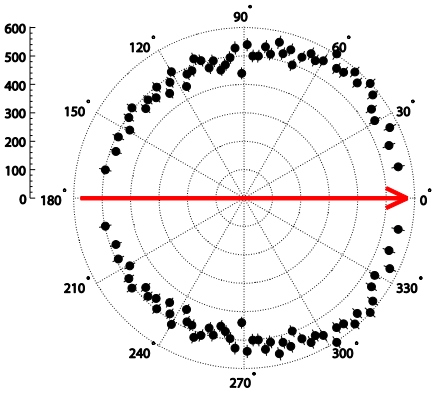

Electron angular distribution

Figure 5.29: Angular-distribution of the ICD electrons relative to the dissociation axis in the $\mathbf{He^+ - He^+}$ channel from cluster fragmentation experiments (II-V) with energy gates set on different regions in the ion energy correlation diagram. The dissociation axis is defined by the relative momentum of the fragments (red arrow).

Chapter 6

Summary

In this work the fragmentation dynamics of helium nanodroplets after interatomic Coulombic decay induced by photoexcitation has been investigated. A molecular beam of ultra-cold helium gas containing clusters of mean sizes between N~5000 and N~200000 was crossed with a photon beam of $h\nu = 67$ eV from the BESSY II synchrotron light source. It has been shown that the VUV radiation causes ionization and fragmentation of the helium nanodroplets. By using the COLTRIMS technique the momenta of the ions and electrons emitted from the point of interaction have been measured which provide an entire view on the dynamics of the charged particles emitted after ionization and ICD in the droplets. The distribution of the various breakup channels available for the cluster fragmentation has been characterized revealing that large helium droplets break up mostly into small ionic fragments which contain less than twenty helium atoms. The experiment has indicated that the fragment size is largely independent of the target cluster size. Energy spectra of the emitted electrons as well as KER spectra from different breakup channels have been presented. A distinct correlation of KER and kinetic energy of the electrons with energies around 8 eV in the $\mathbf{He^+ - He^+}$ breakup channel has been observed linking the cluster fragmentation and the ICD process. The measured fragment energies and the kinetic energy release in all investigated breakup channels are significantly smaller than the KER found in semi

classical simulations done in 2013 by N. Sisourat but is in good agreement with the KER observed in the experiment reported in [5].

Two energy dissipative processes have been discussed in the present work which can explain the discrepancy between theory and experiment. It must be assumed that binary elastic scattering of the $\mathbf{He}^+$ ionic fragments from neutral cluster atoms leads to momentum transfer and to a substantial loss of kinetic energy. The characteristic relation between energy loss and scattering angle is observed in the angular distribution of the kinetic energy of the slower $\mathbf{He}^+$ ions from the $\mathbf{He}^+ - \mathbf{He}^+$ fragmentation channel presented in chapter 5.5. Furthermore, this distribution indicates that other energy dissipative processes such as the excitation of phonon and ripplon modes of the superfluid helium droplets and subsequent evaporation of atoms from the cluster surface have a strong cooling effect which significantly contributes to the energy loss of the fragments inside the droplets.

Analyses and comparisons between experimental data and the results from accompanying semi classical simulations done by N. Sisourat in 2014 and 2015 have indicated that a considerable part of the observed ion pairs which carry a low kinetic energy are created in an interatomic Coulombic decay between second shell neighbor atoms near the cluster surface. The greater internuclear distance leads to a much smaller kinetic energy release compared to a first shell neighbor dissociation.

The angular distribution of the collected high energetic ICD electrons in the molecular frame of the dissociating cluster atoms shows slight changes compared to the angular distribution observed in dimer fragmentations which could indicate that the ICD electrons interact with the cluster, and that the fragment ions are emitted in different directions relative to the cluster surface.

The direct observation of ion-atom binary elastic scattering of positively charged ions from cluster atoms substantially contributes to a more complete picture of the motion of charged particles inside helium nanodroplets which could be of considerable relevance for future experiments which employ helium nanodroplets as a carrier matrix for dopant atoms such as often done in atomic and molecular spectroscopy.

Experimental parameters

Spectrometer

Fields		Unit
Electric field	18.27	V/cm
Magnetic field	6.25	Gauss
Length		
Ion acceleration region	35.5	mm
Ion drift region	75.2	mm
Electron acceleration region	74.5	mm
Electron drift region	161.5	mm

Cluster source

Nozzle		Unit
Nozzle diameter	5	µm
Temperatures	10-14.5	K
Pressures	1.5-50	bar
First skimmer diameter	300	µm
Second skimmer diameter	300	µm

Beamline

TGM-7		Unit
Source	D151 Bending magnet	
Monochromator	Toroidal grating monochromator	
Energy range	8 - 120	eV
Energy resolution	500	E/ΔE
Photon flux	10^{12}	s^{-1}
Polarization	Horizontal	
Horizontal divergence	~	mrad
Vertical divergence	~	mrad
Horizontal focus size	100	µm
Vertical focus size	1	mm

Bibliography

[1] F. Luo and co-workers, "Influence of retardation on the vibrational wave-function and binding-energy of the Helium dimer," *J. Chem. Phys. 98, 9687,* 1993.

[2] J. Seong and co-workers, "Short-time charge motion in He n + clusters," *J. Chem. Phys. 109, 10873,* 1998.

[3] D. Buchta and co-workers, "Extreme ultraviolet ionization of pure He nanodroplets: Mass-correlated photoelectron imaging, Penning ionization, and electron energy-loss spectra," *J. Chem. Phys. 139, 084301,* 2013.

[4] "Cold Target Recoil Ion Momentum Spectroscopy COLTRIMS," Goethe-Universität Frankfurt, [Online]. Available: http://www.atom.uni-frankfurt.de/research/coltrims/. [Accessed 08 02 2015].

[5] C. Müller, Diploma Thesis - Untersuchung der Ionisationsdynamik von Helium-Clustern, Goethe-Universität Frankfurt, 2013.

[6] L. S. Cederbaum, J. Zobeley and F. Tarantelli, "Giant Intermolecular Decay and Fragmentation of Clusters," *Phys. Rev. Lett. 79, 4778,* 1997.

[7] T. Jahnke and co-workers, "Experimental Observation of Interatomic Coulombic Decay in Neon Dimers," *Phys. Rev. Lett. 93, 163401,* 2004.

[8] T. Havermeier, PhD Thesis - Photoionisation von Helium Dimeren, Goethe-Universität Frankfurt, 2010.

[9] NikelsenH, "Wikipedia," 14 June 2015. [Online]. Available: httpde.wikipedia.orgwikiMolek%C3%BClorbitaltheorie. [Accessed 19 July 2015].

[10] K. T. Tang, J. P. Toennies and C. L. Yiu, "Accurate Analytical He-He van der Waals Potential Based on pertubation Theory," *Phys. Rev. Lett. 74, 1546,* 1995.

[11] R. E. Grisenti and co-workers, "Determination of the Bond Length and Binding Energy of the Helium Dimer by Diffraction from a Transmission Grating," *Phys. Rev. Lett. 85, 2284,* 2000.

[12] D. Bressanini and co-workers, "Quantum Monte Carlo investigation of small ^{4}He clusters with a ^{3}He impurity," *J. Chem. Phys. 112, 717,* 2000.

[13] J. Kim and co-workers, "Photoionization of helium nanodroplets doped with rare gas atoms," *J. Chem. Phys. 124, 214301,* 2006.

[14] M. Rosenblit and J. Jortner, "Electron bobbles in helium clusters. I. Structure and energetics," *J. Chem. Phys. 124, 194505,* 2006.

[15] K. v. Haeften and co-workers, "Observation of Atomiclike Electronic Excitations in Pure ^{3}He and ^{4}He Clusters Studied by Fluorescence Excitation Spectroscopy.," *Phys. Rev. Lett. 87, 1,* 2001.

[16] F. Stienkemeier and K. Lehmann, "Spectroscopy and dynamics in helium nanodroplets," *J. Phys. B: At. Mol. Opt. Phys. 39, R127–R166,* 2006.

[17] L. Gomez and co-workers, "Shapes and vorticities of superfluid helium nanodroplets," *Science 345 (6199), 906-909,* 2014.

[18] A. McKellar, Y. Xu and W. Jäger, "Spectroscopic Exploration of Atomic Scale Superfluidity in Doped Helium Nanoclusters," *Phys. Rev. Lett. 97, 1,* 2006.

[19] J. P. Toennies and A. F. Vilesov, "Superfluid Helium Droplets: A Uniquely Cold Nanomatrix for Molecules and Molecular Complexes," *Angew. Chem. Int. Ed. 43, 2622-2648,* 2004.

[20] L. Gomez and co-workers, "Size of large He Droplets," *J. Chem. Phys. 135, 154201,* 2011.

[21] M. Lewerenz, B. Schilling and J. Toennies, "A new scattering deflection method for determining and selecting the sizes of large liquid clusters of ^{4}He," *Chem. Phys. Lett. 206, 381-387,* 30 April 1993.

[22] T. Jiang and J. A. Northby, "Fragmentation Clusters Formed in Supercritical Expansion of ^{4}He," *Phys. Rev. Lett. 68, 2620,* 27 April 1992.

[23] O. Kornilov and J. P. Toennies, "The determination of the mean sizes of large He droplets by electron impact induced attenuation," *Int. J. Mass Spectrom. 280, 209-212,* 2009.

[24] H. Pauly, "Production and Diagnosis of Cluster Beams," in *Atom, Molecule, and Cluster Beams II*, Springer Science & Business Media, 2000, p. 117.

[25] P. Bartl, PhD Thesis - Rare gas cluster formation in helium nanodroplets, Innsbruck: University of Innsbruck, 2013.

[26] A. Conjusteau, "PhD Thesis - Spectroscopy in Helium Nanodroplets:," in *Studying Relaxation Mechanisms in Nature's Most Fascinating Solvent*, Princeton University, 2002, p. 15.

[27] B. H. Brandsden and C. J. Joachain, Physics of Atoms and Molecules, 2. Edition, Prentice Hall, 2003.

[28] C. Møller, "Zur Theorie des Durchgangs schneller Elektronen durch Materie," *Ann. Phys. 406, 531–585,* 1932.

[29] T. Carlson and M. Krause, "Electron Shake-Off Resulting from K-Shell Ionization in Neon Measured as a Function of Photoelectron Velocity," *Phys. Rev. 140, A1057,* 1965.

[30] T. Mayer-Kuckuk, Atomphysik, Teubner Verlag, 1997.

[31] K. Schulz and co-workers, "Observation of New Rydberg Series and Resonances in Double Excited Helium at Ultrahigh Resolution," *Phys. Rev. Lett. 77, 3086,* 1996.

[32] Y. Morishita and co-workers, "Experimental evidence of interatomic Coulombic decay from the Auger final states in argon dimers," *Phys. Rev. Lett. 96, 243402,* 2006.

[33] P. Lablanquie and co-workers, "Appearance of interatomic Coulombic decay in Ar, Kr, and Xe homonuclear dimers," *J. Chem. Phys. 127, 154323,* 2007.

[34] F. Trinter and co-workers, "Evolution of Interatomic Coulombic Decay in the Time Domain," *Phys. Rev. Lett. 111, 093401,* 30 August 2013.

[35] N. Sisourat and co-workers, "Ultralong-range energy transfer by interatomic Coulombic decay in an extreme quantum system," *Nature Physics 6, 508-511,* 2010.

[36] N. Sisourat, "private communications," 2013.

[37] N. Sisourat, "private communications," 2014-2105.

[38] J. Doye, "Lennard-Jones Clusters," The Cambridge Cluster database, 1997. [Online]. Available: http://doye.chem.ox.ac.uk/jon/structures/LJ.. [Accessed 30 01 2015].

[39] W. Nolting, "Klassische Mechanik," in *Grundkurs Theoretische Physik 1*, Berlin Heidelberg, Springer-Verlag, 2006, p. 228.

[40] J. Scott, "Aerospace.org," 17 April 2005. [Online]. Available: http://www.aerospaceweb.org/question/propulsion/q0224.shtml. [Accessed 06 02 2015].

[41] "Wikipedia," 20 December 2014. [Online]. Available: http://en.wikipedia.org/wiki/Shock_diamond. [Accessed 06 02 2015].

[42] M. Norman and K. Winkler, "Supersonic Jets," in *LOS ALAMOS SCIENCE*, Los Alamos National Lab., 1985, pp. 41-71.

[43] T. Quast, "Monochromatoren," in *PhD Thesis - Photoemission with combined laser and synchrotron pulses: Setup of a user facility and experiments*, FU Berlin, 2000, p. 86.

[44] RoentDek, "MCP Delay Line Detector Manual," in *Version 11.0.1505.1*.

[45] L. Foucar, Ionisation und Anregung von Wasserstoff- und Deuteriummolekülen mit Synchrotronstrahlung, Goethe-Universität Frankfurt, 2003.

[46] K. Kreidi, Diploma Thesis - Photodoppelionisation von H_2 – eine Analogie zum Doppelspalt, Goethe-Universität Frankfurt am Main, 2005.

[47] T. Jahnke, PhD Thesis - Interatomic Coulombic Decay - Experimentelle Untersuchung eines neuartigen, interatomaren Abregungsmechanismus, Goethe-Universität Frankfurt am Main, 2005.

[48] M. Schöffler, PhD Thesis - Grundzustandskorrelationen und dynamische Prozesse untersucht in Ion-Helium-Stößen, Goethe-Universität Frankfurt am Main, 2006.

[49] M. Schöffler, Diploma Thesis - Entwicklung und Aufbau eines Abbildungssystems zur Messung von Elektronen jenseits niedriger Energien, Goethe-Universität Frankfurt am Main, 2002.

[50] F. Kohlrausch, in *Praktische Physik: Zum Gebrauch für Unterricht und Forschung Band 2*, Stuttgart, B.G. Teubner, 1996, p. 28.

[51] D. Buchta and co-workers, "Charge transfer and Penning ionization of dopants in or on helium nanodroplets exposed to EUV radiation," *J. Phys. Chem. 117 (21), 4394–4403,* 2 May 2013.

[52] A. Braun and M. Drabbels, "Photodissociation of alkyl iodides in helium nanodroplets. I. Kinetic energy transfer," *J. Chem. Phys. 127, 114303,* 2007.

[53] A. Braun und M. Drabbels, „Imaging the Translational Dynamics of CF_3 in Liquid Helium Droplets,“ *Phys. Rev. Lett. 93, 253401,* 2004.

[54] P. Radcliffe and co-workers, "Excited-State Relaxation of Ag_8 Clusters Embedded in Helium Droplets," *Phys. Rev. Lett. 92, 173403,* 2004.

[55] K. Lehmann, "Spectroscopy and Dynamics of doped helium nanodroplets," University of Virginia.

[56] K. Lehmann and A. Dokter, "Evaporative Cooling of Helium Nanodroplets with Angular Momentum Conservation," *Phys. Rev. Lett. 92, 173401,* 2008.

Figures and Tables

Tables

Acknowledgements

At first, I want to thank Professor Reinhard Dörner, who has given me the opportunity to write this master thesis. From the first time when I knocked at the door to his office end of 2013, his door was always open for questions. He has always found time to sit down next to me and discuss the experimental results and even details of the analytical proceedings. I am thankful for his confidence in letting me perform the experiment which this master thesis is based on and for his scientific advices which guided me through my work.

Secondly, I want to thank Florian Trinter, who has spent so much time helping me to construct the COLTRIMS spectrometer and to run the experiment in January 2014. From the outset, he guided me through the beamtime preparation and took care of all the bureaucratic hurdles which accompany an experiment at a synchrotron facility. After the beamtime, he spent many hours helping me with the analysis of the experimental data. I thank him for his exceeding endurance in introducing me to all the subtleties of the experimental and analytical methods.

In this context, I would like to thank Dr. Till Jahnke whose pioneer work in particular on the field of ICD has, without doubt, paved the way for this experiment. As probably the most demanded contact person for all kinds of scientific and technical issues, he radiates exceptional serenity and an encouraging optimism in seemingly hopeless situations. He took time to answer all questions about programming the analyzing software and the physics behind ICD.

I am also grateful to Dr. Markus Schöffler whose expertise with the COLTRIMS technique was essential before and during the beamtime and whose good mood is always cheering.

My very special appreciation is extended in particular to my colleagues, namely Florian Trinter, Daniel Metz, Martin Pitzer, Markus Waitz, Elias Jabbour al Maalouf, Christian Janke, Jonas Riest and Natascha Wechselberger who have participated in the two-week beamtime and helped to set up and run the experiment. They have worked through countless day and nightshifts and have put a lot of effort in the success of the experiment.

My further thanks also go to Prof. Christian Pettenkofer from the HZB for providing me beamtime at the TGM-7 beamline.

Last but not least, I would like to express my gratitude to my family, my parents, my brother and my girlfriend who have always been an important anchor of stability in my life - My wholehearted thanks to you for having supported me.

Erklärung nach § 28 (12) Ordnung für den Bachelor- und dem Masterstudiengang

Hiermit erkläre ich, dass ich die Arbeit selbstständig und ohne Benutzung anderer als der angegebenen Quellen und Hilfsmittel verfasst habe. Alle Stellen der Arbeit, die wörtlich oder sinngemäß aus Veröffentlichungen oder aus anderen fremden Texten entnommen wurden, sind von mir als solche kenntlich gemacht worden. Ferner erkläre ich, dass die Arbeit nicht - auch nicht auszugsweise - für eine andere Prüfung verwendet wurde.

Frankfurt, den